Probing the Photodynamics of Photoprotective Molecules and Two-Photon Activated Metal Complexes

Michael David Horbury

Submitted for the Qualification of Doctor of Philosophy in Chemistry

University of Warwick, Department of Chemistry

April 2016

Table of Contents

List of Figures

List of Tables

Acknowledgements

I would like to extend my deepest thanks to my PhD supervisor Dr Vasilios Stavros, for the incredible support and assistance he has provided throughout my PhD. This is despite the fact I have, on several occasions, nearly caused him heart attacks.

I would also like to thank the rest of "Team Stavros" past and present. Firstly, I would particularly like to thank Dr Ed Greenough for teaching me everything I know about transient absorption spectroscopy and for drastically improving my vocabulary. Secondly a special thanks to: Lewis 'That Physicist' Baker for providing invaluable assistance with anything physics and code related, Jamie 'The Lucky One' Young for providing me company throughout my PhD and Dr Mick 'I said Waltz' Staniforth who listen to my crazier interpretations of my data and for sharing a similar sense of dark humour. Finally, I would like to thank, Victor Quan, Natercia 'The Organic Chemist' Rodrigues, the various Masters students, Mr Conner Gallagher and Ms Faye Monk, and the past members, Dr Garth Roberts, Dr Adam Chatterley and Dr Dave Hadden.

I also extend my gratitude to the members of the Costantini group: Jon D. Blohm for the various discussions on a range of computer games; Dr Ada Della Pia, Dr Luís Perdigão, Dan Warr, James Lawrence and Phil Blowey. Additionally, I would like to thank the electronics grandmaster, Mr Rod Wesson, for bring a many electronic item back from the dead. Alongside this I would like to thank the various collaborators: Dr Nicola Smith, Prof. Peter Sadler, Prof. Martin Paterson and Dr Tolga Karsili.

To my family and friends for the support they have provided. I am deeply indebted to my fiancée Natalie Hallgarth for the incredible support she has provided without which I would have never succeeded. Furthermore, she has had to put up with the constant late nights, when I go on and on about science, and finally for attempting to teach me the various rules of written English.

Finally, I would like to thank: Squidge 'The Spike Floof', my large collection of computer games for helping me unwind, in particular the Mass Effect and The Witcher trilogies, pastries, energy drinks, sugar, large quantities of rum, metal music, Razer PC mouses, ham, bicycle, the lamppost (I still have the scar) and last but not least pasta.

Declaration

This thesis is submitted to the University of Warwick in support of my application for the degree of Doctor of Philosophy. It has been composed by myself and has not been submitted in any previous application for any degree. The work presented (including data generated and data analysis) was carried out by the author except in the cases outlined below:

i. The time-resolved ion-yield and time-resolved velocity map imagining data shown in Section 3.3.1 was collected by M. Staniforth and J. D. Young

ii. The deuteration of 4-*tert*-butylcatechol, drying of solvents and NMR spectra in Chapter 3 were performed by W.-D. Quan

iii. The theory calculations used in Chapter 3 were performed by M. Staniforth

iv. The preparation of the buffer solutions was carried out by W.-D. Quan

v. The theory calculations used in Chapter 5 were performed by M. J. Paterson

vi. The synthesis and characterisation of complex **1** in Chapter 5 was done by N. A. Smith and P. J. Sadler

Parts of this thesis have been published or by the author:

Chapter 3:

M. D. Horbury, L. A. Baker, W.-D. Quan, J. D. Young, M. Staniforth, S. E. Greenough, and V. G. Stavros, Bridging the Gap between the Gas and Solution Phase: Solvent Specific Photochemistry in 4-tert-Butylcatechol, *J. Phys. Chem. A.*, 2015, **119**, 11989-11996

Chapter 4:

M. D. Horbury, L. A. Baker, W.-D. Quan, S. E. Greenough and V.G. Stavros, Photodynamics of Potent Antioxidants: Ferulic and Caffeic Acids, *submitted*.

Chapter 5:

S. E. Greenough, M. D. Horbury, N. A. Smith, P. J. Sadler, M. J. Paterson and V.G. Stavros, Excited-State Dynamics of a Two-Photon-Activatable Ruthenium Prodrug, *ChemPhysChem*, 2016, **17**, 221-224

Abstract

The work presented in this thesis consists of three distinct areas, each of which is explored using solution-phase femtosecond transient electronic (ultraviolet/visible) absorption spectroscopy. The first area is the effects of the environmental surroundings on the intrinsic photodynamics of a molecule. The second area is the photodynamics responsible for the apparent photostability of a pair of photoprotective molecules. Finally, we explore the effects of two-photon excitation on a ruthenium metal complex. The overarching link between these areas, which at face value appear disconnected, is the idea of the protection of biological systems from the deleterious effects of exposure to solar ultraviolet.

The first experiment studies the solvation effects on the photodynamics of 4-*tert*-butyl-1,2-dihydroxybenzene, a motif of an ultraviolet radiation absorbing chromophore subunit of eumelanin, which serves in the body's natural photoprotection mechanisms. This work demonstrates that the level of solvent interaction can have a drastic effect on the inherent photodynamics. In the case of a weakly interacting solvent the observed dynamics display a similarity to those observed of the molecule in the isolated environment of the gas-phase, which consist of an ultrafast O–H bond dissociation. However, when placed in a strongly interacting solvent, the dynamics change significantly. Rather than an ultrafast dissociation, a multitude of decay pathways occur instead and take place on the order of nanoseconds.

The second experiment studies the ultrafast deactivation route for a pair of sunscreening agents, 3-(4-hydroxy-3-methoxyphenyl)-2-propenoic acid and 3-(3,4-dihydroxyphenyl)-2-propenoic acid. In this work, we highlight an ultrafast photoisomerization pathway between the *trans*- and *cis*-isomers. This involves a population transfer between two excited states, aided by a conical intersection and subsequently through a second conical intersection between an excited state and ground state along the isomerization coordinate, to regenerate the original *trans*-isomer or the *cis*-isomer.

The third experiment studies the role of two-photon activation on a ruthenium poly-pyridyl complex and compares this to the one-photon activation process. In this work we demonstrate that both methods of activation result in the same photoproduct and on comparable timescales and yields. In doing so, we demonstrate that the observed excited state dynamics appear to be independent of the excitation method, which may have repercussions in the design of next generation photochemotherapy drugs.

Abbreviations

1-D	One-Dimensional
4-TBC	4-tert-Butylcatechol
εr	Dielectric Constant
μs	Microsecond
BBO	β-Barium Borate
bpy	Bipyridine
BS	Beam Splitter
CCD	Charge Coupled Device
CI	Conical Intersection
DAS	Decay Associated Spectrum
DFG	Difference Frequency Generation
DNA	Deoxyribonucleic Acid
ESA	Excited State Absorption
fs	Femtosecond
FWHM	Full Width Half Maximum
GM	Göppert-Mayer
GSB	Ground State Absorption
GVD	Group Velocity Dispersion
IC	Internal Conversion
IET	Intermolecular Energy Transfer
ISC	Intersystem Crossing
IVR	Intramolecular Vibrational Redistribution
KE	Kinetic Energy
KIE	Kinetic Isotope Effect
KOALA	Kinetics Observed After Light Absorption
MC	Metal-Centred
MCP	Micro-Channel Plate
MLCT	Metal-to-Ligand Charge-Transfer
MP	Multiphoton Processes

NA	Nicotinamide
ND	Neutral Density
NMR	Nuclear Magnetic Resonance
ns	Nanosecond
OD	Optical Density
OPA	One-Photon Absorption
OPG	Optical Parametric Generation
PCI	Pentacoordinate Intermediate
PDT	Photodynamic Therapy
PEC	Potential Energy Cut
PES	Potential Energy Surface
ps	Picosecond
PTFE	Polytetrafluoroethylene
PYP	Photoactive Yellow Protein
REMPI	Resonance Enhanced Multiphoton Ionization
ROS	Reactive Oxygen Species
SE	Stimulated Emission
SFG	Sum Frequency Generation
SHG	Second Harmonic Generation
TAS	Transient Absorption Spectrum
TEAS	Transient Electronic Absorption Spectroscopy
TKER	Total Kinetic Energy Release
TPA	Two-Photon Absorption
TR-IY	Time-Resolved Ion Yield
TR-VMI	Time-Resolved Velocity Map Imaging
UV	Ultraviolet
VET	Vibrational Energy Transfer
vFC	Vertical Franck-Condon

1. Introduction

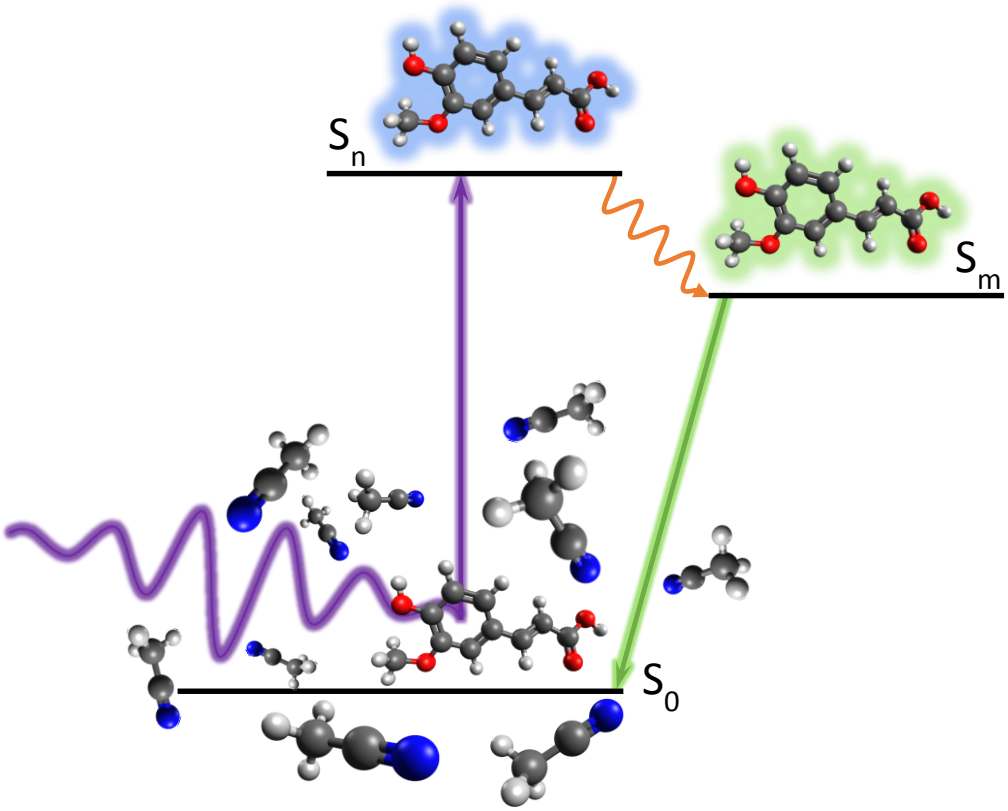

"Science is simply the word we use to describe a method of organizing our curiosity"

Tim Minchin

1.1 Spectroscopy

Spectroscopy is a powerful tool for obtaining information about a variety of systems ranging from the properties of individual atoms, to the composition of celestial bodies. The origins of spectroscopy can be traced back to Newton with the separation of the solar spectrum into its composite colours.[1] In 1802 Wollaston expanded upon Newton's work by discerning dark spectral lines within the solar spectrum.[2] However, it was not until Herschel's work in 1822 that spectroscopy was used as an apparatus for chemical analysis; by burning various compounds the resulting colour of the flame could be used to identify the constituent elements.[3] This approach used the *emission* line spectrum for identification rather than the *absorption* lines observed within the solar spectrum. In 1859 Kirchhoff put forward a theory that linked emission and absorption, stating that any atomic species that possessed a strong emission at a particular wavelength would also absorb at that same wavelength.[4] This theory gave rise to the use of visible spectrophotometry, both absorption and emission, as a powerful tool for chemical analysis and led to the identification of new elements. The reason behind why the absorptions and emissions appeared as distinct lines was not explained until the discovery of the electron in 1897 by J. J Thompson,[5] followed by the dawn of quantum mechanics. Bohr linked the idea that when an electron transitions between two states, it will either absorb or emit light equal to the energy gap between the two states, causing characteristic spectral lines.[6] Not only did this explain the discrete spectral lines, it also highlighted the information that could be gained on the inner workings of atoms and molecules through spectroscopy.

Spectroscopy was eventually applied to monitoring the progression of chemical reactions in the form of flash photolysis; a rudimentary pump-probe technique.[7,8] An initial flash of light (pump) is used to initiate a chemical reaction and the progression in the reaction is then tracked by the change in absorption (probe) of the sample over time. Limitations in the temporal and spectral resolutions limited the amount of information that could be gleaned and also limited the types of chemical reactions that could be analysed in this way. The development of the laser in the late 1960s led to a stark improvement in the information that could be acquired from spectroscopy.[9] A laser's ability to produce coherent light with narrower spectral dispersion and shorter pulse durations than previous light sources, provided a host of new spectroscopic techniques, some of which will be discussed in the ensuing paragraphs and chapters.

In 1974 the first laser with a pulse duration in the femtosecond (10^{-15} s, fs) regime was produced using the technique of mode-locking.[10] This was a particularly noteworthy

milestone as nuclear motion occurs on this timescale, providing unparalleled information on reaction dynamics. This ability was first exploited by Ahmed Zewail in studying the photodissociation of the triatomic molecule, iodine cyanide.[11,12] Zewail further applied the use of femtosecond pulses to a plethora of systems ranging from diatomics to large polyatomic systems, leading to the birth of "femtochemistry"; this earned Zewail the Nobel Prize for chemistry in 1999.[13]

In this thesis the femtosecond spectroscopic technique, transient electronic (ultraviolet (UV)/visible) absorption spectroscopy (TEAS), is used to garner insight into three areas. The first is the biologically relevant motif, 4-*tert*-butylcatechol in several differing environments, allowing for the observation of environmental influences upon the intrinsic photodynamics of this motif. Using this technique will help to build a clearer picture of the photodynamics of the full biomolecule, eumelanin, in its native environment. Secondly TEAS is used to study the photodynamical processes that occur within UV photoprotective (or sunscreen filter) molecules. Many of these molecules have been studied *via* static irradiation experiments, where they display relatively long-term stability to prolonged UV exposure while reducing the effects of UV induced photodamage to human skin. However, the underlying photophysics responsible for their photoprotective nature is poorly understood, and here we explore the dynamics of ferulic acid (3-(4-hydroxy-3-methoxyphenyl)-2-propenoic acid) and caffeic acid (3-(3,4-dihydroxyphenyl)-2-propenoic acid) as representative cases, to shed-light on their apparent photostability. Finally, we build upon previous work on the mechanism of one-photon (OPA) activation of a potential photochemotherapy drug, a ruthenium poly-pyridyl complex, $[Ru(bipyridine)_2(nicotinamide)_2]^{2+}$ ($[Ru(bpy)_2(NA)_2]^{2+}$). Specifically, we explore how two-photon absorption (TPA) alters the photoactivation mechanism of this drug versus the one-photon absorption counterpart.

1.2 Absorption

Any atom or molecule is capable of absorbing light and thereby gaining the energy of the incident photon which induces a transition to a higher energy level. Depending on the wavelength of the light, this transition can be either electronic, vibrational or rotational. The focus of this thesis is on electronic transitions which, for aromatic molecules, are usually caused by the absorption of light in the UV-visible region of the electromagnetic spectrum.

Here, an overview is given on the modelling of absorption in a classical manner, before moving onto the quantum mechanical interpretation and the various rules governing the strength of absorption.

1.2.1 Beer-Lambert Law

When light with intensity I_0 passes through a solution, it can be attenuated by the molecules absorbing the incident light. The amount of absorption (A) at a specific wavelength (λ) is given by $\log(I_0(\lambda)/I(\lambda))$, where I is the intensity of light after transmission through the sample. The absorption of a sample can be related to the path length of the absorbing medium (l) and concentration of the absorber (C) by the Beer-Lambert law:[14]

$$A(\lambda) = \log\frac{I_0(\lambda)}{I(\lambda)} = \varepsilon(\lambda)lC \tag{1.1}$$

Here, ε is the molar absorption coefficient of the sample and, since A is dimensionless, has the units mol^{-1} dm^3 cm^{-1}. In order to understand where this coefficient comes from and how it relates to a particular species, it is best to invoke a quantum mechanical interpretation.

1.2.2 Schrödinger Equation

A quantum mechanical interpretation first requires consideration of the Schrödinger equation.[15] Any molecular property can be described by solving its molecular Schrödinger equation:[15-17]

$$\mathrm{H}\psi(r,R) = \mathrm{E}\psi(r,R) \tag{1.2}$$

In Equation (1.2), H is the Hamiltonian operator, E is the total energy and ψ is the wavefunction for the molecule over both the nuclear coordinate (R) and the electron coordinate (r). The Hamiltonian is constructed from the sum of potential and kinetic energy operators:[15-17]

$$\mathrm{H} = \mathrm{T}_e + \mathrm{T}_n + \mathrm{V}_{en} + \mathrm{V}_{ee} + \mathrm{V}_{nn} \tag{1.3}$$

V_{ee} and V_{nn} are the potential energies arising from the coulombic repulsion between the electrons and between the nuclei, respectively; V_{en} is the potential energy of the coulombic attraction between the electron and the nuclei; T_e and T_n are the kinetic energies for the electrons and nuclei respectively.

1.2.3 Born-Oppenheimer Approximation

Due to the complex nature of polyatomic systems as well as modelling system in an adiabatic manner an approximation is required. The approximation that is used throughout this thesis is the Born-Oppenheimer approximation,[18,19] which exploits the mass difference between electrons and nuclei ($m_{proton}/m_{electron} \approx 1836$) to justify the separation of the nuclear motion from electronic motion. This enables the separation of

the electronic (e) and nuclear (n) terms of the Schrödinger equation. In effect, whenever the nuclei move, the electrons rearrange instantaneously, or the electrons can move while the nuclear coordinates remain fixed. The electronic Schrödinger equation, which takes into account fixed nuclear coordinates is as follows:[15-17]

$$\mathrm{H}_e\psi_e = \mathrm{E}_e\psi_e \tag{1.4}$$

As the nuclear coordinates are fixed, the Hamiltonian operator is now composed of:[15-17]

$$\mathrm{H}_e = \mathrm{T}_e + \mathrm{V}_{en} + \mathrm{V}_{ee} \tag{1.5}$$

V_{en} still depends on the nuclei coordinates and so do E_e and ψ_e, but since the nuclear coordinates are stationary it can be treated as a parametric variable.

The nuclear Schrödinger equation is given by:[15-17]

$$\mathrm{H}_n\psi_n = \mathrm{E}_n\psi_n \tag{1.6}$$

Where:[15-17]

$$\mathrm{H}_n = \mathrm{T}_n + \mathrm{V}_{nn} + \mathrm{E}_e \tag{1.7}$$

As the Born-Oppenheimer approximation separates the electronic and nuclear motion, E_e is first calculated using the electronic Schrödinger equation and thus treated as a constant in the nuclear Schrödinger equation.

By combining the values V_{nn} and E_e at each nuclear displacement, an adiabatic potential energy cut (PEC) along a specific displacement coordinate (Figure 1.1) can be produced for the molecule. The calculation of these PECs or more generally potential energy surfaces (PESs) for multiple displacement coordinates, using computational chemistry techniques, can assist in interpreting the experimental data obtained *via*

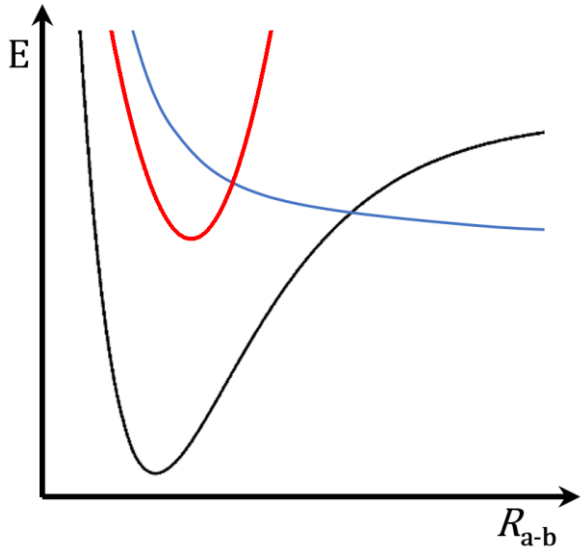

Figure 1.1 A schematic of potential energy cuts of three electronic states along the nuclear displacement coordinate **a**–**b**. Black, red and blue lines show the potential energy of the ground, bound excited and dissociative excited electronic states respectively.

spectroscopy. We will use such PECs and PESs in our discussions of the results in the proceeding chapters of this thesis.

1.2.4 Uncertainty Principle

Another consideration when using a quantum mechanical interpretation is the uncertainty principle,[15] especially with regards to the ultrafast timescales presented within this thesis. While the most prominent example of the uncertainty principle is the relationship between the position and momentum of a particle put forward by Heisenberg,[20] a similar relationship exists between energy and time:[†15]

$$\Delta E \Delta t \geq \frac{\hbar}{2} \tag{1.8}$$

Here $\hbar$ is the reduced Planck constant which equals $h/2\pi$, where h is the Planck's constant.[‡] ΔE is the uncertainty in energy and Δt is the uncertainty in time, therefore in order to generate a femtosecond pulse (small Δt) spectral resolution must be sacrificed (large ΔE) in order to satisfy the above relationship. Rather than generating an ensemble of molecules within the same vibronic state (*vide infra*), the broad energy bandwidth of the ultrafast pulse will prepare molecules with a variety of energies. This is particularly pertinent in systems that exist in a range of conformers with similar absorptions, or multiple electronic states possessing similar energies, as the spectral broadness of the pulse will cause a reduction in selectivity. Therefore, while ultrafast pulses give unparalleled insight into the kinetics of photochemistry, they do so at the sacrifice of spectral selectivity.

The amount of spectral broadening an ultrafast pulse with a Gaussian profile will experience can be calculated from:

$$\Delta\tilde{\nu} \approx \frac{0.441}{t_p c} \tag{1.9}$$

$\Delta\tilde{\nu}$ is the full width half maximum (FWHM) of the frequency in wavenumbers, t_p is the FWHM of the pulse duration and c is the speed of light in a vacuum. Therefore a Gaussian pulse with 100 fs FWHM will have at least a $\Delta\tilde{\nu}$ of ~150 cm^{-1}, while to get a spectral bandwidth of 1 cm^{-1} the pulse duration must be ~15 ps or greater.

[†] However, this is not strictly true as time does not have a time operator, but for the scope of this thesis the relationship provided is a good approximation.

[‡] $h = 6.626 \times 10^{-34}$ Js

1.2.5 Transition Dipole Moment

Returning to absorption, the absorption of a photon with energy hν induces an excitation from an initial state i to some higher state f, with the energy difference ΔE_{fi} = hν. The probability of absorption occurring has the proportionality:[17,21-23]

$$A \propto \left|\mu_{fi}\right|^2 \tag{1.10}$$

Here, μ_{fi} is the transition dipole moment of the two states; the square of the transition dipole moment is proportional to the probability of absorption. The transition dipole moment is given by:[15-17,21,22]

$$\mu_{fi} = \int \psi_f^* \hat{\mu}\, \psi_i d\tau \tag{1.11}$$

where $\hat{\mu}$ is the electric dipole moment operator, ψ_i represents the wavefunction of the state i and ψ_f^* is the complex conjugate of the wavefunction of state f. Both of these wavefunctions are dependent on the electronic and nuclear coordinates. By applying the Born-Oppenheimer approximation, these wavefunctions can be separated into the nuclear and electronic component wavefunctions, ψ_n and ψ_e respectively. In doing so, Equation (1.11) can be written as:[15-17,21,22]

$$\mu_{fi} = \int \psi_{fe}^* \hat{\mu}\, \psi_{ie} d\tau \int \psi_{fn}^* \psi_{in} dR \tag{1.12}$$

The first integral in Equation (1.12) is the expectation value of the electronic wavefunctions and its dependence on the electric dipole moment ($\hat{\mu}$). The second integral is dependent upon the nuclei and their vibrations, involved in the transition, and hence is referred to as the vibrational overlap integral. It is this integral that gives rise to the Franck-Condon principle.

1.2.6 Franck-Condon Principle

The Franck-Condon principle states that the intensity of vibronic transitions are dependent on the overlap between the vibrational modes of the initial and final electronic states.[24-26] A vibronic transition is when a change in the electronic and vibrational states occurs within the same transition. The strength of this coupling is dependent on the vibrational overlap integral and the probability of transition is given by the square of this integral which is called the Franck-Condon factor. The Franck-Condon principle can also be envisaged in terms of the PEC of both the ground and excited states. Generally, the minimum energy geometry of the excited state is different to that of the ground state. As previously mentioned, electronic transitions occur before any nuclear (geometric) movement, leading to a vertical transition,[17] as depicted in

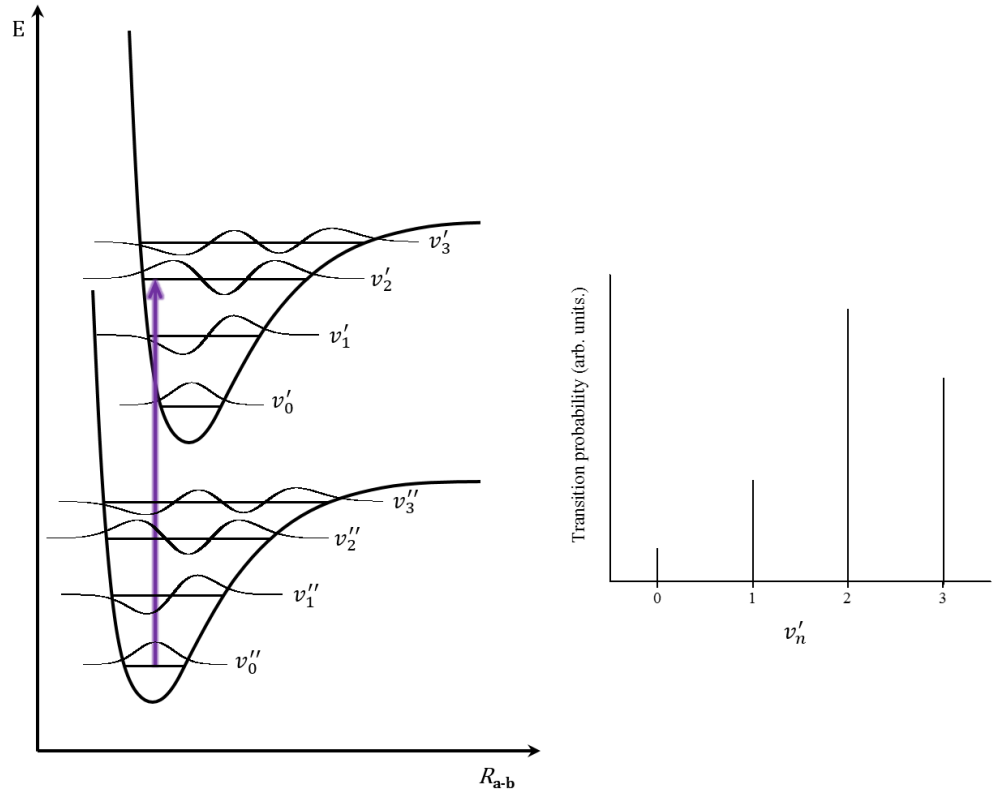

Figure 1.2 Graphical representation of the Franck-Condon principle and its effect on the transition probability. (left) Demonstrates a vertical transition, from the ground state v_0'' to an excited state with a differing minimum energy bond-length. (right) A graph showing the probability of each vibronic transition. Note that here, prime and double prime on the vibrational quantum number v refers to a vibrational state belonging to the excited and ground electronic states respectively.

Figure 1.2. In this example, a vertical transition from v_0'' has the greatest overlap with v_2', though weaker overlap exists with other v_n', therefore a spread of vibrational modes can be populated with v_2' having the highest probability (Figure 1.2 insert).

1.2.7 Selection Rules

The possibility of absorption of a photon is also governed by a series of selection rules related to the quantum numbers of the photon and electron involved in the transition. Not only does the photon's energy need to be conserved during absorption, it also possesses orbital angular momentum which also needs to be conserved, resulting in the following selection rule:[15,16]

$$\Delta l = \pm 1 \tag{1.13}$$

Where l is the orbital angular momentum of the absorbing species.

Another constraint on absorption arises due to an electron's fundamental property of spin. During an absorption, the initial spin state of the excited electron must be maintained. Therefore the spin multiplicity $(2S + 1)$[§] of the final state must equal the

[§] $S = \sum|\boldsymbol{s}|_i$ where $\boldsymbol{s}$ is the spin of the electron (defined as $\boldsymbol{s} = 1/2$) and i is the number of electrons.[15]

initial state, though this is not formally forbidden due to the phenomenon of spin-orbit coupling.[15,16,27] This phenomenon occurs when the spin magnetic moments and orbital magnetic moments couple and allows for transitions between states of differing spin multiplicity. The probability of spin-orbit coupling allowing a transition to occur is proportional to the mass of the atom ($p \propto Z^4$),[15] hence molecules containing heavy atoms have a higher propensity to undergo transitions resulting in a change of spin multiplicity. Within this thesis, we will only be concerned by states with a spin multiplicity of 1 ($S = 0$, singlet, S_n) and 3 ($S = 1$, triplet, T_n)

1.2.8 Two-Photon Absorption

Currently we have only discussed an electronic transition, i to f, due to absorption of one photon equal in energy to ΔE_{fi}. It is in fact possible that this transition can occur *via* the instantaneous absorption of multiple photons whose combined energy equals ΔE_{fi}.[28] While this can in principle occur with any number of photons, we shall only focus on TPA as this features in Chapter 5. Furthermore, we will only discuss TPA involving photons with equal energy *i.e.* $h\nu = 1/2\,\Delta E_{fi}$. Unlike OPA, which is a linear process, TPA is a second order nonlinear process;** absorbance displays a squared dependence with the incident light intensity (I^2). Another intricacy of TPA is its mediation by a virtual state[29] (w) which can be envisaged as a superposition of the states i and f. Therefore the absorption is proportional to:[28]

$$A \propto I^2 \left| \int \psi_w^* \hat{\mu}_{wi} \psi_i d\tau \int \psi_f^* \hat{\mu}_{fw} \psi_w d\tau \right|^2 \qquad (1.14)$$

Here, ψ_w is the wavefunction the virtual state, $\hat{\mu}_{wi}$ is the electric dipole moment between the states w and i, and $\hat{\mu}_{fw}$ is the electric dipole moment between the states f and w. Given that these two integrals are transition dipole moments, they can be separated out into their electronic and nuclear components *via* the Born-Oppenheimer approximation. This highlights the fact that, as in OPA, the vibronic transition strength is determined by the Franck-Condon principle.

As with OPA, TPA is governed by selection rules, though as two photons are involved, the rules are slightly modified. As both photons contain one quantum of angular momentum, the selection rule for l changes to:

$$\Delta l = 0, \pm 2 \qquad (1.15)$$

** Non-linear processes are explained in more detail in the experimental section (Section 2.2).

As can be seen, the difference in the selection rule of l means that states that are accessible by OPA are not accessible with TPA and *vice versa*. In the case of spin multiplicity, TPA obeys the same restrictions as with OPA.

While the above describes TPA on a quantum mechanical level, it is more practical to determine the attenuation of light passing through a sample in a classical way, akin to the Beer-Lambert law for OPA. The change in intensity as the light travels through a sample can be modelled by:[30,31]

$$I(l,\lambda) = \frac{I_0(\lambda)}{1 + \beta(\lambda) I_0(\lambda) l} \tag{1.16}$$

$\beta(\lambda)$ is the molecular TPA cross-section, given the units Göppert-Mayer (1 GM = 10^{-50} cm^4 s photons^{-1} molecule^{-1}). The value of this unit clearly demonstrates the large intensities of light required to induce a measureable number of TPA events. Generally, TPA only becomes possible with pulsed lasers as these provide sufficiently high power density.

1.3 Relaxation of Excited States

Following absorption, the excited molecule now possesses excess energy equal to hν or, in the case of TPA, 2hν. As the molecule is in an excited state, it will now want to release this excess energy and return to its ground electronic state in order to re-establish an equilibrium with its surroundings. It is able to achieve this through a variety of methods. Some of these relaxation processes can be destructive to the molecule as the excess energy could allow a chemical reaction to occur that was previously inaccessible, or even cause bond fission within the molecule. Alternatively, the molecule may relax through non-destructive pathways, returning back to its original state. Examples of these latter, non-damaging, relaxation pathways are shown in the Jablonski diagram[32] in Figure 1.3. These relaxation mechanisms generally occur on femtosecond (fs, 10^{-15} s), picosecond (ps, 10^{-12}) or nanosecond (ns, 10^{-9} s) timescales, however in the case of phosphorescence it ranges from microseconds (μs, 10^{-6} s) to hours.[27]

1.3.1 Vibrational Energy Transfer

As most of these electronic transitions are vibronic in nature, not only will the molecule possess excess electronic energy, it will also possess excess vibrational energy due to the population of higher vibrational modes v'_n ($n > 0$). From these modes the molecules will want to relax back down to the state's lowest energy vibrational mode (v'_0); it can achieve this relaxation in two ways. The first is to redistribute this energy throughout

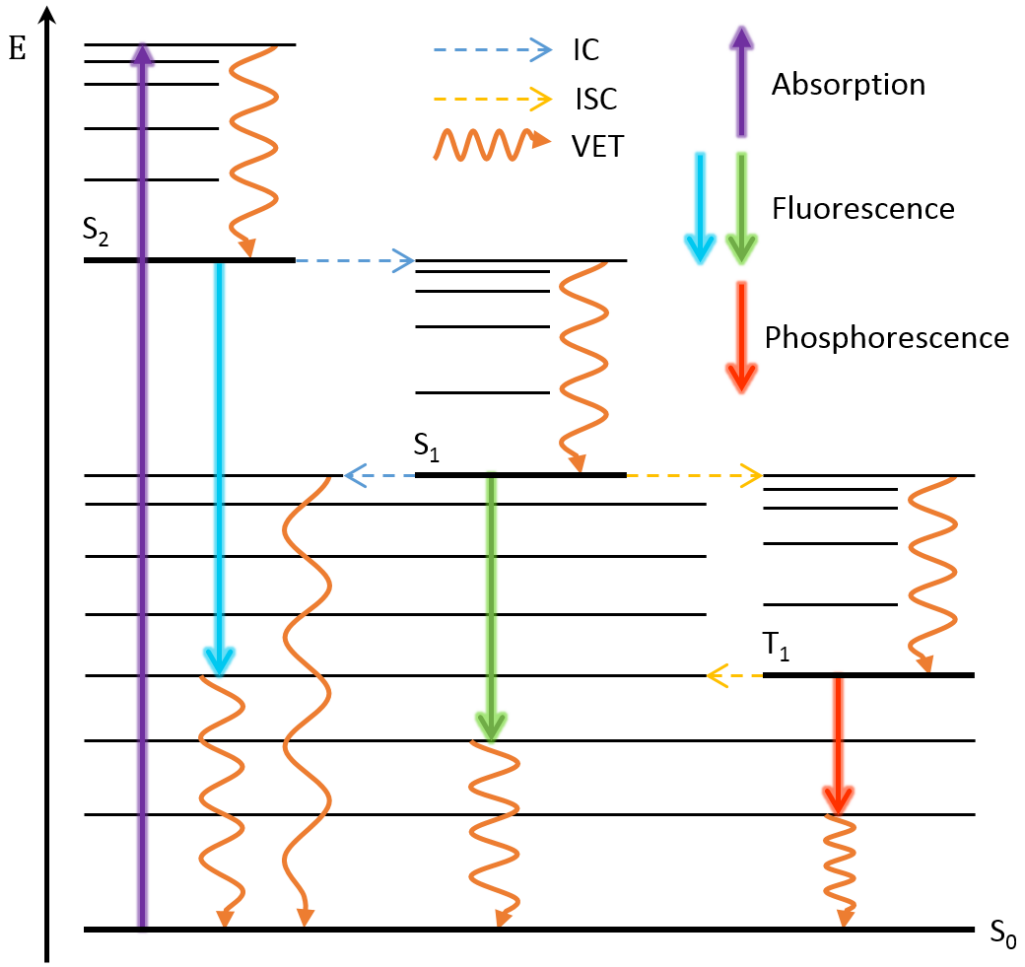

Figure 1.3 Jablonski diagram depicting possible relaxation routes of a molecule electronically excited to its S_2 state from the ground state S_0. The thick black lines represent the lowest vibrational mode (v_0) of the electronic state, while the thin black lines resent higher vibrational modes (v_n, $n > 0$).

the rest of the molecule's vibrational modes along differing nuclear coordinates. This is referred to as *intra*molecular vibrational redistribution (see below, IVR).[33,34] The other process is to transfer the excess energy to the molecule's surroundings, *e.g.* the solvent bath, and this is termed *inter*molecular energy transfer (IET).[35] As IVR requires access to additional vibrational modes, it only occurs within polyatomic molecules, while IET only occurs if the molecule is capable of interacting with other molecules. Collectively, IVR and IET are termed vibrational energy transfer (VET) and can lead to interesting changes to the relaxation dynamics of the molecule; if the initial vibrational mode possesses enough energy to access a decay pathway, but lower energy modes do not, the pathway will display a dependence on the rate of VET. VET can also occur in ground electronic state molecules that have been populated vibrationally hot from an electronic excited state (Figure 1.3).

1.3.1.1. Intramolecular Vibrational Redistribution

As previously mentioned, IVR involves excess vibrational energy transferring across other vibrational modes of the molecule. These modes are either equal or lower in energy than the initial vibrational modes. As this is a *redistribution* of the energy, the total energy of the molecule is not reduced, but rather distributed across a series of orthogonal modes. It is possible to model the rate of vibrational relaxation (k_{jb}) due to intramolecular redistribution by Fermi's golden rule:[15,16]

$$k_{jb} = \frac{2\pi}{\hbar}\left|V_{jb}\right|^2 \rho_m \tag{1.17}$$

Here $\left|V_{jb}\right|$ is related to the strength of coupling between the vibrational state, j, and the bath of additional vibrational states, b, and ρ_m is the density of states that are energetically accessible. The density of states within a molecule is dependent upon the vibrational degrees of freedom of the molecule, which is given by $3N$-6[††] where N is the number of atoms,[15-17,36] thus larger molecules tend to display faster IVR.[37] Due to the greater number of vibrational modes for the energy to spread over, the probability of coupling back to the initial state once the energy transfers out is near-zero, therefore this transfer can be treated as irreversible. In smaller molecules on the other hand, the smaller number of states to which the energy can transfer can lead to the possibility of a recurrence in the initial state.[33] This dependency on the density of states also means that the rate of transfer is dependent on the energy the vibrational mode possesses. At higher vibrational levels, more vibrational modes are energetically accessible, leading to higher rates of IVR early on. As the energy spreads across lower energy vibrational modes, the density of states becomes lower, thus reducing the rate of transfer[35] which can affect the rate of processes that are reliant on the low-energy vibrational modes *e.g.* fluorescence.

1.3.1.2. Intermolecular Energy Transfer

A molecule is also capable of disposing its excess vibrational energy *via* interaction with other molecules, however this process is non-existent in isolated systems, such as the gas-phase[‡‡] (see Chapter 3). By transferring the energy to another molecule, the excited molecule's energy is reduced, "cooling" the excited molecule. Like IVR, the rate of IET is dependent on Fermi's golden rule, but is better described by using a Landau-Teller approach; a semi-classical molecular collision theory. Therefore the rate of vibrational cooling (k_c) of the molecules excess vibrational energy is better modelled by:[35]

[††] In a diatomic, and linear polyatomic molecule, it is given by $3N$-5.
[‡‡] Unless molecular clusters are present.

$$k_c = \frac{2\tanh(\beta\hbar v/2)}{\mu\beta\hbar v}\zeta(v) \quad (1.18)$$

In the above equation v is the frequency of the vibration, μ is the reduced mass of the molecule, $\beta = 1/k_bT$, where k_b is the Boltzmann constant and T is temperature. This only works within the limits of $\hbar v < k_bT$. ζ is the friction to the vibration due to the solvent forces acting on the vibrational mode and this is inversely proportional to the frequency of the vibrational mode. As a consequence, when the molecule is in low frequency modes, the rate of IET increases. This is in contrast to IVR which slows down when modes with low vibrational quantum numbers are populated owing to the decrease in the density of states.[35]

1.3.2 Excited State Relaxation

While VET covers the excess vibrational energy caused by a vibronic transition, it does not deal with the excess electronic energy imparted to the molecule.[33,35,37] There is an array of electronic relaxation methods that an excited electronic state can undergo and these shall be discussed below.

1.3.2.1. Emission

It is possible that an electronically excited molecule can undergo the spontaneous emission of a photon by transitioning from the excited state to the ground state.[15,16,38,39] This transition can be treated as the reverse of absorption, as it is still dependent on the Franck-Condon principle and selection rules.[15,16,22] However, a few caveats must be considered. Generally, the energy of the photon due to spontaneous emission is lower than the initial absorbed photon energy, as spontaneous emission tends to occur from the lowest excited singlet vibronic state. This is referred to as Kasha's rule[40] and is a by-product of the difference in rates between VET, internal conversion (IC) (*vide infra*) and spontaneous emission. Spontaneous emission tends to occur on a ns timescale whereas VET and IC between excited states occur in the ps regime or faster.[27] As the transition is vibronic, it is also ruled by the Franck-Condon principle, and the overlap between v_0' and v_n'' is generally greater with the higher vibrational modes of the ground state. As mentioned above, this manifests as a reduction in the energy of the emitted photon compared to the absorbed photon. This phenomenon is best demonstrated by comparing the emission spectrum to the absorption spectrum: generally, the two spectra appear as near mirror images with the emission spectrum being lower in energy as shown in Figure 1.4. There tends to be some spectral overlap between the two spectra (absorption/emission) due to the v_0'' to v_0' transition, though in some cases the two spectra do not overlap. This can occur if the molecule undergoes some sort of structural

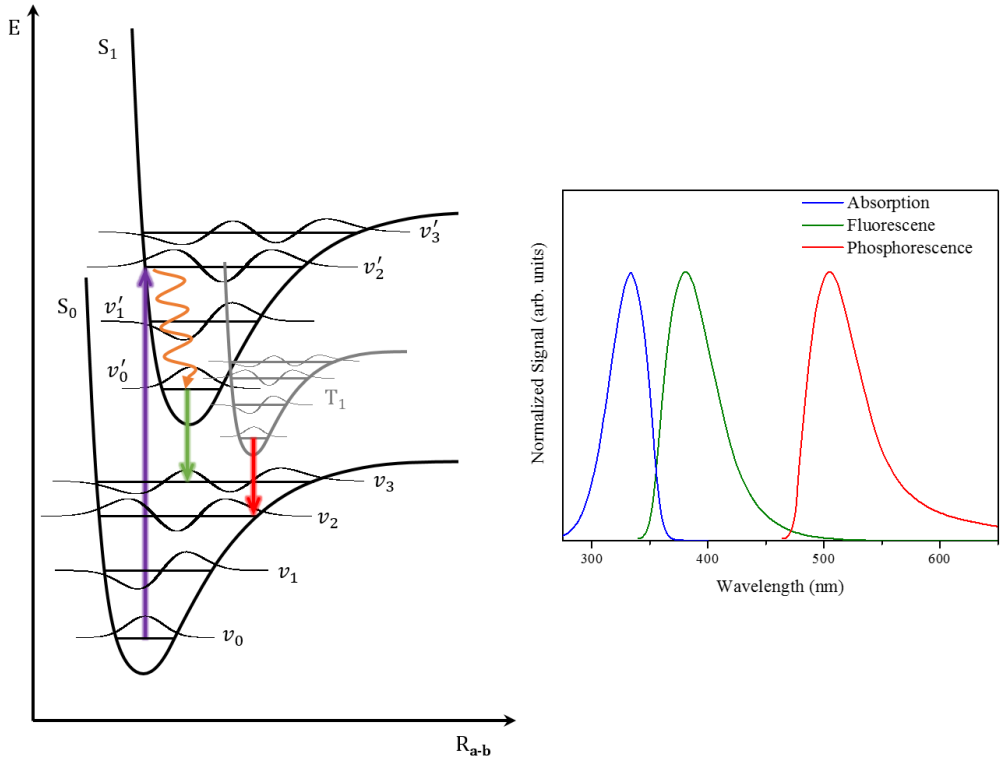

Figure 1.4 A graphical representation (left) of the effect of VET and the Franck-Condon principle on the wavelength of the emitted photon during fluorescence/phosphorescence. The graph (right) shows an example of absorption and emission spectra, the absorption (blue) and the fluorescence (green) are almost mirror images that overlap at the v_0' to v_0'' transition, while the phosphorescence is further red-shifted due to the triplet state (PEC shown in grey) being lower in energy.

change, *e.g.* excited state hydrogen transfer, as the new structural rearrangement can be more stable in its excited state reducing the energy gap between the excited state and ground state.[38]

As with emission, the S multiplicity of the initial and final states have to be maintained, though spin-orbit coupling is again able to lift this restriction.[15,16,27] When the emission causes a transition between two states with the same multiplicity, normally singlet to singlet, it is termed fluorescence. If the states change in multiplicity, commonly triplet to singlet, it is referred to as phosphorescence. In the case of phosphorescence, the emission spectrum (Figure 1.4 inset) tends to be heavily shifted to lower energies as the lowest triplet state tends to be significantly lower in energy than the lowest excited singlet. As phosphorescence is a forbidden process, the timescale for this emission can range from μs to hours.[27]

1.3.2.2. Internal Conversion

While fluorescence and phosphorescence are radiative processes (*i.e.* they involve the emission of a photon), it is possible for an excited molecule to undergo a transition

between electronic states in a non-radiative manner.[41-44] As with absorption and emission, any change in S is forbidden, though spin-orbit coupling, once again, lifts this restriction for transitioning between states of different spin. Transitions between states of the same S are referred to as undergoing IC, while transitions between states of differing S undergo intersystem crossing (ISC).

IC between electronic states is mediated by the coupling of the vibrational modes from both states. As would be expected, the probability of the transition is dependent upon Fermi's golden rule,[27] though, like IET, it is not the main determinant in the solution phase.[§§] Instead the energy gap (ΔE_{fi}) between the states i and f is the main factor in the rate of IC (k_{IC}). This dependence is given by:[44]

$$k_{IC} \propto 10^{-13} e^{(\alpha \Delta E_{fi})} \tag{1.19}$$

where α is the proportionality constant. Since the rate is exponentially dependent upon ΔE_{fi}, IC between higher lying excited states tends to occur rapidly as the energy gap between these states is smaller, due to anharmonicity. In the case of IC between states very close in energy, the IC can occur on the timescale of hundreds of femtoseconds. However IC between the lowest excited state and the ground state generally occurs on timescales of nanoseconds or longer due to the increased energy gap.[44] In cases where ΔE_{fi} tends towards zero along a particular set of nuclear coordinates, one of two situations can arise and is dependent on the nature of the states involved, leading to either an avoided crossing or a conical intersection (see below).[45-49]

1.3.2.3. Intersystem Crossing

As mentioned earlier, ISC involves a non-radiative transition between states of different spin multiplicity *e.g.* singlet to triplet. As this is a forbidden process, ISC tends to generally occur on a slower timescale (μs to hours) to IC, though in molecules containing heavy atoms ISC can be competitive with other relaxation pathways.[15] Much like IC, the rate of ISC is dependent on the energy gap between the two states. In most cases, ISC is irreversible as triplet states are always lower in energy than their corresponding singlet states.

1.3.2.4. Avoided Crossings and Conical Intersections

In order for two states to become degenerate, they must do so within a $3N$-8 subspace of the $3N$-6 nuclear coordinates space (*vide supra*),[45-49] as it is impossible for two states

[§§] However, in the gas-phase Fermi's golden rule becomes important again as the total vibrational energy cannot be reduced.

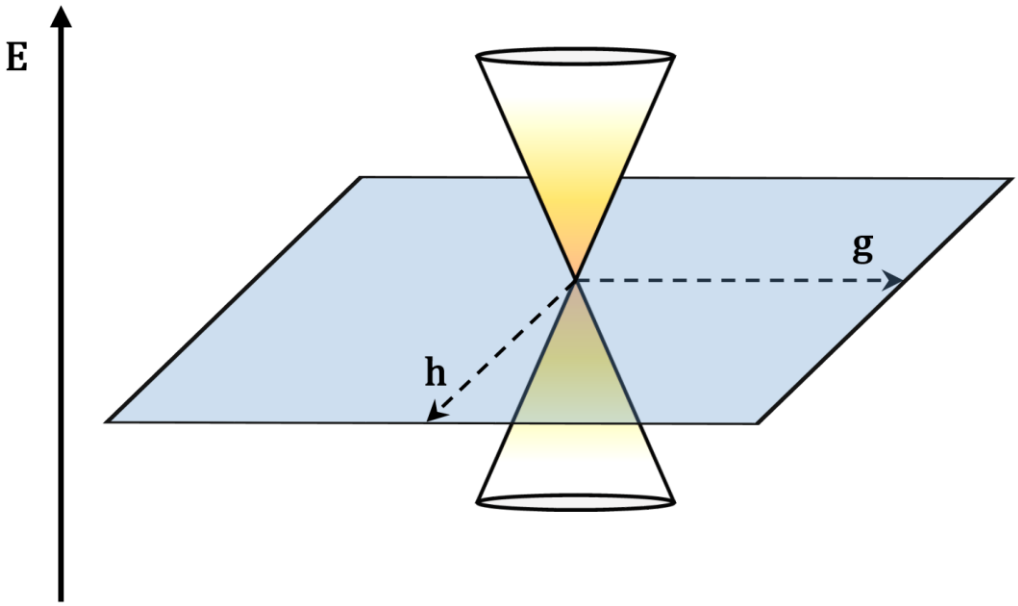

Figure 1.5 Representation of a conical intersection between two degenerate states in the two dimensional subspace **h** (derivative coupling) and **g** (gradient difference).

of the same spin multiplicity and symmetry to cross along a one-dimensional coordinate. This is due to the non-crossing rule. If a 3*N*-8 dimensional subspace cannot be formed an avoided crossing is formed instead of a point of degeneracy. However, if a 3*N*-8 subspace can be formed, a point of degeneracy will occur; these points are referred to as a conical intersection (CI). For simplicity it is easier to consider a CI in a two dimensional subspace (Figure 1.5), though they are capable of existing in multiple-dimensions. In this subspace, the CI can be envisaged as a pair of cones that are coupled at their tips, thus the term conical. The subspace consists of two coordinates referred to as the derivative coupling (**h**) and the gradient difference (**g**). **h** represents the strength of the non-adiabatic coupling between the two states, while **g** represents the steepness of the two cones (or multidimensional seam) leading to the point of degeneracy. Furthermore, at these tips, the Born-Oppenheimer approximation breaks down as the nuclear and electronic motions become strongly coupled. Due to this, the resultant dynamics at a CI are referred to as non-adiabatic.[45-49] These non-adiabatic dynamics occur rapidly, leading to an increased efficiency in transition between the two electronic states. This often makes them the dominant driving force in a molecule's photodynamics.

An example of a CI playing an important role in the photodynamics of a molecule is photoisomerization. It is possible that along an isomerization pathway, a CI is formed between the excited state and the ground electronic state. While it is possible that the initial ground state molecule is reformed, some of the excited state population can end up forming the other isomer of the molecule. Rhodopsin is a classic example of excited state relaxation *via* (*cis*/*trans*) photoisomerization and is the initial step in vision.[50]

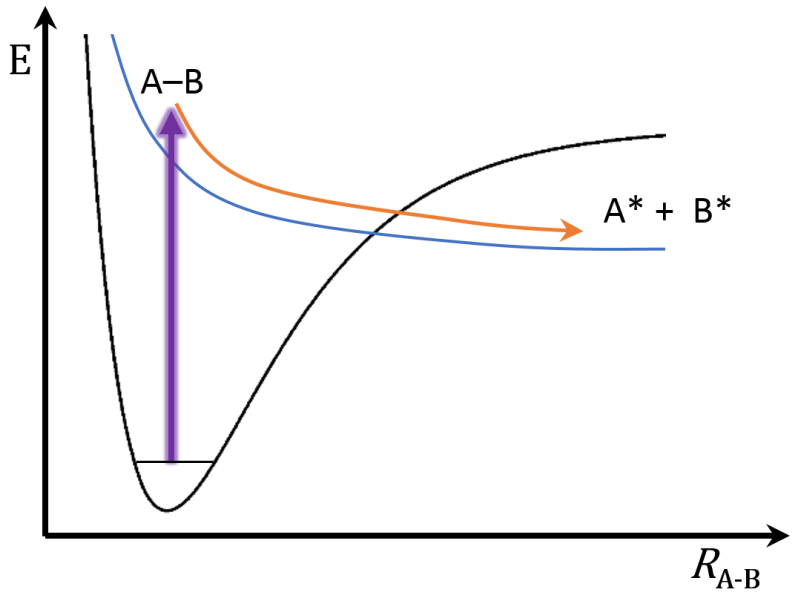

Figure 1.6 The molecule A–B undergoing photoexcitation to a dissociative excited state, leading to fragmentation of the molecule producing the fragments A* and B*.

1.3.2.5. Dissociation

Through the aforementioned processes, it is possible for a molecule to end up within a state that possesses anti-bonding characteristics with respect to a specific bond coordinate. If the excited state population ends up on this repulsive surface, the molecule can undergo bond-fission, leading to fragmentation of the molecule. An example schematic is shown in Figure 1.6 demonstrating a molecule (A-B) undergoing an excitation to a dissociative state leading to the formation of two fragments A* and B* where the excess energy is distributed between the two fragments (denoted by *). The excess electronic energy the molecule has gained due to absorption is split between the fragments as internal energy and kinetic energy. Mapping of these fragments and their kinetic energy can be of great use in gleaning insights into the inner workings of a molecule's photodynamics.[51-53] In the isolated gas-phase, once fragmentation occurs, the chance of recombination is zero, yet in solution the fragments have the possibility of interacting with the solvent environment or even recombining (*e.g.* geminate recombination).[54] How these fragments recombine, or interact with the solvent is dependent upon several factors. Monitoring the fate of these fragments can give an insight into any photoproducts that could be either harmful or beneficial to the role of the molecules.

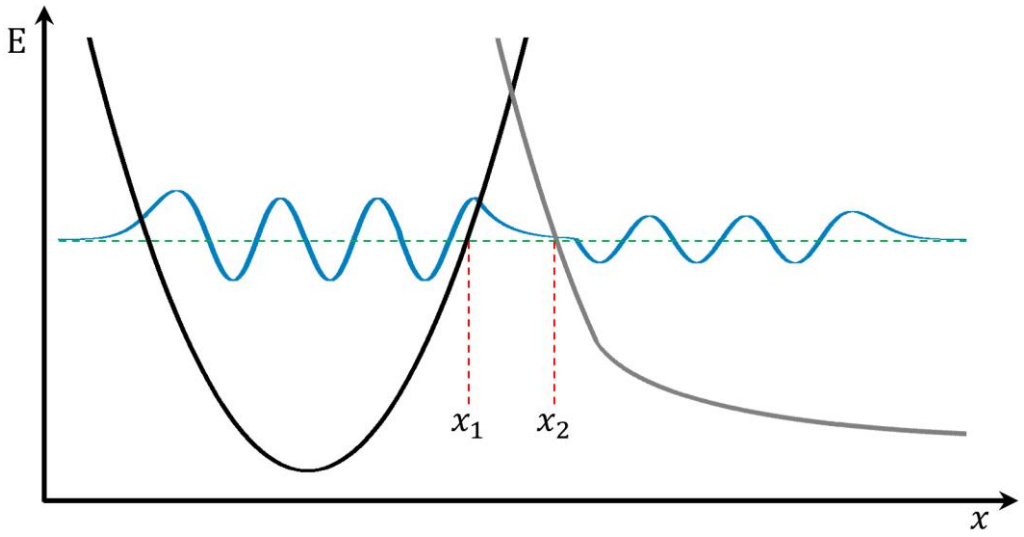

Figure 1.7 Demonstrates the non-zero nature of wavefunctions under a barrier along the nuclear coordinate x.

1.3.2.6. Tunnelling

In some cases, an excited state might encounter an energy barrier to a potential decay pathway. Under the classical view of a ball rolling on a surface, if it encounters a barrier that cannot be surmounted due to lack of energy, that particular pathway cannot occur. However, this classical view fails to take into account quantum mechanical tunnelling. Quantum mechanical tunnelling is a phenomenon that allows for a system to pass through a barrier without possessing the required energy to surmount it.[15] This occurs due to the probability of finding the molecule on the other side of the barrier being non-zero, though this probability drops off exponentially through the barrier. Figure 1.7 shows an example barrier along a nuclear coordinate (x). The rate of tunnelling through this barrier (k_t), can be given by the semiclassical Wentzel-Kramers-Brillouin approximation:[55]

$$k_t = v \cdot exp\left[\int_{x_1}^{x_2} \frac{-2}{\hbar}\sqrt{2m(V(x)-E)}dx\right] \qquad (1.20)$$

Here, $V(x)$ is the height of the barrier along the x coordinate, E is the energy of the wave, v the vibrational period of the mode mediating the tunnelling and m is the mass of the species undergoing tunnelling. This approximation only works within a one-dimensional coordinate, so is of limited use within a multi-dimensional system where other coordinates are accessible.

Since k_t is exponentially dependent upon both the mass of the tunnelling species and the size of the barrier, k_t only tends to be applicable to very light particles, like a

proton or electron, with a small barrier. This dependence on mass in tunnelling can prove to be a useful tool in determining whether a process is mediated by tunnelling as changing the isotope of an atom will have a noticeable effect on its tunnelling probability. However, this is only feasible with hydrogen and its isotope deuterium due to their diminutive mass. Considering the rate of dissociation of an O–H bond, by comparing the rate of the protonated species (k_H) to the rate of the deuterated species (k_D), a kinetic isotope effect (KIE) can be defined by:[55]

$$\text{KIE} = \frac{k_D}{k_H} \tag{1.21}$$

From this KIE it is possible to determine if the process is mediated by tunnelling, in which case the KIE value will be large (typically >10).[55] Any smaller value than this can be caused by isotopic effects on the vibrational period of the coupling mode or changes to the zero-point energy.

1.4 Pump-Probe Spectroscopy

Pump-probe spectroscopy (Figure 1.8) has previously been mentioned within this chapter, albeit briefly. Here we shall expand upon the pump-probe techniques used in more detail. The fundamental principles of pump-probe spectroscopy are to use a flash of light as a pump to initiate a dynamical process which is then monitored using a second light source as a probe, *e.g.* UV-visible absorption.[7,8,13] The femtosecond spectroscopic techniques encompassed here are: transient (UV/visible) electronic absorption spectroscopy (TEAS), time-resolved velocity map imaging (TR-VMI), and time-resolved ion yield (TR-IY). These all employ the same pump method, using a femtosecond laser

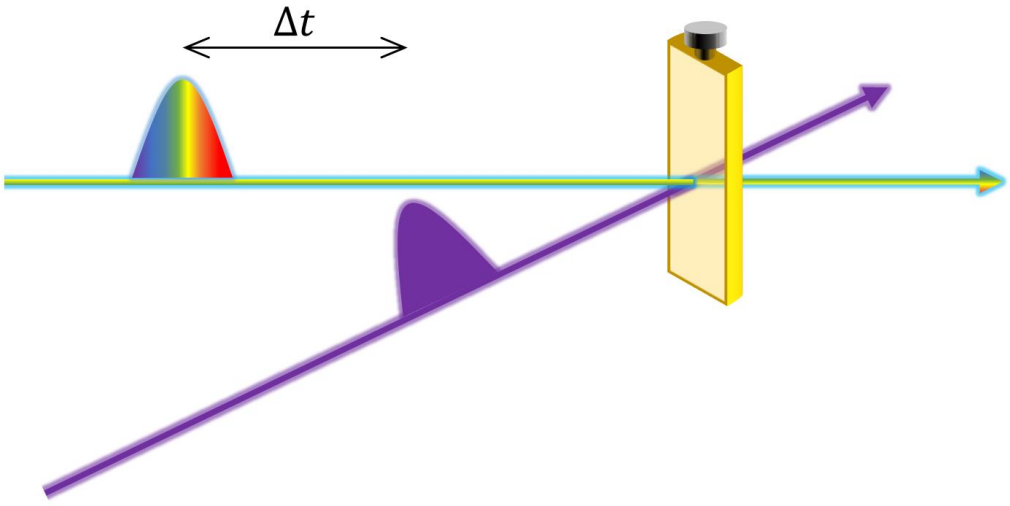

Figure 1.8 A basic example of pump-probe spectroscopy, where a photoexcitation is induced by a pump pulse (purple arrow), and then the evolving dynamics probed using a probe pulse (rainbow arrow) after a variable time-delay.

pulse to induce electronic excitation within the system of interest, though the probe technique differs significantly. While TEAS is the main focus of this thesis, TR-VMI and TR-IY are used as comparative gas-phase measurements in Chapter 3, and are therefore discussed briefly below.

1.4.1 Transient Absorption

Femtosecond transient absorption has been used to monitor the evolution of a wide variety of systems after photoexcitation. These include molecules of biological importance,[56-58] transition metal complexes,[59-61] photovoltaics[62,63] and a miscellany of organic molecules.[64-67] In order to gain time resolution, first an ultrafast pump pulse is used to prepare the sample into its excited state. Then after a time-delay (Δt) an ultrafast probe pulse interacts with the sample, *via* absorption, taking a snap shot of the system; the intensity is then recorded at varying Δt. This information allows for the progression of the photodynamics to be observed and depending on the wavelengths that comprise the probe pulse, determine the states that are probed. In this thesis, a probe pulse spanning the near UV to the red end of the visible (330 – 675 nm) is used. This probe region allows for monitoring of the evolution of electronic states due to the probe pulse inducing electronic transitions in the photoexcited molecule; in effect a time-resolved UV/visible spectrum of the excited state molecule is taken. Generally, the change in intensity in the probe pulse at different Δt is minor, therefore, for ease of interpretation a difference spectrum is produced. Therefore a probe pulse is used that passes through

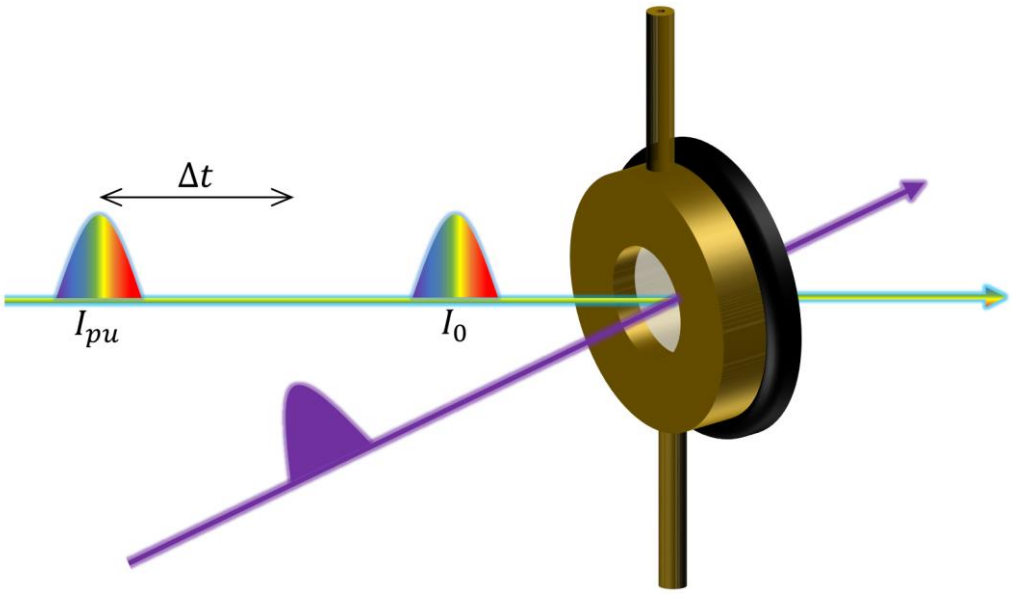

Figure 1.9 Schematic showing the pulse ordering used to generate the differential spectrum used to unravel the photodynamics of the system of interest. First a probe (rainbow arrow) pulse passes through the sample before excitation (I_0), the sample is then excited by a pump pulse (purple arrow) and after a variable Δt a second probe pulse passes through the sample (I_{pu}).

the sample before it is excited by the pump pulse (I_0), this is then compared with a probe pulse that has traverses through the sample after excitation (I_{pu}), as shown in Figure 1.9. The difference for a particular time and wavelength is given as:[68]

$$\Delta\mathrm{OD}(\lambda, t) = \log\left[\frac{I_0(\lambda)}{I_{pu}(\lambda, t)}\right] \tag{1.22}$$

Here, ΔOD is the change in optical density and λ is the wavelength. A positive ΔOD is caused by a reduction in I_{pu}, while a negative ΔOD is caused by an increase in I_{pu}. Throughout this thesis, the generated differential spectrum is referred to as the transient absorption spectrum (TAS). Figure 1.10 is an example TAS demonstrating how the overall spectrum is produced from the possible component elements. The four components within this example TAS are: the ground state bleach (GSB), stimulated emission (SE), excited state absorption (ESA) and photoproduct absorption.[69] It is through these four elements that dynamical insight can be gained and thus these shall be expanded upon below.

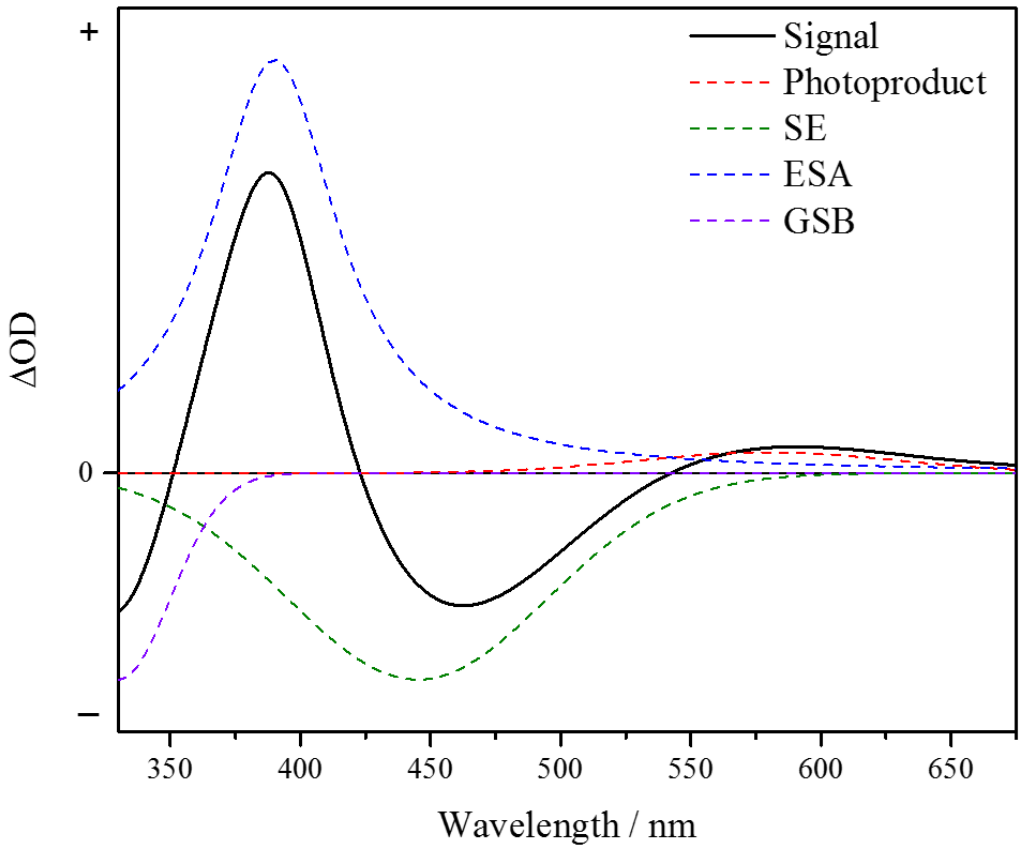

Figure 1.10 A representative TAS, showing how the overall signal is generated from a combination of possible features.

1.4.1.1. Ground State Bleach

The GSB is a by-product of the pump pulse photoexciting a number of the molecules which depletes the ground state population. Therefore, I_{pu}, will experience a diminished absorption from the ground state compared to, I_0, and thus, the GSB appears as a negative ΔOD. This only occurs if the ground state of the molecule absorbs within the spectral window of the probe. A GSB can provide useful information about the recovery, or lack thereof, of the starting species. Full recovery of the GSB is indicative of the molecules' relaxation pathway(s) occurring in a non-destructive manner. On the other hand, the incomplete recovery of the GSB either shows that the molecule has become trapped in a state that persists longer than the maximum achievable Δt of the experiment, or that the system has undergone fragmentation leading to destruction of the original molecule. The GSB can be used to generate a quantum yield for the fraction of molecules that do not return to the initial state.

1.4.1.2. Excited State Absorption

Since the excited states of a molecule are capable of further absorptive transitions to higher excited states within the molecule, these absorptions can be used to garner information about the excited state. If these absorptions are within the probe window, they will appear as positive ΔOD features in the TAS, and by tracking the changes in intensity, wavelength and broadness of these features, a host of information on the excited state dynamics can be recovered. This information can give an insight into the rate of VET, IC, ISC and numerous other phenomena.

1.4.1.3. Stimulated Emission

SE is an extension of spontaneous emission *e.g.* fluorescence, as it is also a radiative transition between an excited electronic state and the ground state.[15] However, unlike spontaneous emission that can occur at any time, SE only occurs when another photon, of equal energy to the transition, interacts with the excited molecule and induces the emission; this emitted photon can provide lifetime and energy information of the excited state. As SE causes an increase in photons within the probe pulse, it will appear as a negative ΔOD within the TAS. Generally, the region of the TAS where SE appears corresponds to the fluorescence spectrum of the molecule, though SE can appear in molecules that do not appear to fluoresce. Since the SE is induced by the probe, which is in the region of electronic transitions, the emission must occur from an electronically excited state.

1.4.1.4. Photoproducts

If the molecule undergoes fragmentation, structural rearrangement or even a chemical reaction, the end products of these processes tend to have a different absorption to the starting molecule. Therefore, they appear as additional positive peaks within the TAS that persist beyond the maximum Δt of the experiment. As these photoproducts cause a reduction in the number of original molecules, the appearance of a photoproduct is also linked to a GSB feature.

1.4.2 Time-Resolved Velocity Mapped Imaging and Ion Yield

Both TR-VMI and TR-IY are gas-phase spectroscopic techniques and work by detecting charged particles.[52,70,71] The probe in both of these techniques is a second UV-pulse that is used to ionize either the parent molecule in TR-IY, or any dissociated species in TR-VMI.[45,62,63] These ions are detected through collisional impact onto a micro-channel plate (MCP) array and phosphor screen, following their acceleration *via* ion optics. The resultant emission of light by the phosphor screen is then detected by a charge coupled device camera. The intensity of light detected at each Δt, as well as the location point of the emission of light from the phosphor screen, can be used to infer the photodynamics of the isolated molecule.

First we shall consider the information that can be provided by TR-IY. As the wavelength of the probe is fixed, it can only probe molecules that possess enough internal energy to be ionized with this wavelength (ignoring any two-photon effects). Therefore, as the molecule relaxes and redistributes the energy, *i.e.* redistribution as internal energy or fragmentation of the molecule, a smaller amount of parent ions are produced and detected. This allows an insight into the lifetime of the excited parent molecule. One consideration to be taken into account in TR-IY is that if the probe has enough energy to induce ionization within any eliminated fragments or contaminants of the sample, they will also be detected. Therefore, in order to monitor the parent molecule of interest, a time of flight mass spectrometer is used to allow for ion selectivity alongside other experimental techniques such as gating the MCP array and deflecting ions of higher/lower mass.

TR-VMI is a technique that allows for probing of species such as hydrogen atoms,[72] methyl fragments,[73] and photoelectrons. In order to probe these species with TR-VMI, they are first ionized, which can be achieved *via* single- or multi-photon ionization. In the case of hydrogen atoms, the ionization is attained by [2+1] resonance enhanced multiphoton ionization[74,75] using a wavelength of 243 nm. This induces a two-photon absorption in the hydrogen atom, caused by virtue of an excitation from the 1s to the 2s

orbital, while a third photon causes ionization from the 2s orbital. The ionised species (H^+) are then mapped onto a detector using ion optics. This mapping allows for information to be collected on the kinetic energy, the anisotropy and relative yield of the eliminated species. Using this information it is possible to determine the conditions the molecule was in as it underwent dissociation or, in the case of photoelectrons and hydrogen atoms, the excited electronic state they originated from.[76]

1.5 Environmental Effects on Photodynamics

The use of a "bottom-up" approach has been an extremely beneficial method in attempting to unravel the photodynamics of large complex systems of interest[52,70] *e.g.* eumelanin (demonstrated by Figure 1.11).[77-80] Generally these larger systems produce complex and convoluted spectra hindering the interpretation of the photodynamics. Therefore, by extracting the UV chromophore subunits, the section of the molecule where the initial excitation is localized, leads to a reduction in the level of complexity in the spectra. This allows for clearer interpretation of the dynamics. As many of the observed dynamics in biological systems tend to occur on ultrafast timescales, as is needed to out-compete dissociative pathways, it may be expected that critical dynamics of many systems would occur within the UV-chromophore. This furthers the usefulness of studying an isolated system as a model for the complete system. Once the dynamics of the simplified system are understood, the complexity of the chromophore can be increased and the dynamics built upon with the aim to reach a fuller understanding of the larger system.

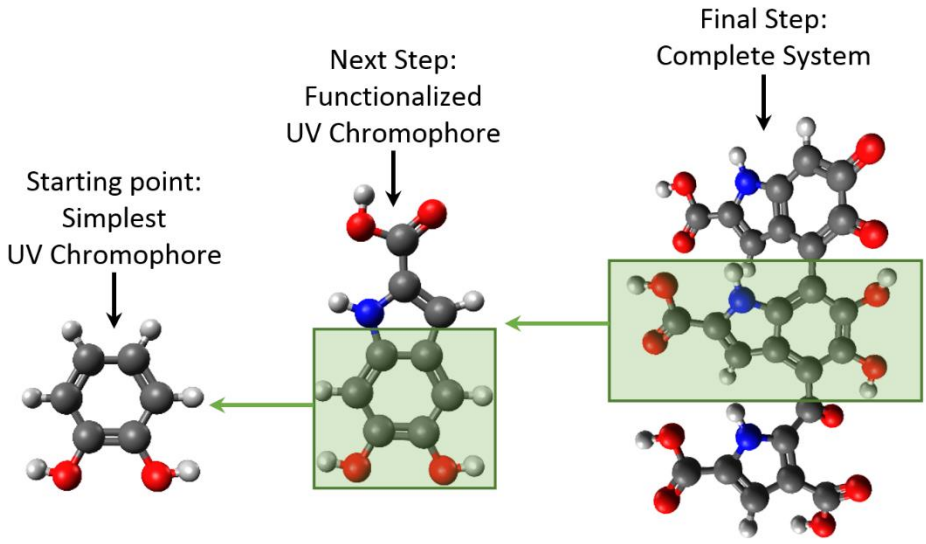

Figure 1.11 A graphic demonstrating the bottom-up approached: simplest UV chromophore = catechol, functionalized UV chromophore = dihydroxyindole carboxylic acid and complete system = eumelanin only three monomers of the large heterogeneous polymer that makes up eumelanin are shown here.

Another additional complexity within these systems is their interaction with their local environment, therefore much work has been performed under vacuum conditions to isolate the molecule, in order to isolate these interactions.[52,53,65,70,81-86] While this gives an insight into the intrinsic properties of the molecule, it is further distancing the model from the complete system. In recent years there has been a move towards understanding the environmental effects upon molecules studied in the gas-phase.[65,66,87,88] A good example of this is phenol (hydroxybenzene). Phenol has attracted great interest as it is the chromophore of the amino acid tyrosine and possesses a relatively strong UV absorption. Therefore, understanding its photodynamics provides a good starting point towards understanding numerous larger systems that incorporate the UV chromophore. While the isolated gas-phase dynamics are well established,[89-91] only recently has work begun on investigating the environmental effects on the excited state dynamics of phenol.[66,87,92] The understanding of phenol's photodynamics has also been invaluable as it is the archetype of other UV chromophores also present as subunits in biomolecules. Phenol has been shown to have access to a range of relaxation pathways, including radical formation *via* fission of the O–H bond. The solvation effects upon phenol are minimal in the non-polar solvent, cylohexane, with only slight changes occurring to the excited state lifetime, while studies in water show that phenol undergoes an electron transfer to the solvent.[92] Like phenol, guaiacol (2-methoxyphenol) has been studied in the isolated gas-phase,[93,94] and in the solution-phase.[65] In the gas-phase guaiacol differs to the relaxation of phenol as the elimination of hydrogen does not occur. This is due to the intramolecular hydrogen bond between the hydroxyl and methoxy groups, which prevents the O–H bond undergoing fission. Upon solvation, guaiacol displays solvent dependant dynamics. In a non-polar solvent, the excited state dynamics of guaiacol are similar to the gas-phase; in contrast, in a polar solvent radical formation occurs. As such, studying the role the environment has on the photodynamics of such phenolic species is crucial and forms one of the central premises of this thesis, best illustrated in Chapter 3.

1.6 Photoprotection

Biology has always had to contend with constant exposure to UV radiation.[95,96] While the majority of solar UV photons are either scattered or absorbed by the atmosphere, mainly by ozone, a significant amount still reaches the Earth's surface. This constant bombardment of UV light presents an interesting problem as many biomolecules contain UV chromophores and thus have relatively high UV absorption cross-sections.[52,70,97,98] Fortunately, natural selection appears to have led to the construction of biomolecules

with relatively high photostability while still maintaining function.[82,97,99] This has led to great interest into the photodynamics of these molecules, in an effort to unravel their photostability, and indeed much work has been performed upon them. The main thrust of this work has been towards understanding DNA, ranging from individual nucleobases to DNA strands.[56,82,99,100] This has highlighted that, while non-destructive pathways occur readily with high quantum yields, destructive pathways are still present and occur with a non-negligible yield.[101,102] Luckily nature has provided cells with a plethora of mechanisms to deal with any photodamage inflicted to DNA, *via* repair mechanisms[103] or programmed cell death.[104] Yet even with these preventative measures, the damage can lead to severe consequences, *e.g.* formation of cancerous cells.[105-107] As a result, natural and synthetic pre-emptive measures are also employed in order to reduce the amount of UV exposure that these vital molecules experience.

The natural photoprotection system employed by human skin is a group of pigments called melanins.[105,108,109] While several melanin pigments exist in various locations within the body, only two are of concern in the skin: eumelanin and pheomelanin. Eumelanin is a large heterogeneous polymer that appears brown/black in colour depending on the component monomers and is generally considered to be the molecule responsible for the skin's photoprotection, although some studies suggest it has phototoxic properties.[110] Pheomelanin is another large heterogeneous polymer and is pink/red in colour, though unlike eumelanin it is thought to be a photosensitizer, which seems counter-intuitive to be used in part of the skins photoprotective mechanism. The levels of each melanin pigment are heavily dependent on the phenotype of the individual person.[102,103] People originating from areas with high levels of UV, like equatorial regions of the planet, tend to have high ratios of eumelanin, while people in more northern climates where UV levels are comparatively lower tend to have a reduced eumelanin level and higher levels of pheomelanin.[111,112] The reason for the differing composition and ratios of melanin is due to the fact that the body needs a certain amount of UV exposure, as UV is used in the body's production of vitamin D, therefore a trade-off is needed.[113,114] Under abnormally high amounts of UV exposure, the body will respond by expressing an increased amount of these pigments, often referred to as tanning, though this is a delayed response.[109,115] Due to this delayed response during which damage could have occurred, coupled with the potential phototoxicity of melanins, much work has been done in the production of synthetic sunscreening agents to bolster the body's natural photoprotection.[116,117]

While there are many studies looking at how effective these synthetic sunscreening agents are at protecting against UV, the understanding of the photodynamics of these molecules is lacking. The need for understanding these photodynamics has become more and more pertinent as recent studies have highlighted possible issues with some current sunscreening agents.[118-123] These issues include photoallergenic responses, interruption of various biological processes and the formation of reactive oxygen species due to photodegradation of the sunscreening agent. There has been a push in recent years towards unravelling the photodynamics of various sunscreening agents, though much work remains to be done.[67,124-127] In response to this, the work presented in Chapter 4 targets the photodynamics of sunscreening agents.

1.7 Two-Photon Activation

Ruthenium poly-pyridyl complexes have garnered interest in several areas such as cytotoxic action,[128,129] fluorescence imaging,[128,130] light-emitting devices,[131-133] light-harvesting[134,135] and photodynamic therapy.[136-139] The area of interest in this thesis is photodynamic therapy, where an inert precursor drug is activated with light, releasing or forming the medicinal compound. The afforded spatial control limits possible side effects to the immediate area of irradiated tissue,[140,141] and also has the potential to generate unique reactive species that might otherwise be biologically incompatible *i.e.* caged delivery.[142-144] Furthermore these are of particular use in treatments for when the above photoprotective mechanisms fail. Here we focus on activation by ligand dissociation where the leaving ligand is generally designed to have medical use or convert the metal complex into an active compound. Ideally, these light activated complexes should be activatable within the spectral window of 620 - 1000 nm; this region is commonly referred to as the therapeutic window.[145-147] This is the region in the electromagnetic spectrum which the tissues within the body have a reduced absorption and therefore allow light to penetrate deeper into the body. Unfortunately, the absorption of these metal-complexes tends to be towards the bluer region of the visible spectrum; outside of the therapeutic window. Serendipitously the TPA region of these molecules resides within the therapeutic window making it possible to use this as method of activation instead.[148,149] Indeed several irradiation studies have shown that activation of these complexes occurs *via* either OPA or TPA,[150] though whether the initial photodynamics differ between OPA or TPA has yet to be investigated. From a precursor drug design point of view, it is imperative to understand the initial activation mechanism following TPA for such species. Such knowledge will hopefully provide a platform for the future design of more effective PDT agents (*e.g.* optimum choice of substituents).[151] The

focus of the third and final results chapter is on developing an appreciation on the differences that exist, if any, between OPA and TPA in a well-studied photoactive Ru^{II} complex.

1.8 Summary

To summarize this introductory chapter, we have had a brief historical overview of spectroscopy, which has then been followed by the rules governing molecular absorption and the various fates of the molecule after absorption. Following this, the basic premise of the techniques employed within this thesis have been explained, while the solution-phase technique will be examined in much greater depth later in this thesis. Finally, a brief introduction has been given on the three areas of interest presented within this thesis. These are as follows: the comparison of the gas- and solution-phase photodynamics of simple UV-chromophores, the importance of photoprotective molecules, and the use of two-photon activation of potentially therapeutic ruthenium poly-pyridyl complexes.

The remaining parts of this thesis are structured in the following way. Chapter 2 explains the experimental setup used to obtain the solution-phase measurements in the ensuing chapters. Chapter 3 focuses on the comparison between the photodynamics of the UV-chromophore 4-*tert*-butylcatechol in the isolated gas-phase, and in the solution-phase. Chapter 4 explores the photodynamics of the sunscreening agents ferulic and caffeic acid in order to improve the understanding of potential photoprotective molecules. Chapter 5 builds upon previous OPA studies on the metal complex $[Ru(bpy)_2(NA)_2]^{2+}$, by performing TPA experiments and then comparing the differences in photoactivation methods following one- and two-photon activation. The thesis then ends with a conclusion and brief outlook at the future work built off the work presented here.

1.9 Bibliography

1. I. Newton, *Opticks: or a treatise of the reflexions, refractions, inflexions and colours of light*, First edn., 1704.
2. W. H. Wollaston, *Phil. Trans. R. Soc. Lond.*, 1802, **92**, 365-380.
3. J. F. W. Herschel, *Trans. Roc. Soc. Edinb.*, 1823, **9**, 445-460.
4. G. Kirchhoff, *Monatsberichte der Akademie der Wissenschaften zu Berlin*, 1859, 783-787.
5. J. J. Thomson, *Philos. Mag.*, 1897, **44**, 293-316.
6. N. Bohr, *Philos. Mag.*, 1913, **26**, 1-25.

7. R. G. W. Norrish and G. Porter, *Nature*, 1949, **164**, 658.
8. G. Porter, *Nobel Lecture*, 1967, 241-263.
9. T. H. Maiman, *Nature*, 1960, **187**, 493-494.
10. C. V. Shank and E. P. Ippen, *Appl. Phys. Lett.*, 1974, **24**, 373-375.
11. N. F. Scherer, J. L. Knee, D. D. Smith and A. H. Zewail, *J. Phys. Chem.*, 1985, **89**, 5141-5143.
12. M. Dantus, M. J. Rosker and A. H. Zewail, *J. Chem. Phys.*, 1988, **89**, 6128-6140.
13. A. H. Zewail, *J. Phys. Chem. A*, 2000, **104**, 5660-5694.
14. A. Beer, *Ann. Phys.*, 1852, **86**, 78-88.
15. P. W. Atkins and R. S. Friedman, *Molecular Quantum Mechanics*, Oxford University Press, United States of America, Fifth edn., 2011.
16. P. Atkins and J. de Paula, *Atkins' Physical Chemistry*, Oxford University Press, Great Britain, Eighth edn., 2006.
17. J. M. Hollas, *Modern Spectroscopy*, John Wiley & Sons Ltd, Great Britain, Fourth edn., 2004.
18. C. Eckart, *Phys. Rev.*, 1934, **46**, 383.
19. M. Born and R. Oppenheimer, *Ann. Physik*, 1927, **389**, 457-484.
20. W. Heisenberg, *Z. Phys.*, 1927, **43**, 172-198.
21. J. D. Graybeal, *Molecular Spectroscopy*, McGraw-Hill Book Company, United States of America, International edn., 1988.
22. J. M. Brown, *Molecular Spectroscopy*, Oxford University Press, United States of America, 1998.
23. R. C. Hilborn, *Am. J. Phys.*, 1982, **50**, 982.
24. J. Franck and E. G. Dymond, *T. Faraday Soc.*, 1926, **21**, 536-542.
25. E. U. Condon, *Phys. Rev.*, 1926, **28**, 1182.
26. E. U. Condon, *Phys. Rev.*, 1928, **32**, 858.
27. P. Klán and J. Wirz, *Photochemistry of Organic compounds: From Concepts to Practice*, John Wiley & Sons, Great Britain, 2009.
28. S. H. Lin, Y. Fujimura, H. J. Neusser and E. W. Schlag, *Multiphoton Spectroscopy of Molecules*, Academic Press, Inc., United States of America, 1984.
29. M. Göppert-Mayer, *Ann. Physik*, 1931, **401**, 273.
30. G. S. He, L.-S. Tan, Q. Zheng and P. N. Prasad, *Chem. Rev.*, 2008, **108**, 1245-1330.
31. M. Pawlicki, H. A. Collins, R. G. Denning and H. L. Anderson, *Angew. Chem. Int. Ed.*, 2009, **48**, 3244-3266.
32. A. Jablonski, *Nature*, 1933, **131**, 21.
33. K. L. Reid, *Int. Rev. Phys. Chem.*, 2008, **27**, 607-628.

34. I. V. Hertel and W. Radloff, *Rep. Prog. Phys.*, 2006, **69**, 1897.
35. J. C. Owrutsky, D. Raftery and R. M. Hochstrasser, *Annu. Rev. Phys. Chem.*, 1994, **45**, 519-555.
36. C. N. Banwell and E. M. McCash, *Fundamentals of Molecular Spectroscopy*, McGraw-Hill Book Company, United Kingdom, Fourth edn., 1994.
37. D. Boyall and K. L. Reid, *Chem. Soc. Rev.*, 1997, **26**, 223-232.
38. J. R. Lakowicz, *Principles of Fluorescence Spectroscopy*, Springer Science & Business Media, United States of America, Third edn., 2006.
39. T. Itoh, *Chem. Rev.*, 2012, **112**, 4541-4568.
40. M. Kasha, *Discuss. Faraday Soc.*, 1950, **9**, 14-19.
41. A. I. Prokof'ev, N. N. Bubnov, S. P. Solodovnikov and M. I. Kabachnik, *Tetrahedron Lett.*, 1973, **14**, 2479-2480.
42. R. Englman and J. Jortner, *Mol. Phys.*, 1970, **18**, 145-164.
43. M. Bixon and J. Jortner, *J. Chem. Phys.*, 1968, **48**, 715-726.
44. N. J. Turro, *Modern molecular photochemistry*, University science books, 1991.
45. D. R. Yarkony, *Rev. Mod. Phys.*, 1996, **68**, 985-1011.
46. G. A. Worth and L. S. Cederbaum, *Annu. Rev. Phys. Chem.*, 2004, **55**, 127-158.
47. W. Domcke, D. R. Yarkony and H. Köppel, *Conical intersections: theory, computation and experiment*, World Scientific, 2011.
48. D. R. Yarkony, *Acc. Chem. Res.*, 1998, **31**, 511-518.
49. S. Matsika and P. Krause, *Annu. Rev. Phys. Chem.*, 2011, **62**, 621-643.
50. D. Polli, P. Altoè, O. Weingart, K. M. Spillane, C. Manzoni, D. Brida, G. Tomasello, G. Orlandi, P. Kukura and R. A. Mathies, *Nature*, 2010, **467**, 440-443.
51. H. J. Krautwald, L. Schnieder, K. H. Welge and M. N. Ashfold, *Farad. Discuss.*, 1986, **82**, 99-110.
52. G. M. Roberts and V. G. Stavros, *Chem. Sci.*, 2014, **5**, 1698-1722.
53. M. N. R. Ashfold, B. Cronin, A. L. Devine, R. N. Dixon and M. G. D. Nix, *Science*, 2006, **312**, 1637-1640.
54. E. Pines, D. Huppert and N. Agmon, *J. Chem. Phys.*, 1988, **88**, 5620-5630.
55. H.-H. Limbach, J. M. Lopez and A. Kohen, *Phil. Trans. R. Soc. B Biol. Sci.*, 2006, **361**, 1399-1415.
56. C. Wan, T. Fiebig, O. Schiemann, J. K. Barton and A. H. Zewail, *Proc. Natl. Acad. Sci.*, 2000, **97**, 14052-14055.
57. J. Peon, G. C. Hess, J.-M. L. Pecourt, T. Yuzawa and B. Kohler, *J. Phys. Chem. A*, 1999, **103**, 2460-2466.

58. L. A. Baker, M. D. Horbury, S. E. Greenough, F. Allais, P. S. Walsh, S. Habershon and V. G. Stavros, *J. Phys. Chem. Lett.*, 2016, **7**, 56-61.
59. Y. Liu, D. B. Turner, T. N. Singh, A. M. Angeles-Boza, A. Chouai, K. R. Dunbar and C. Turro, *J. Am. Chem. Soc.*, 2009, **131**, 26-27.
60. N. H. Damrauer, G. Cerullo, A. Yeh, T. R. Boussie, C. V. Shank and J. K. McCusker, *Science*, 1997, **275**, 54-57.
61. D. A. Lutterman, P. K.-L. Fu and C. Turro, *J. Am. Chem. Soc.*, 2006, **128**, 738-739.
62. U. Bach, D. Lupo, P. Comte, J. Moser, F. Weissörtel, J. Salbeck, H. Spreitzer and M. Grätzel, *Nature*, 1998, **395**, 583-585.
63. S. De, T. Pascher, M. Maiti, K. G. Jespersen, T. Kesti, F. Zhang, O. Inganäs, A. Yartsev and V. Sundström, *J. Am. Chem. Soc.*, 2007, **129**, 8466-8472.
64. M. Vengris, D. S. Larsen, M. A. van der Horst, O. F. A. Larsen, K. J. Hellingwerf and R. van Grondelle, *J. Phys. Chem. B*, 2005, **109**, 4197-4208.
65. S. E. Greenough, M. D. Horbury, J. O. F. Thompson, G. M. Roberts, T. N. V. Karsili, B. Marchetti, D. Townsend and V. G. Stavros, *Phys. Chem. Chem. Phys.*, 2014, **16**, 16187-16195.
66. S. J. Harris, D. Murdock, Y. Zhang, T. A. Oliver, M. P. Grubb, A. J. Orr-Ewing, G. M. Greetham, I. P. Clark, M. Towrie, S. E. Bradforth and M. N. R. Ashfold, *Phys. Chem. Chem. Phys.*, 2013, **15**, 6567-6582.
67. L. A. Baker, M. D. Horbury, S. E. Greenough, P. M. Coulter, T. N. V. Karsili, G. M. Roberts, A. J. Orr-Ewing, M. N. R. Ashfold and V. G. Stavros, *J. Phys. Chem. Lett.*, 2015, **6**, 1363-1368.
68. U. Megerle, I. Pugliesi, C. Schriever, C. F. Sailer and E. Riedle, *Appl. Phys. B*, 2009, **96**, 215-231.
69. R. Berera, R. van Grondelle and J. T. Kennis, *Photosynth. Res.*, 2009, **101**, 105-118.
70. M. Staniforth and V. G. Stavros, *Proc. R. Soc. A*, 2013, **469**, 20130458.
71. R. De Nalda, J. Izquierdo, J. Durá and L. Bañares, *J. Chem. Phys.*, 2007, **126**, 021101.
72. K. L. Wells, G. Perriam and V. G. Stavros, *J. Chem. Phys.*, 2009, **130**, 074308.
73. D. J. Hadden, C. A. Williams, G. M. Roberts and V. G. Stavros, *Phys. Chem. Chem. Phys.*, 2011, **13**, 4494-4499.
74. W. Demtröder, *Laser spectroscopy: basic concepts and instrumentation*, Springer Science & Business Media, United States of America, 2013.
75. M. Ashfold and J. Howe, *Annu. Rev. Phys. Chem.*, 1994, **45**, 57-82.
76. D. M. Neumark, *Annu. Rev. Phys. Chem.*, 2001, **52**, 255-277.
77. A. Corani, A. Pezzella, T. r. Pascher, T. Gustavsson, D. Markovitsi, A. Huijser, M. d'Ischia and V. Sundström, *J. Phys. Chem. Lett.*, 2013, **4**, 1383-1388.

78. A. Huijser, A. Pezzella and V. Sundström, *Phys. Chem. Chem. Phys.*, 2011, **13**, 9119-9127.
79. M. Gauden, A. Pezzella, L. Panzella, M. T. Neves-Petersen, E. Skovsen, S. B. Petersen, K. M. Mullen, A. Napolitano, M. d'Ischia and V. Sundstrom, *J. Am. Chem. Soc.*, 2008, **130**, 17038-17043.
80. M. Gauden, A. Pezzella, L. Panzella, A. Napolitano, M. d'Ischia and V. Sundström, *J. Phys. Chem. B*, 2009, **113**, 12575-12580.
81. M. S. de Vries and P. Hobza, *Annu. Rev. Phys. Chem.*, 2007, **58**, 585-612.
82. S. Ullrich, T. Schultz, M. Z. Zgierski and A. Stolow, *Phys. Chem. Chem. Phys.*, 2004, **6**, 2796-2801.
83. M. G. D. Nix, A. L. Devine, B. Cronin and M. N. R. Ashfold, *J. Chem. Phys.*, 2007, **126**, 124312.
84. K. L. Wells, D. J. Hadden, M. G. D. Nix and V. G. Stavros, *J. Phys. Chem. Lett.*, 2010, **1**, 993-996.
85. A. Iqbal and V. G. Stavros, *J. Phys. Chem. Lett.*, 2010, **1**, 2274-2278.
86. N. L. Evans and S. Ullrich, *J. Phys. Chem. A*, 2010, **114**, 11225-11230.
87. Y. Zhang, T. A. A. Oliver, M. N. R. Ashfold and S. E. Bradforth, *Farad. Discuss.*, 2012, **157**, 141-163.
88. T. A. A. Oliver, Y. Zhang, M. N. R. Ashfold and S. E. Bradforth, *Farad. Discuss.*, 2011, **150**, 439-458.
89. G. M. Roberts, A. S. Chatterley, J. D. Young and V. G. Stavros, *J. Phys. Chem. Lett.*, 2012, **3**, 348-352.
90. R. N. Dixon, T. A. Oliver and M. N. R. Ashfold, *J. Chem. Phys.*, 2011, **134**, 194303.
91. C.-M. Tseng, Y. T. Lee and C.-K. Ni, *J. Chem. Phys.*, 2004, **121**, 2459-2461.
92. T. A. A. Oliver, Y. Zhang, A. Roy, M. N. R. Ashfold and S. E. Bradforth, *J. Phys. Chem. Lett.*, 2015, **6**, 4159-4164.
93. A. S. Chatterley, J. D. Young, D. Townsend, J. M. Zurek, M. J. Paterson, G. M. Roberts and V. G. Stavros, *Phys. Chem. Chem. Phys.*, 2013, **15**, 6879-6892.
94. J. D. Young, M. Staniforth, J. C. Dean, G. M. Roberts, F. Mazzoni, T. N. V. Karsili, M. N. R. Ashfold, T. S. Zwier and V. G. Stavros, *J. Phys. Chem. Lett.*, 2014, **5**, 2138-2143.
95. N. D. Paul and D. Gwynn-Jones, *Trends Ecol. Evol.*, 2003, **18**, 48-55.
96. M. M. Caldwell, J. Bornman, C. Ballaré, S. D. Flint and G. Kulandaivelu, *Photochem. Photobiol. Sci.*, 2007, **6**, 252-266.
97. A. Sobolewski and W. Domcke, *Phys. Chem. Chem. Phys.*, 2010, **12**, 4897-4898.
98. C. E. Crespo-Hernández, B. Cohen, P. M. Hare and B. Kohler, *Chem. Rev.*, 2004, **104**, 1977-2019.

99. C. T. Middleton, K. de La Harpe, C. Su, Y. K. Law, C. E. Crespo-Hernández and B. Kohler, *Annu. Rev. Phys. Chem.*, 2009, **60**, 217-239.
100. G. Groenhof, L. V. Schafer, M. Boggio-Pasqua, M. Goette, H. Grubmuller and M. A. Robb, *J. Am. Chem. Soc.*, 2007, **129**, 6812-6819.
101. F. De Gruijl, *Eur. J. Cancer*, 1999, **35**, 2003-2009.
102. G. P. Pfeifer, Y.-H. You and A. Besaratinia, *Mutat. Res-Fund. Mol. M.*, 2005, **571**, 19-31.
103. P. C. Hanawalt, E. C. Friedberg and C. F. Fox, *DNA repair mechanisms*, Academic Press, United States of America, 1978.
104. D. Kulms and T. Schwarz, *Photodermatol. Photoimmunol. Photomed.*, 2000, **16**, 195-201.
105. J. P. Ortonne, *Br. J. Dermatol.*, 2002, **146**, 7-10.
106. R. S. Mason and J. Reichrath, *Anticancer Agents Med. Chem.*, 2013, **13**, 83-97.
107. S. González, M. Fernández-Lorente and Y. Gilaberte-Calzada, *Clin. Dermatol.*, 2008, **26**, 614-626.
108. J. Borovansky and P. A. Riley, *Melanins and Melanosomes: Biosynthesis, Structure, Physiological and Pathological Functions*, John Wiley & Sons, Germany, 2011.
109. M. Brenner and V. J. Hearing, *Photochem. Photobiol.*, 2008, **84**, 539-549.
110. S. Premi, S. Wallisch, C. M. Mano, A. B. Weiner, A. Bacchiocchi, K. Wakamatsu, E. J. H. Bechara, R. Halaban, T. Douki and D. E. Brash, *Science*, 2015, **347**, 842-847.
111. N. Kollias, R. M. Sayre, L. Zeise and M. R. Chedekel, *J. Photochem. Photobiol. B*, 1991, **9**, 135-160.
112. A. Slominski, D. J. Tobin, S. Shibahara and J. Wortsman, *Physiol. Rev.*, 2004, **84**, 1155-1228.
113. M. F. Holick, *J. Cell. Biochem.*, 2003, **88**, 296-307.
114. J. Reichrath, *Sunlight, Vitamin D and Skin Cancer*, Springer Science+Business Media, United States of America, 2008.
115. N. Agar and A. R. Young, *Mutat. Res-Fund. Mol. M.*, 2005, **571**, 121-132.
116. S. Forestier, *J. Am. Acad. Dermatol.*, 2008, **58**, S133-S138.
117. F. Urbach, *J. Photochem. Photobiol. B*, 2001, **64**, 99-104.
118. M. Loden, H. Beitner, H. Gonzalez, D. W. Edström, U. Åkerström, J. Austad, I. Buraczewska-Norin, M. Matsson and H. C. Wulf, *Br. J. Dermatol.*, 2011, **165**, 255-262.
119. M. E. Burnett and S. Q. Wang, *Photodermatol. Photoimmunol. Photomed.*, 2011, **27**, 58-67.

120. K. Skotarczak, A. Osmola-Mańkowska, M. Lodyga, A. Polańska, M. Mazur and Z. Adamski, *Eur. Rev. Med. Pharmacol. Sci.*, 2015, **19**, 98-112.
121. S. Afonso, K. Horita, J. P. S. e Silva, I. F. Almeida, M. H. Amaral, P. A. Lobão, P. C. Costa, M. S. Miranda, J. C. G. E. da Silva and J. M. S. Lobo, *J. Photochem. Photobiol. B*, 2014, **140**, 36-40.
122. M. S. Matsui, A. Hsia, J. D. Miller, K. Hanneman, H. Scull, K. D. Cooper and E. Baron, *J. Investig. Dermatol. Symp. Proc*, 2009, **14**, 56-59.
123. A. Saija, A. Tomaino, D. Trombetta, A. De Pasquale, N. Uccella, T. Barbuzzi, D. Paolino and F. Bonina, *Int. J. Pharm.*, 2000, **199**, 39-47.
124. E. M. M. Tan, M. Hilbers and W. J. Buma, *J. Phys. Chem. Lett.*, 2014, **5**, 2464-2468.
125. A. Dunkelberger, R. D. Kieda, B. M. Marsh and F. F. Crim, *J. Phys. Chem. A*, 2015, **119**, 6155-6161.
126. L. A. Baker, M. D. Horbury, S. E. Greenough, M. N. Ashfold and V. G. Stavros, *Photochem. Photobiol. Sci.*, 2015, **14**, 1814-1820.
127. M. T. Ignasiak, C. Houée-Levin, G. Kciuk, B. Marciniak and T. Pedzinski, *ChemPhysChem*, 2015, **16**, 628-633.
128. M. R. Gill and J. A. Thomas, *Chem. Soc. Rev.*, 2012, **41**, 3179-3192.
129. A. Yadav, T. Janaratne, A. Krishnan, S. S. Singhal, S. Yadav, A. S. Dayoub, D. L. Hawkins, S. Awasthi and F. M. MacDonnell, *Mol. Cancer Ther.*, 2013, **12**, 643-653.
130. V. Fernández-Moreira, F. L. Thorp-Greenwood and M. P. Coogan, *Chem. Commun.*, 2010, **46**, 186-202.
131. H. Rudmann and M. F. Rubner, *J. Appl. Phys.*, 2001, **90**, 4338-4345.
132. H. Rudmann, S. Shimada and M. F. Rubner, *J. Am. Chem. Soc.*, 2002, **124**, 4918-4921.
133. E. Holder, B. M. W. Langeveld and U. S. Schubert, *Adv. Mater.*, 2005, **17**, 1109-1121.
134. M. Grätzel, *Inorg. Chem.*, 2005, **44**, 6841-6851.
135. P. D. Frischmann, K. Mahata and F. Würthner, *Chem. Soc. Rev.*, 2013, **42**, 1847-1870.
136. C. Mari and G. Gasser, *CHIMIA*, 2015, **69**, 176-181.
137. E. K. Pefkianakis, T. A. Theodossiou, D. K. Toubanaki, E. Karagouni, P. Falaras, K. Papadopoulos and G. C. Vougioukalakis, *Photochem. Photobiol.*, 2015, **91**, 1191-1202.
138. T. J. Dougherty, *Photodynamic Therapy: Methods and Protocols*, Humana Press, United States of America, 2010.
139. J. D. Knoll, B. A. Albani and C. Turro, *Acc. Chem. Res.*, 2015, **48**, 2280-2287.

140. P. Agostinis, K. Berg, K. A. Cengel, T. H. Foster, A. W. Girotti, S. O. Gollnick, S. M. Hahn, M. R. Hamblin, A. Juzeniene and D. Kessel, *CA-Cancer J. Clin.*, 2011, **61**, 250-281.
141. P. Mroz, A. Yaroslavsky, G. B. Kharkwal and M. R. Hamblin, *Cacners*, 2011, **3**, 2516-2539.
142. L. Zayat, C. Calero, P. Alborés, L. Baraldo and R. Etchenique, *J. Am. Chem. Soc.*, 2003, **125**, 882-883.
143. K. L. Ciesienski and K. J. Franz, *Angew. Chem. Int. Ed.*, 2011, **50**, 814-824.
144. M. A. Sgambellone, A. David, R. N. Garner, K. R. Dunbar and C. Turro, *J. Am. Chem. Soc.*, 2013, **135**, 11274-11282.
145. L. Carroll and T. R. Humphreys, *Clin. Dermatol.*, 2006, **24**, 2-7.
146. K. Ogawa and Y. Kobuke, *Anti-Cancer Agents in Medicinal Chemistry (Formerly Current Medicinal Chemistry-Anti-Cancer Agents)*, 2008, **8**, 269-279.
147. A. M. Smith, M. C. Mancini and S. Nie, *Nat. Nanotechnol.*, 2009, **4**, 710-711.
148. M. Four, D. Riehl, O. Mongin, M. Blanchard-Desce, L. M. Lawson-Daku, J. Moreau, J. Chauvin, J. A. Delaire and G. Lemercier, *Phys. Chem. Chem. Phys.*, 2011, **13**, 17304-17312.
149. C. Girardot, B. Cao, J.-C. Mulatier, P. L. Baldeck, J. Chauvin, D. Riehl, J. A. Delaire, C. Andraud and G. Lemercier, *ChemPhysChem*, 2008, **9**, 1531-1535.
150. M. Salierno, E. Marceca, D. S. Peterka, R. Yuste and R. Etchenique, *J. Inorg. Biochem.*, 2010, **104**, 418-422.
151. S. E. Greenough, G. M. Roberts, N. A. Smith, M. D. Horbury, R. G. McKinlay, J. M. Żurek, M. J. Paterson, P. J. Sadler and V. G. Stavros, *Phys. Chem. Chem. Phys.*, 2014, **16**, 19141-19155.

2. Experimental

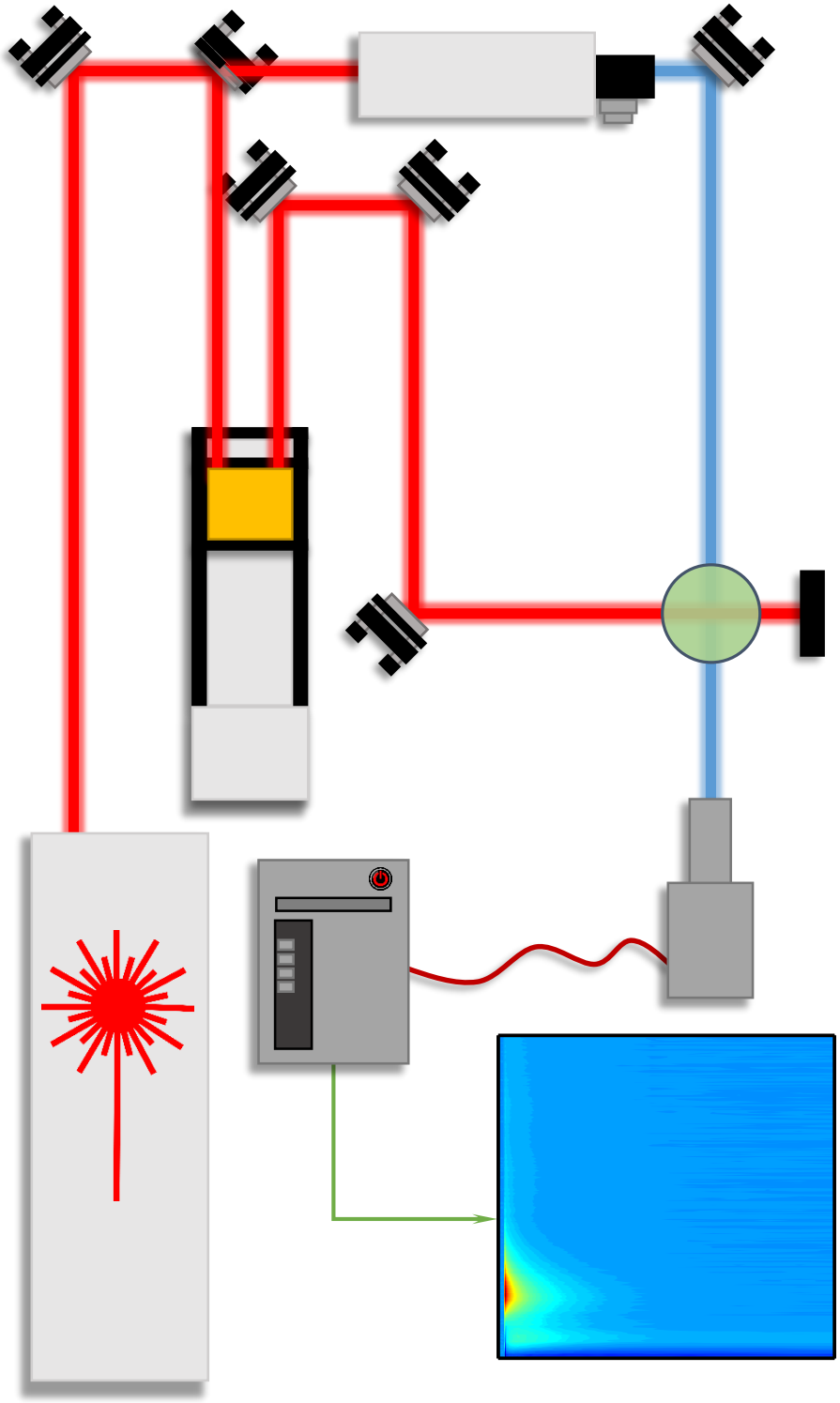

"Any sufficiently advanced technology is indistinguishable from magic."

Arthur C. Clarke

2.1 Introduction

In this chapter, a detailed overview of the transient electronic absorption spectroscopy (TEAS) setup is given. This setup is used for all the ultrafast solution-phase measurements presented in this thesis (Chapters 3-5). The description also covers several systems that are shared with the experimental setup of the gas-phase measurements presented in Chapter 3, though details are not provided beyond what has already being discussed in Chapter 1.

2.1.1 Laser System

Here we shall briefly discuss the generation of the laser pulses used within the TEAS experiment (Figure 2.1). The initial femtosecond laser pulses are generated by a commercially available Tsunami (Newport Spectra-Physics) Ti:sapphire (Ti^{3+} doped Al_2O_3) oscillator.[1] This produces pulses centred at 800 nm with a 35-40 nm bandwidth, as shown in Figure 2.2, and a pulse duration of ~80 fs. The repetition rate of the pulses is ~75 MHz, with a pulse power of ~3.9 nJ per pulse (~300 mW). To generate these pulses, the Ti:sapphire lasing medium is pumped by a 532 nm continuous wave laser beam generated by a commercially available Millennia Pro (Newport Spectra-Physics). The Millennia Pro is a diode (gallium-aluminium-arsenide, 809 nm) pumped solid state laser that uses Nd:YVO_4 as the lasing medium, producing an initial wavelength of 1064 nm. This is then frequency-doubled in a lithium triborate crystal, producing a beam power of 40 W at 532 nm. While this system gives us our femtosecond pulses, they are produced with too low a pulse power to be useful. Therefore, in order to generate pulses of the power required for our experiments, the oscillator feeds its output into a regenerative amplifier (Newport Spectra-Physics Spitfire Pro). Rather than amplify every pulse produced by the oscillator, 1 in every 75,000 pulses is selected, giving a 1 kHz amplified pulse train. These pulses are amplified utilising the output of another Ti:sapphire lasing medium. This lasing medium is pumped by a commercially available laser, Empower (Newport Spectra-Physics), a diode (gallium-aluminium-arsenide, 809 nm) pumped solid state laser, which uses a laser medium of Nd:YLF, to give a continuous wave 1053 nm beam; this beam is again frequency-doubled to give 527 nm. Rather than use the continuous wave output to amplify the femtosecond pulses, it is instead electronically chopped to produce a 1 kHz pulsed beam with a pulse duration of 100 ns, with 15 mJ/per pulse (15 W). With this amplification, the regenerative amplifier outputs a pulse power of 3 mJ (3 W) at 800 nm, with a pulse duration of approximately 40 fs.

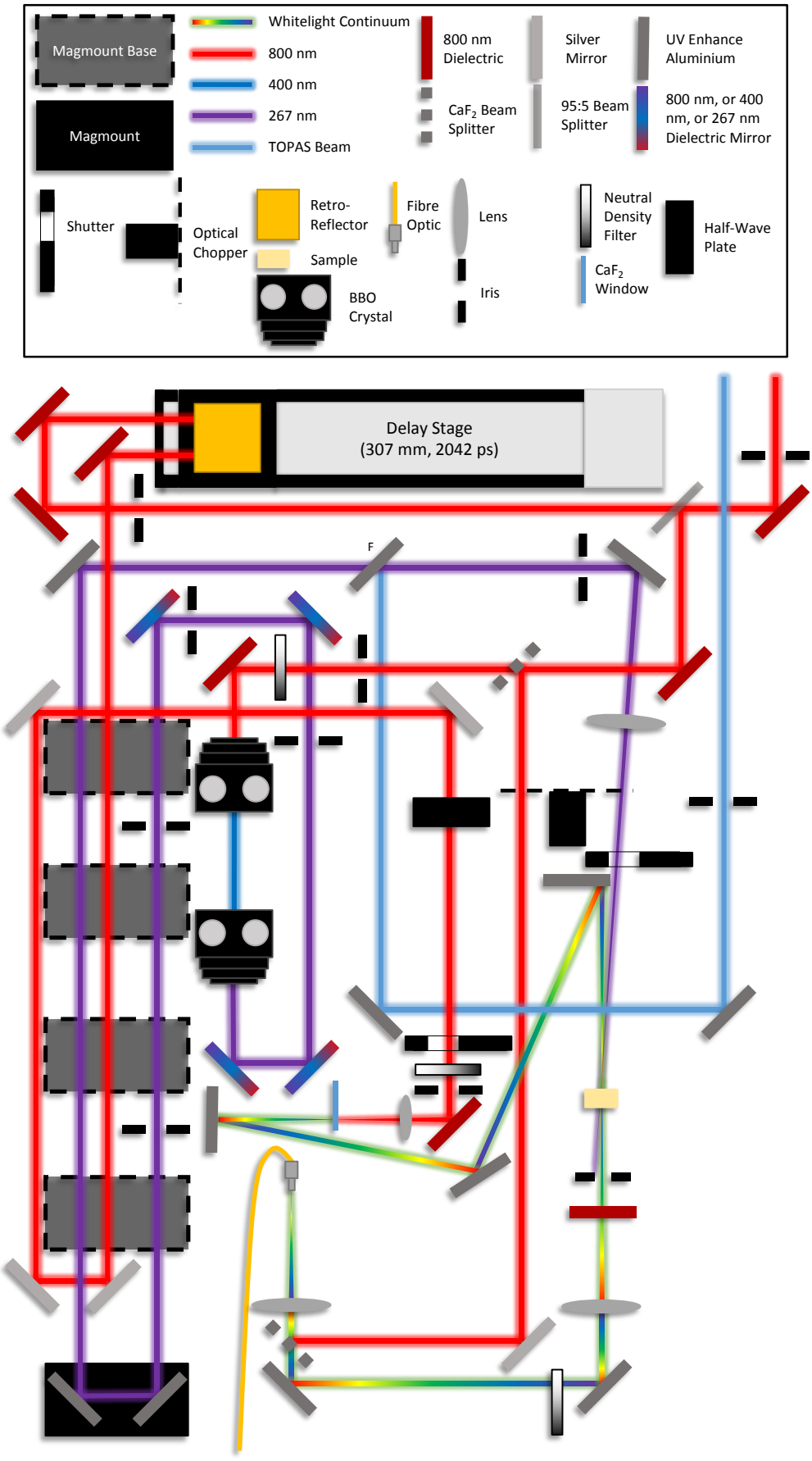

Figure 2.1 A schematic of the TEAS optical table. Various sections of this table are shown in greater detail later in this chapter. F denotes that the mirror is mounted on a flip mount.

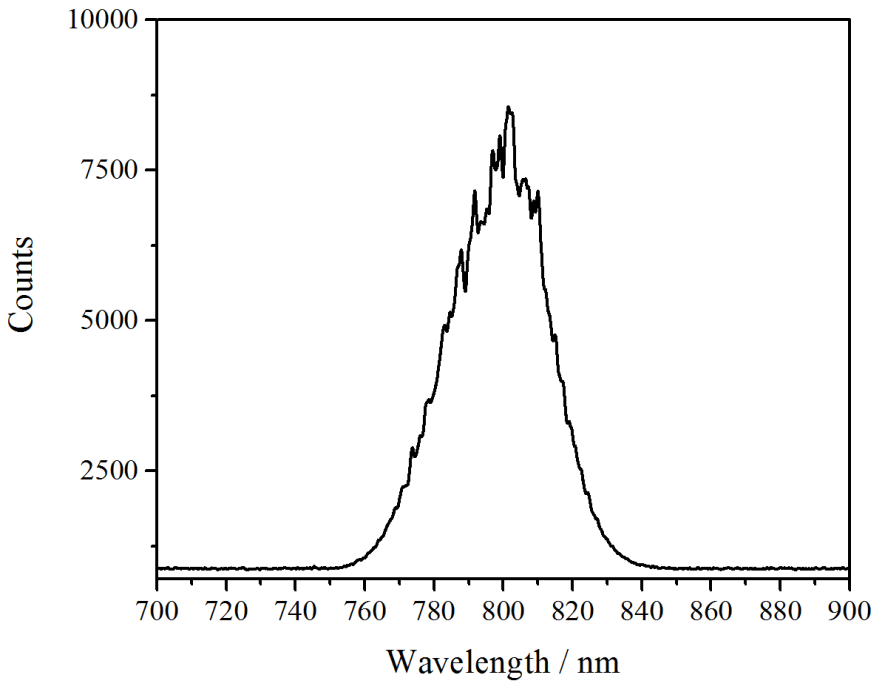

Figure 2.2 Spectral profile of the 800 nm pulse from the Tsunami.

This beam is referred to as the fundamental beam, which is used to generate the pump and probe pulses described below.

The fundamental beam produced by the regenerative amplifier is required to seed multiple beam lines, therefore it is split into multiple fractions of differing power (Figure 2.3). First it is split into two beams, one with a power of 1 W and the other with a power of 2 W; the 1 W beam is not used in the TEAS experimental setup.[8] The 2 W beam is further split into two 1 W beams. One of these is used to seed the optical parametric amplifier (TOPAS-C, Light Conversion) for the variable wavelength pump source,[9] while the second is sent to the TEAS setup. Once the 1 W fundamental beam is fed onto the TEAS table, it is further split into a 950 mW beam and 50 mW beam by a 95:5 beam splitter, with the 50 mW beam used to seed the generation of the white light continuum probe pulse. The 950 mW beam is further split by a 1 mm CaF_2 window to give two beams, one has a power of ~5 mW and is used as a reference and the remaining ~945 mw is used for harmonic generation, another possible pump pulse source.

2.2 Non-linear Processes

The generation of the pump and probe pulses that are used within the spectroscopic measurements are reliant on several non-linear processes. Therefore, a brief description

[8] This beam is used to seed the pump source, another TOPAS-C or a harmonic generation setup, for the TR-VMI and TR-IY experiments.
[9] This TOPAS-C is also used as the probe source for the TR-VMI and TR-IY experiments.

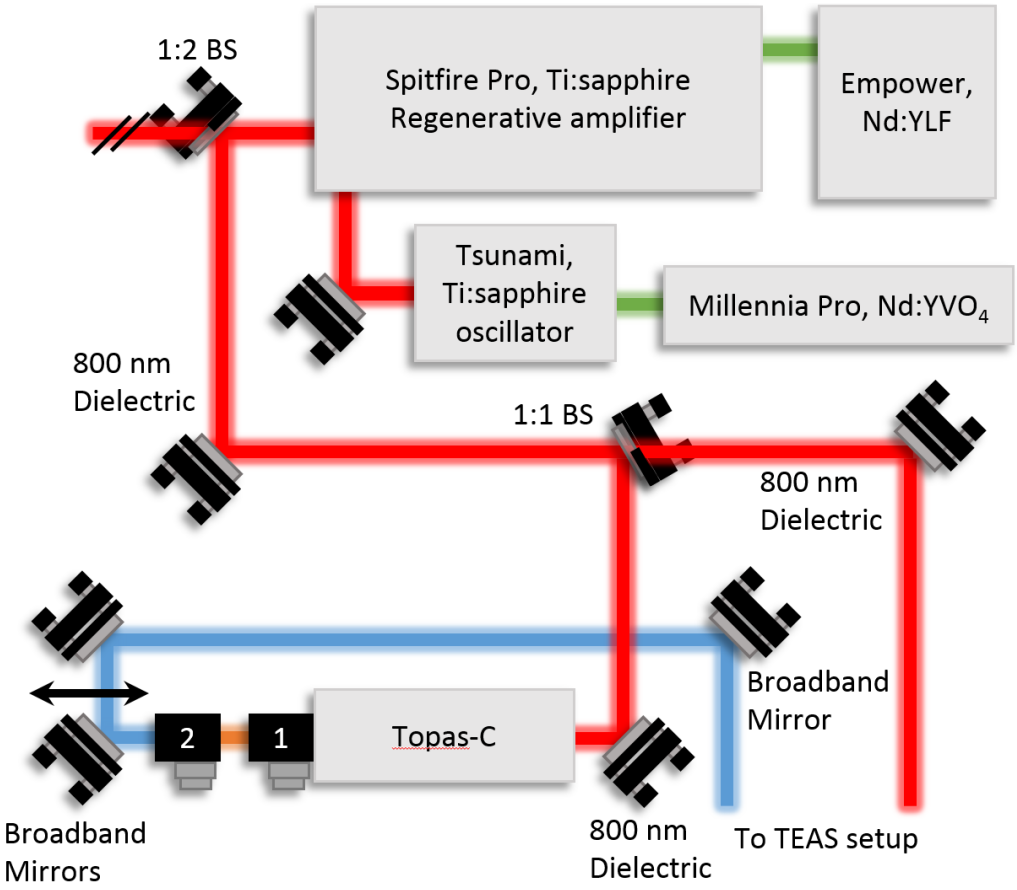

Figure 2.3 A schematic of the initial fundamental laser beam, followed by the various beam-splits that occur. The initial path of the TOPAS-C pump source (*vide infra*) is also shown. The beam paths of the 800 nm fundamental (red line), 527 and 532 nm pump laser's beams (green line), TOPAS-C intermediate beam before final mixing (orange line) and the final beam generated by the TOPAS-C with wavelengths 230 – 2100 nm (blue line) are shown. (1) First TOPAS-C mixer and (2) second TOPAS-C mixer. The double headed arrow shows the pair of mirrors used to match the TOPAS path length with the probe path length. BS = beam splitter.

of these non-linear affects is warranted. First, we shall consider how light is typically described when travelling through a medium that is linearly polarizable. The electric field ($\boldsymbol{E}$) component of light passing through a medium will have an effect upon the medium's dielectric polarization, ($\boldsymbol{P}$). This can be approximated by the following equation:[2,3]

$$\boldsymbol{P} = \varepsilon_0 \chi \boldsymbol{E} \tag{2.1}$$

where ε_0 is the vacuum permittivity and χ is the electric susceptibility of the medium. However, this equation only captures the linear response to light passing through the medium. For intense laser pulses, such as those used in the experiments presented in this thesis, non-linear responses from the medium become important. Therefore this simplified equation can be expanded from the linear model to give a nonlinear model for susceptibility that takes higher order electric fields into account:[2,3]

$$(\boldsymbol{P}^{(1)} + \boldsymbol{P}^{(2)} + \boldsymbol{P}^{(3)} \ldots + \boldsymbol{P}^{(n)}) = \varepsilon_0(\chi^{(1)}\boldsymbol{E} + \chi^{(2)}\boldsymbol{E}^2 + \chi^{(3)}\boldsymbol{E}^3 \ldots + \chi^{(n)}\boldsymbol{E}^n) \quad (2.2)$$

Here $\boldsymbol{P}^{(n)}$ is the n^{th} (n=1,2,3…) order nonlinear polarization and $\chi^{(n)}$ is the n^{th} order nonlinear susceptibility. It is possible that the electric field component can be provided by photons of differing wavelengths *i.e.* $\chi^{(2)}\boldsymbol{E}_{\lambda(1)}\boldsymbol{E}_{\lambda(2)}$ as well as photons of equal wavelengths. It is from these higher order terms that non-linear processes are derived.

2.2.1 Frequency Conversion

It is possible, through second order non-linear processes, to induce frequency conversions in the incident light to higher or lower frequencies under specific criteria.[3] Firstly, the medium has to display a second order non-linear dependence to the applied electric field. This requires the medium to be an asymmetric material, otherwise the changes in the $\boldsymbol{P}$ are symmetrical with changes in $\boldsymbol{E}$, leading to even order terms within Equation (2.2) becoming zero.[3] Secondly the phases of the incident photons need to be matched correctly. This can be achieved in several ways: a time-delay can be introduced between the photons involved in the conversion; altering the relative orientation of the medium's crystal structure compared to the photons polarization; or changing the angle of polarization between the photons.[3,4]

The specific non-linear processes invoked within the experimental setup for production of the pump-pulses from the fundamental beam are sum frequency generation (SFG), difference frequency generation (DFG) and optical parametric generation (OPG) (Figure 2.4).[10]

2.2.1.1. Sum Frequency Generation

SFG occurs when two-photons interact within a non-linear medium. The first photon induces an oscillation within the electron cloud of the material at the photon's frequency. The second photon then causes this oscillation to occur at a higher frequency that is equal to the sum of the two-photons, which is then followed by an emission of a photon at this new frequency (Figure 2.4 a)). A special case of SFG is when the two incident photons have the same frequency, referred to as second harmonic generation (SHG, Figure 2.4 b)). Further harmonics can be generated *e.g.* third harmonic and these occur when SFG occurs between a harmonic and the fundamental.[3]

[10] The TOPAS-C also makes use of a supercontinuum to generate certain wavelengths.

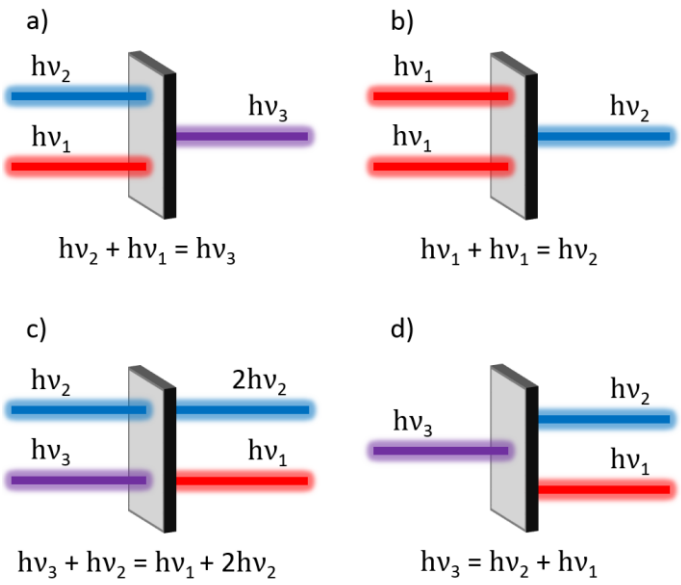

Figure 2.4 Schematic of possible 2nd order non-linear processes that are used in this thesis, a) SFG, b) SHG, c) DFG and d) OPG.

2.2.1.2. Difference Frequency Generation

DFG is similar to SFG, however, where SFG is the summation of the frequencies of two photons, DFG is the subtraction. However, in order to conserve energy, the process relies on stimulated emission. Initially the photon with the higher energy produces an excited state within the system, either a virtual or real state. Then the second photon with lower energy induces a stimulated emission from this state to a virtual state, with the emission of a photon with energy that is equal to the energy difference between the two initial photons (Figure 2.4 c)).[3]

2.2.1.3. Optical Parametric Generation

Finally, OPG can be envisaged as the reverse of SFG, where instead of two photons being combined within a non-linear medium, a single photon is split into two photons (Figure 2.4 d)). The sum energy of these two photons is equal to the incident photon due to the conservation of energy.[3]

2.2.2 Supercontinuum

Another important non-linear phenomenon exploited within the experimental setup, to generate the probe pulse, is the generation of a supercontinuum. The exact non-linear processes involved in generation of a supercontinuum is still an active area of research.[5-7] The generation of a supercontinuum occurs when the intensity of light passing through a transparent medium reaches some critical threshold. Once surpassed, the incident beam undergoes significant broadening through both Stoke and anti-Stoke shifts,

predominantly the latter. The exact properties of these supercontinua depend heavily on the medium and the incident beam wavelength.

2.3 Probe pulse

The 50 mw beam that the probe pulse is derived from is first sent into a gold plated retroreflector that is mounted upon a translation stage (Physik Instrumente). This allows us to generate the variable time-delay (Δt) between the pump and probe pulses. The stage has a 307 mm travel that allows for a maximum delay of ~2 ns. The retroreflector is employed to make sure the beam pointing is identical at all distances along the position of the stage. After reflecting off the retroreflector, the beam is then sent to the optical setup responsible for the white light supercontinuum generation (Figure 2.5). The first of these optics is a half-wave (λ/2, 800 nm) plate, which is used to alter the polarization of the fundamental beam before white light generation occurs, in turn this sets the polarization of the generated supercontinuum. The need to alter the polarization of the probe is due to anisotropic (rotational) effects. These effects arise due to the use of polarized light, since a molecule will predominantly undergo absorption when its transition dipole moment is aligned with the polarization of the electric field. While the initially excited molecules will be aligned after excitation, they will begin to dephase, leading to a change in the signal and thereby introducing extra dynamics due to rotational motion of the molecular ensemble. This bias in absorption towards molecules of a particular alignment, referred to as the angular distribution ($I(\theta)$) can be modelled by:[8,9]

$$I(\theta) = \frac{\sigma}{4\pi}\left[1 + \beta\frac{1}{2}(3\cos^2\theta - 1)\right] \tag{2.3}$$

where β is the anisotropy parameter,[8] σ is the total cross section and θ is the angle between the molecule's transition dipole moment and the polarization of the electric

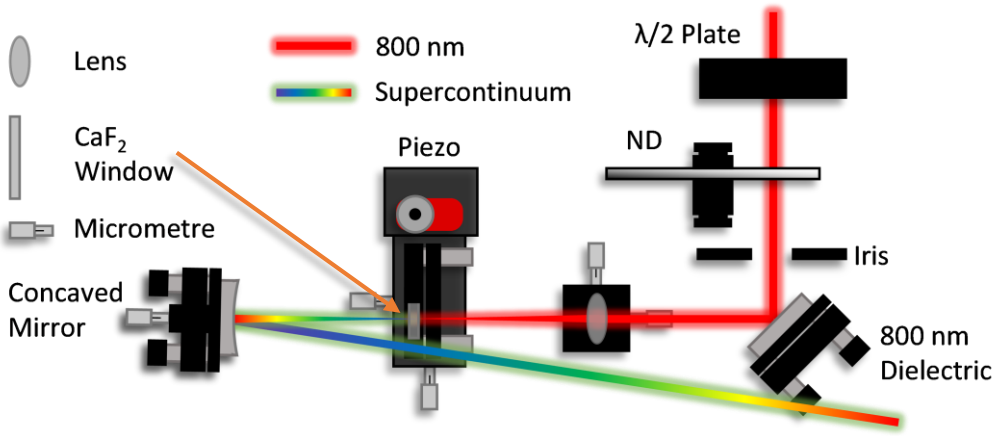

Figure 2.5 Schematic of the supercontinuum generation optical setup. ND = variable neutral density filter.

field. Fortunately these anisotropic effects can be negated by setting the angle between the pump and probe to be 54.7° (magic angle)[10] as this causes the term $3\cos^2\theta - 1$ to equal zero, leading to all orientations of the transition dipole moment being detected equally.

2.3.1 White Light Generation

The supercontinuum is generated by focusing a portion of the fundamental 800 nm beam (50 mW) into a 1 mm thick CaF_2 window. This process requires the photon density to reach a certain threshold for stable white light generation to occur. Therefore, the combination of an iris, variable neutral density (ND) filter and focusing lens are used to control the photon density in the window *via* beam power and tightness of focus. This level of control is needed as if the photon density becomes too great the damage caused to the window is increased (*vide infra*). The window and lens are both mounted on x, y and z translation mounts to allow positioning of the focus within the window, which affects the relative intensity of each wavelength within the supercontinuum as well as the stability of the supercontinuum generated. A drawback of using CaF_2 as the generation medium is that the threshold for supercontinuum generation is greater than the damage threshold of the CaF_2 crystal. This means that the generation of the supercontinuum causes a temporary structural change to the CaF_2 crystal structure to occur, which eventually leads to permanent damage. Fortunately, it takes time for these structural changes in the window to induce instability into the supercontinuum and even longer for permanent damage to occur to the window. Therefore, by translating the window, this prevents damage building up that would lead to instability in the supercontinuum. This translation is achieved by a piezo motor (Newport Corp.) and is in the vertical direction as rotation of the crystal leads to changes in the supercontinuum.[11] The generated supercontinuum is then collimated, before being focussed into the sample. The benefit of using CaF_2 over another medium like water, sapphire or air is the larger anti-Stoke shift that occurs in CaF_2.[7,12] This allows for wavelengths within the near-UV to be produced which can provide a host of dynamical insight into the species of interest (see Chapters 3-5) that would otherwise be undetectable with another generation medium. The range of our detected probe pulse and the relative intensities of the wavelengths are shown in Figure 2.6 but this does not truly show the intensities of the continuum. This is due to the fibre coupled spectrometer detector for the continuum having a wavelength dependant sensitivity, which is biased towards the near-UV. Secondly the mirrors used also have a wavelength specific reflectivity, though

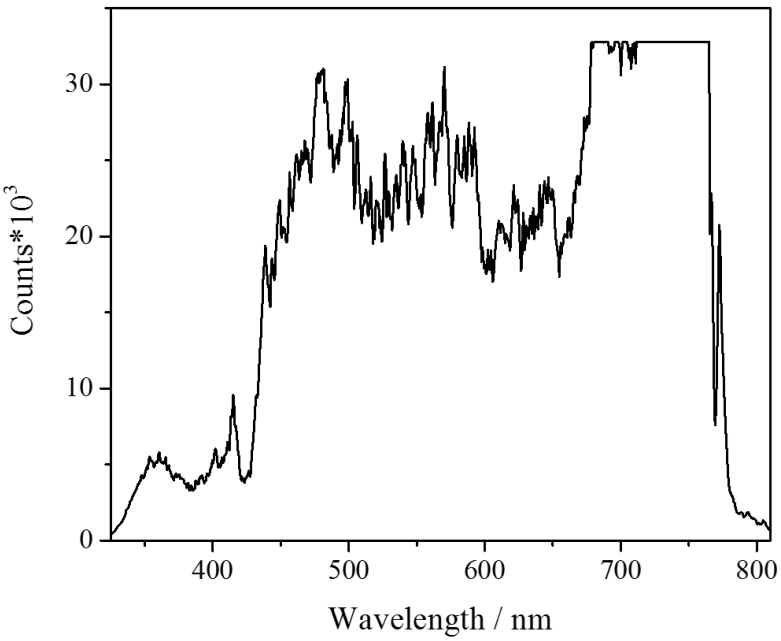

Figure 2.6 A plot showing the relative intensities of the wavelengths within the detected white light supercontinuum. The flat section of the spectrum is due to saturation of the detector at these wavelengths (>675 nm), the filtering of the 800 nm can be seen by the lack of counts in that particular spectral region.

this is minimal and finally the continuum is filtered to remove any residual fundamental; this also slightly reduces the 400 nm section of the continuum.

2.4 Pump-Pulses

The experimental setup has two different methods of producing the pump pulses used within the TEAS measurements. One employs the use of harmonic generation which can be used to pump at the fundamental, and its second and third harmonic; 800, 400 and 267 nm, respectively. The second employs the TOPAS-C and can be used to provide pump wavelengths in the range of ~230-2100 nm, though it is predominately used in the near-UV region for the measurements discussed in this thesis.

2.4.1 Harmonic Generation

The harmonic generation setup (Figure 2.7) is seeded by the fundamental with a beam power of ~945 mW and, depending upon the desired pump wavelength, is constructed from a specific set of optics. For all of the wavelengths generated in this harmonic generation setup, their powers are controlled *via* a variable ND filter before any frequency conversion occurs.[11] When using the fundamental 800 nm as the pump, the optical setup consists of two fixed ND filters (optical density = 2 and 3), and four 800 nm

[11] This is in order to reduce stretching the pulse in time and due to the ND filter being constructed of ground glass which will block the 267 nm.

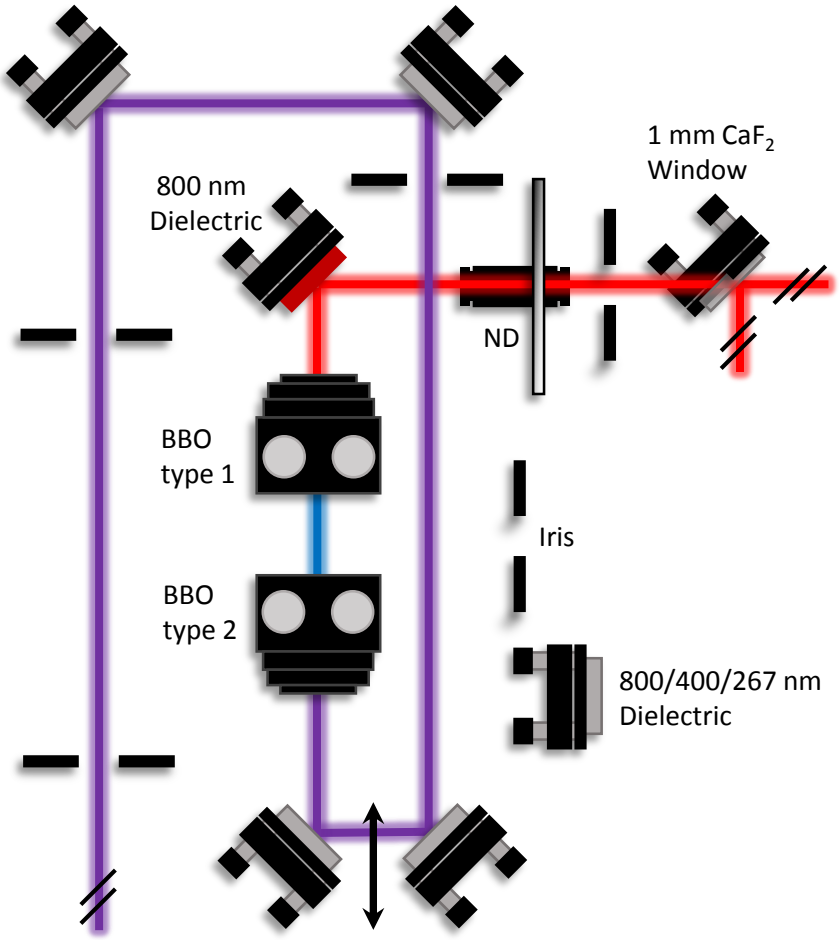

Figure 2.7 Schematic of the optics used within the harmonic generation setup and the splitting off of the reference beam is also shown. (red line) 800 nm, (blue line) 400 nm or 800 nm depending on setup, (purple line) 267 nm or 400 nm or 267 nm depending on the setup. The double headed arrow represents the pair of mirrors that can be moved to match the total path length to equal the probes total path length. The red mirror represents an 800 nm dielectric.

dielectric mirrors. The ND filters are required to reduce the power of the fundamental beam into a useable regime as focussing of the beam into the sample at full power leads to deleterious effects. The first of these is the generation of a white light supercontinuum as described above, yet it occurs in the air, the CaF_2 windows of the sample delivery system (*vide infra*) and the sample itself. Secondly the power of the beam is enough to ablate the surface of the CaF_2 windows and potentially the optics behind the sample depending on the focussing conditions.

When a pump of 400 nm is required, the setup uses a type I β-barium borate (BaB_2O_4, BBO) crystal to convert the fundamental 800 nm *via* SHG. This beam then reflects off four 400 nm dielectrics in order to filter out any residual 800 nm. Finally, for pumping at 267 nm, the setup consists of a type I BBO crystal used for SHG of the fundamental, which is then followed by a type II BBO crystal where SFG occurs between the fundamental 800 nm and the 400 nm second harmonic. After generation of the 267

nm beam, it is filtered by four 267 nm dielectric mirrors in order to remove any residual 800 and 400 nm.

The time-delay between the pump and probe can be increased beyond the limit provided by the length of the translation stage in the probe path. This is achieved by shortening the beam path of the pump pulse, by virtue of a pair of mirrors on a magnetic mount that essentially retroreflects the 800/400/267 nm beam. This mount can be placed on one of five magnetic bases which are spaced 305 mm (2034 ps) apart from each other (Figure 2.1).

2.4.2 TOPAS-C

Since the harmonic generation line is limited to three wavelengths (800/400/267 nm), another beam path is set up using the TOPAS-C. This allows for pumping at a range of wavelengths limited only by what can be produced by the TOPAS-C itself. The production of the various wavelengths involves a combination of second order non-linear processes and supercontinuum generation, however the exact processes involved are wavelength specific. While this line provides a greater selection of wavelengths compared to the harmonic generation, the drawback is inferior beam quality and the limitation of the maximum pump-probe delay to 2 ns. Furthermore, as the beam generated by the TOPAS-C is produced by mixing beams of multiple wavelengths, filtering is required to remove these additional wavelengths. If, however, the filtering is insufficient, the residual wavelengths will travel collinearly with the pump pulse, though in the experiments presented in Chapter 3-5 sufficient filtering was achieved. This could itself cause excitation of the sample or more commonly scatter off the sample into the detector, essentially blinding the detector to that wavelength.

2.4.3 Beam Focus and Chopper

Both of these pump sources share the last mirror before being focussed into the sample (Figure 2.1), which is achieved by passing the beam through a lens that is positioned to focus the beam to between 12 – 20 mm behind the sample. Generally, this gives a beam diameter of 250 μm at the sample which is roughly 2.5 times greater than the probe focus diameter. This is due to the different spectral components of the probe having differing focusing parameters, *i.e.* astigmatism. After focusing, the pump beam is chopped to 500 Hz *via* an optical chopper, in order to alternate between producing probe alone and pump/probe pulse sequences (see Section 1.4.1 and Section 2.7 for further details).

2.4.4 Shutters

The system also employs two mechanical shutters, made from modified hard drives.[13] One of these is placed just before the white light generation for the probe beam and the other just after the chopper for the pump beams. These shutters are designed to reduce irradiation of the sample when the system is not acquiring data. These shutters also allow for automation of background subtraction to remove the dark noise of the detector and any scatter. The scatter can arise from multiple sources, but the main sources in this experimental setup are using a pump pulse within the probe window, or from fluorescence and/or phosphorescence. In the case of scatter from the pump pulse, this can be caused by scattering of the pulse from either the sample or the windows of the sample holder (see below). Some of the scattered light can propagate along the probe path and into the detector. In the case of fluorescence and/or phosphorescence from the sample, the emitted light is produced in all directions allowing for some to enter the optical fibre leading to the detector (*vide infra*). This scattered or emitted light can further be reduced by a polarizer in front of optical fibre if required. Generally, this background subtraction is capable of removing any artefacts in the TAS caused by the scattered or emitted light.

2.5 Sample Delivery

To provide sample to the pump-probe interaction region, a flow through cell is used (Demountable Liquid Cell by Harrick Scientific Products, Inc.). This cell consists of a steel housing for a pair of CaF_2 windows (thickness: 1 mm front, 2 mm back) with a pair of polytetrafluoroethylene (PTFE) spacers to provide the required film thickness (6 μm – 25 mm). As the pump and probe pulses pass through the sample, they undergo group velocity dispersion (GVD, *vide infra*). To reduce the GVD, the thinnest possible sample film is used while providing a usable signal response; the smallest detectable signal is 100 μΔOD. The thinnest spacer that we use within this system is a 100 μm thick spacer. Any thinner spacers (*e.g.* 50 μm) requires a 2 mm front CaF_2 window. In doing so, this provides a greater detriment to the temporal resolution of the pulses (*i.e.* increased GVD) than the reduction in GVD from a thinner film.

2.5.1 Group Velocity Dispersion

GVD occurs due to each wavelength of light having a different refractive index when passing through a medium; this translates to red wavelengths travelling faster than blue wavelengths within the medium. The wavelength (λ) specific refractive index (n) is given by the Sellmeier equation:[14]

$$n^2 = \sum_i 1 + \frac{A_i \lambda^2}{\lambda^2 - B_i} \tag{2.4}$$

Here A and B are the Sellmeier coefficients, the value of these and the value of i are unique to each transparent material.

The effect of GVD can be either beneficial or detrimental to the temporal resolution of the experiment. GVD can be used beneficially to compress the pulses in time and this can be achieved by simply sending the longer wavelengths along a longer path length than the short wavelengths *e.g.* through a prism. This allows for the shorter wavelengths to "catch up" to the longer wavelengths. Generally, all the wavelengths in our white light supercontinuum probe travel along the same path, which leads to the shorter wavelengths trailing behind the longer wavelengths and thus temporally stretching the probe pulse; the spread of the wavelengths within the pulse is referred to as chirp. An example of the chirp is shown in Figure 2.8 and shows the relative time difference between each wavelength. However, the probe is not the only pulse that is affected by GVD, the pump pulse is also an ensemble of wavelengths, though less spectrally broad compared to the probe. Therefore, the temporal resolution of the system is dependent on both pulses, yet it is predominately determined by the pump pulse. This is because while the probe pulse's wavelengths are spread out, each individual wavelength is only spread out over a small section of the pulse and each wavelength is detected separately.

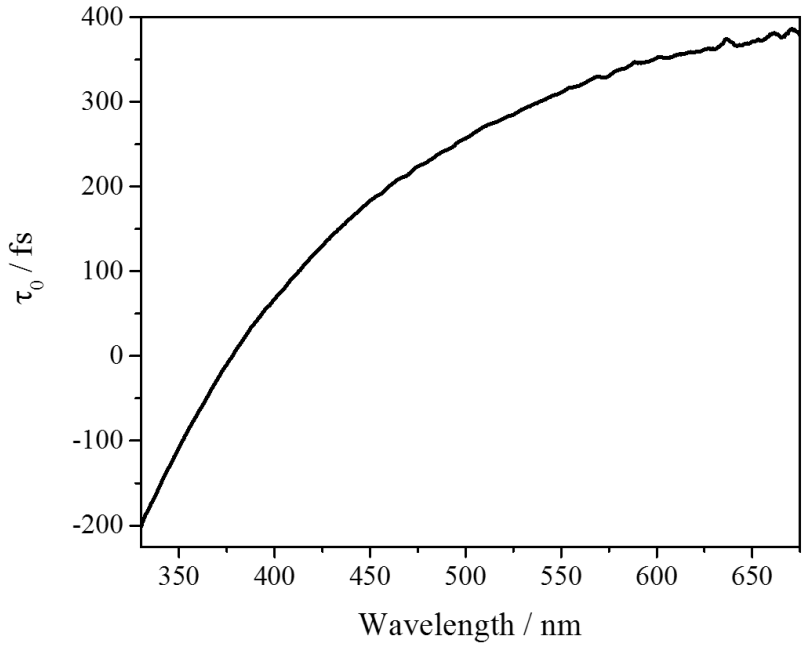

Figure 2.8 A plot showing the maximum intensity at each wavelength of the cross-correlation between the pump and probe pulses. This plot serves to highlight the relative temporal spread of the wavelengths in the supercontinuum.

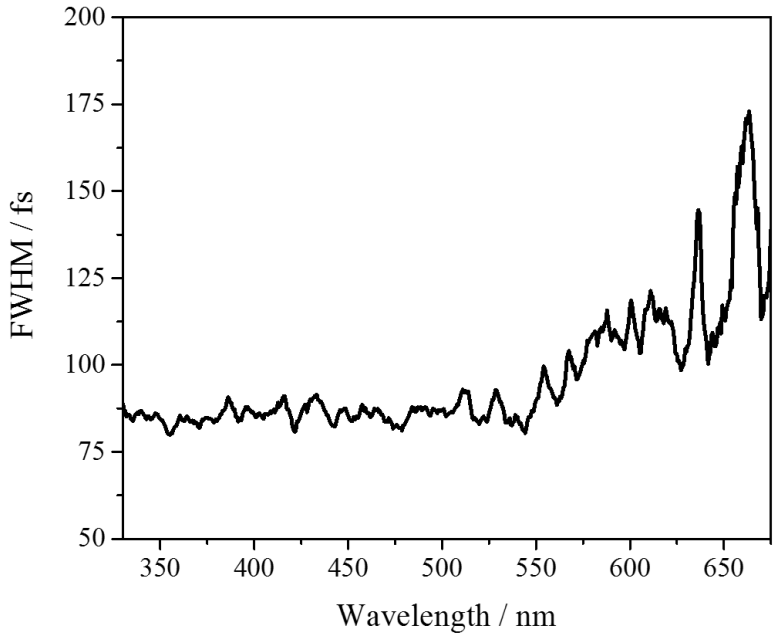

Figure 2.9 A plot showing the FWHM of the Gaussian response from the cross-correlation between the pump and probe.

Yet in the case of the pump, each wavelength can potentially excite the molecule, thus the total pulse duration effects the temporal resolution.

The temporal resolution of the experiment can be determined experimentally by taking a cross-correlation of the pump and probe pulses at each of the probe wavelengths, which generally appears as a Gaussian response[12] when plotting ΔOD versus time, and extracting the full width half maximum (FWHM) of the Gaussian.[15] Figure 2.9 shows the results of fitting the Gaussian response at each wavelength within the supercontinuum probe. As can be seen there is a loss of temporal resolution at redder wavelengths, which is related to the relationship between the uncertainty in time and energy (Section 1.2.4).[15]

2.5.2 Sample

The sample is drawn to the cell from a custom made glass reservoir, shown in Figure 2.10 c), capable of holding 25 - 50 ml of sample, *via* a peristaltic pump (Masterflex) using PTFE tubing. This is designed to make sure fresh sample is provided for each laser pulse and also that any photoproducts produced are diluted to negligible quantities. A minimum flow speed is also required in order to provide the pump-probe interaction region with fresh sample each pulse. This flow speed is given by:

[12] While normally a Gaussian response is observed, it can be convoluted with other contributions, generated through several other phenomena such as sample dynamics, multi-photon effects, solvent and window dynamics, and Raman signals.

$$Flow\ Speed = \frac{\frac{Pump\ Beam}{Diameter}}{Time\ Between\ Laser\ Pulses} Sample\ Thickness \quad (2.5)$$

Normally the pump FWHM intensity diameter is 250 μm and the laser repetition rate gives a time-delay of 1 ms between each pulse, hence if a 100 μm sample thickness is used a minimum flow speed of 6.25×10^{-6} Ls^{-1} is required. If the flow speed of the sample is slower than this, an increase in probe noise occurs. This noise also increases when the flow speed is too high as turbulence begins to affect the flow, so the flow speed is set optimally.

The sample delivery system has also been designed to be utilized under vacuum and to be filled with dry, inert gases. The system can be used with either dry N_2 or dry Ar, allowing air and water sensitive analytes to be studied; these gases are dried *in situ via* a drying tube that is shown in Figure 2.10 b) which is between the gas supply and the Schlenk line. The vacuum and the dry inert gas are provided to the system by a Schlenk line which is shown in Figure 2.10 a), the top tube in this setup supplies the dry inert gas, while the bottom tube is under vacuum. This Schlenk line is linked to the glass reservoir, shown in Figure 2.10 c), through the use of taps that can link to either the vacuum tube or dry inert gas tube. Furthermore, the reservoir is also designed to allow the sample to be introduced under a dry inert gas by cannula transfer.

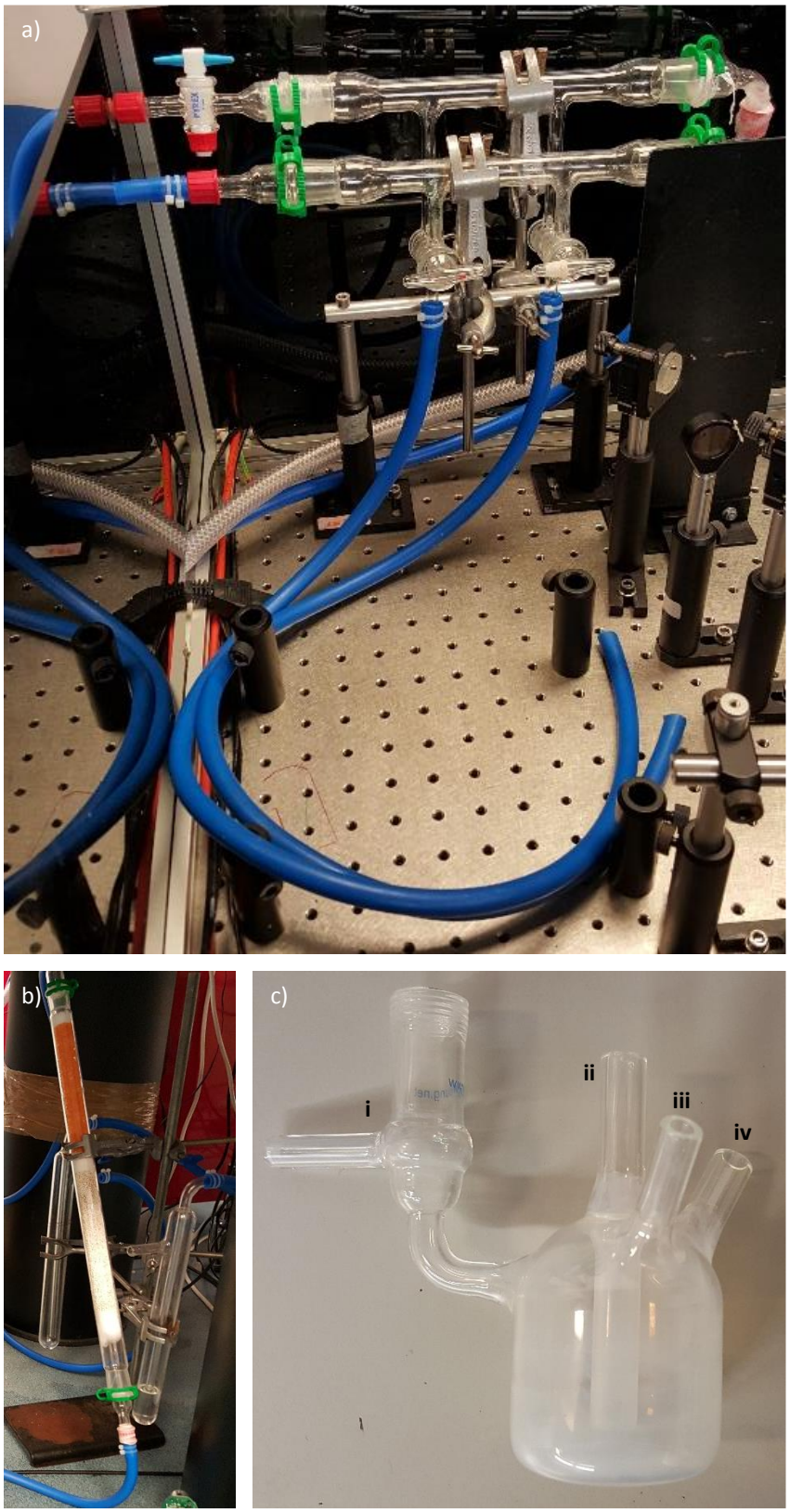

Figure 2.10 Images of the Schlenk lines (a)), drying tube (b)) and the sample reservoir (c)). The Schlenk line consists of two tubes, the top tube contains the dry inert gas used to keep the sample under dry inert atmosphere, while the bottom tube is under vacuum allowing for the system to be purged of air and moisture. The taps allow selective control over which tube the sample system is connected to at a given time. The sample reservoir consists of four tubes: **i** which connects the reservoir to the Schlenk line using the blue tubes connected to the taps, **ii** connects to the flow cell and is the outlet, **iii** is the tube which allows for the sample to be introduced *via* cannula transfer and **iv** is the sample return from the flow cell.

2.6 Detection

After the pump and probe pass through the sample, the residual pump beam is blocked with an iris in order to minimise any scatter into the detector. The probe on the other hand passes through the aperture of this iris, which is in front of a 0° 800 nm dielectric mirror. This mirror is used as a filter, as any residual 800 nm that is not converted during supercontinuum generation is capable of damaging the optics within the detector (spectrometer). The probe is then collimated and passes through a variable ND filter, as the intensity of the supercontinuum at certain wavelengths is able to saturate the detector. Finally, the probe is focussed into an optical fibre, which then feeds into the spectrometer (Avantes). This spectrometer has an acquisition rate of 1 kHz allowing for collection of every probe pulse, though due to hardware limitations only 2500 pulses can be acquired before needing to be read out and stored. As mentioned previously, part of the 800 nm fundamental (used for harmonic generation) is split off to create a reference beam, which passes through the optical chopper and sent into the optical fibre as well. This reference beam is used to determine whether the spectrometer started to collect data on a pumped or an unpumped pulse sequence (given it passes through the optical chopper along with the pump pulse, it only shows up in every other shot). This also bypasses the 0° 800 nm dielectric so it is the only source of 800 nm on the spectrometer making it a suitable reference source.

2.7 System Control

To programmatically control the various components of the experimental setup with a computer, a custom made LabVIEW virtual instrument (VI) is used and fully automates the data acquisition. The VI also converts the acquired probe spectra into the corresponding TAS in ΔOD. This is achieved by implementing the following formula:

$$\Delta\mathrm{OD}(t,\lambda) = log\frac{I_0(\lambda) - I'(\lambda)}{I^*(t,\lambda) - I''(\lambda)} \tag{2.6}$$

where I_0 is the intensity of the probe passing through an unpumped sample, I^* is the probe intensity passing through a pumped sample, I' is the background arising due to the dark charge[13] and ambient lighting and I'' is the background due to any pump only effects. Both I' and I'' are collected automatically *via* the use of the automated shutters. I' is acquired from the spectrometer when both the pump and probe beams are blocked and I'' is recovered from the spectrometer with only the probe blocked. No further post-processing is performed on the data by the VI.

[13] An intrinsic response from the charge-coupled device chip due to electrical noise.

2.8 Analysis

To recover the dynamical information contained within the TAS, a few options are available for use and which method used is dependent upon the data collected and information desired.

2.8.1 Single Wavelength Transients

A transient slice is produced by integrating a range of 5 nm centred on a specific wavelength and then plotted against Δt. This can then be fit ($F(\Delta t)$) using the required number of exponential decays or rises, each convoluted ($*$) with a Gaussian function ($g(\Delta t)$) to model the instrument response (Section 2.5.1) thus:[16]

$$F(\Delta t) = \sum_{i=1}^{n} \left[g(\Delta t) * A_i exp\left(\frac{-\Delta t}{\tau_i}\right)\right] \quad (2.7)$$

where *n* is the number of exponentials, A_i is the amplitude of the exponential (a positive amplitude represents a decay while a negative indicates a rise) and the time constant of the decay is given by τ_i. The fits are performed in the Origin software package which uses the Levenberg-Marquardt algorithm.[17,18] This fitting method is used in Chapter 3 for the TR-IY, TR-VMI and TEAS measurements. It is also employed in Chapter 5 to fit the kinetic traces received from the KOALA spectral decomposition (*vide infra*).

2.8.2 Global Fitting

Instead of fitting just a single wavelength slice, it is possible to fit across the entire probe window simultaneously to model any dynamics observed. This is often referred to as a global fit. However, rather than just treating each wavelength individually with Equation (2.7), it is used for all wavelengths at once, the τ_i value for the fit is produced that best represents every wavelength, while the value of A_i is varied for each wavelength.[19,20] A plot of the values of A_i for each individual τ_i versus wavelength is referred to as a decay associated spectrum (DAS). This can be useful in showing which processes that drive the spectral evolution of the TAS are linked *i.e.* an excited state absorption that is linked with a stimulated emission (see Chapter 4 as an example). As such this approach is particularly useful if various spectral features overlap.

The error analysis performed on the global fit is asymptotic standard error.[21] This involves varying the value of τ_i systematically while fixing the other parameters of the fit, at each value the chi squared (χ^2) is retrieved. The lowest value of χ^2 is referred to as the global minimum (χ^2_{min}) where a ratio between the values of χ^2 at each value of τ_i and χ^2_{min} is taken:

$$\chi^2(\tau_i)/\chi^2_{min} \tag{2.8}$$

This ratio is then compared to:

$$1 + \frac{p}{f}F(N, p, f) \tag{2.9}$$

Here F is the inverse cumulative distribution function, p is the number of parameters within the fit, f is the degrees of freedom and N is the confidence interval. The largest deviation of τ_i that satisfies:

$$\chi^2(\tau_i)/\chi^2_{min} \leq 1 + \frac{p}{f}F(N, p, f) \tag{2.10}$$

is defined as the as the upper error bound of the fit. The confidence interval that is used within error analysis of our global fit values is 95%.

2.8.3 KOALA

A drawback of using the global fitting procedure described above, is the probe wavelengths have to have the same time-zero (t_0). t_0 is the point in time when the pump and probe pulse arrive at the sample at the same point in time. However, due to GVD (see Section 2.5.1), the various spectral components of the probe (see Figure 2.6) arrive at the sample at different times. Therefore each wavelength possess its own t_0. This can be corrected however through chirp correction, which shifts each individual t_0 so that they occur at the same time-delay. The chirp correction of our TAS is done *via* the KOALA (Kinetics Observed After Light Absorption) software package developed by Dr Michael Grubb at the University of Bristol.[22] KOALA is also capable of performing kinetic analysis of the TAS.

2.8.3.1. Chirp Correction

The chirp correction in the KOALA software package is achieved by first designating t_0 for each wavelength. This is then plotted *versus* wavelength before being fit with the following:[22]

$$t_0(\lambda) = AP + GVD\left(\frac{2\pi c}{\lambda}\right) + \frac{1}{2}TOD\left(\frac{2\pi c}{\lambda}\right)^2 \tag{2.11}$$

where AP is the absolute phase and TOD is the third order dispersion. This fit is then applied to each value of $\Delta\mathrm{OD}(t)$ thereby providing each wavelength its own time-delay. However, giving each wavelength its own time-delay is impractical as it introduces another level of complexity into the fitting procedure, so instead the $\Delta\mathrm{OD}(\lambda)$ are linearly interpolated to produce values at the original time-delays.[22] To increase the accuracy of

this interpolation, a large number of TAS are taken with a small step size (10 fs) in the first ps of our measurements.

2.8.3.2. Kinetic Analysis

KOALA is also capable of performing spectral decomposition of the TAS data *via* a linear least squares regression with a series of spectral basis sets. These basis sets represent the absorption of a particular species $[S]$ within the TAS *e.g.* a radical absorption, and by giving KOALA a basis set for each absorbing species, it can model the contribution from each species to the overall TAS. The spectral decomposition is provided by:[22]

$$[\Delta \mathrm{OD}]_\lambda = [S]_{n,\lambda}[I]_n + [\epsilon]_\lambda \tag{2.12}$$

where n is the number of spectral species, $[I]$ is a weighting factor that is proportional to the concentration of the species $[S]$ and $[\epsilon]$ is the residual signal not successfully modelled. Thus the best fit from this spectral decomposition occurs when $[\epsilon]$ is at a minimum, allowing for Equation (2.12) to be rearranged to provide values of $[I]$:[22]

$$[I]_n = \left([S]_{n,\lambda}{}^T[S]_{n,\lambda}\right)^{-1}[S]_{n,\lambda}{}^T[\Delta OD]_\lambda \tag{2.13}$$

By plotting the values of $[I]_n$ against time-delay, a kinetic trace can be acquired, which then can be fit in the same manner as a single wavelength transient to retrieve the dynamical information contained in the traces.

2.9 Bibliography

1. P. F. Moulton, *J. Opt. Soc. Am. B*, 1986, **3**, 125-133.
2. J.-C. Diels and W. Rudolph, *Ultrashort Laser Pulse Phenomena*, Academic press, United States of America, Second edn., 2006.
3. R. W. Boyd, *Nonlinear Optics*, Academic Press, United States of America, Third edn., 2008.
4. R. Eckardt and J. Reintjes, *IEEE J. Quant. Electron.*, 1984, **20**, 1178-1187.
5. A. L. Gaeta, *Phys. Rev. Lett.*, 2000, **84**, 3582-3585.
6. A. M. Zheltikov, *Phys. Usp.*, 2006, **49**, 605-628.
7. A. Brodeur and S. L. Chin, *J. Opt. Soc. Am. B*, 1999, **16**, 637-650.
8. B. J. Whitaker, *Imaging in Molecular Dynamics: Technology and Applications*, Cambridge University Press, United States of America, 2003.
9. K. L. Reid, *Annu. Rev. Phys. Chem.*, 2003, **54**, 397-424.
10. J. R. Lakowicz, *Principles of Fluorescence Spectroscopy*, Springer, United States of America, Third edn., 2006.

11. P. J. M. Johnson, V. I. Prokhorenko and R. J. Dwayne Miller, *Opt. Express*, 2009, **17**, 21488-21496.
12. C. Nagura, A. Suda, H. Kawano, M. Obara and K. Midorikawa, *Appl. Opt.*, 2002, **41**, 3735-3742.
13. L. Maguire, S. Szilagyi and R. Scholten, *Rev. Sci. Instrum.*, 2004, **75**, 3077.
14. W. Sellmeier, *Ann. Phys.*, 1871, **219**, 272-282.
15. M. Ziólek, M. Lorenc and R. Naskrecki, *Appl. Phys. B*, 2001, **72**, 843-847.
16. D. Hanggi and P. W. Carr, *Anal. Chem.*, 1985, **57**, 2394-2395.
17. K. Levenberg, *Q. Appl. Math.*, 1944, **2**, 164-168.
18. D. W. Marquardt, *J. Soc. Indust. Appl. Math.*, 1963, **11**, 431-441.
19. C. R. Mooney, D. A. Horke, A. S. Chatterley, A. Simperler, H. H. Fielding and J. R. Verlet, *Chem. Sci.*, 2013, **4**, 921-927.
20. S. Ullrich, T. Schultz, M. Z. Zgierski and A. Stolow, *Phys. Chem. Chem. Phys.*, 2004, **6**, 2796-2801.
21. L. A. Baker, M. D. Horbury, S. E. Greenough, F. Allais, P. S. Walsh, S. Habershon and V. G. Stavros, *J. Phys. Chem. Lett.*, 2016, **7**, 56-61.
22. M. P. Grubb, A. J. Orr-Ewing and M. N. R. Ashfold, *Rev. Sci. Instrum.*, 2014, **85**, 064104.

3. Environment Specific Photochemistry of 4-*tert*-Butylcatechol

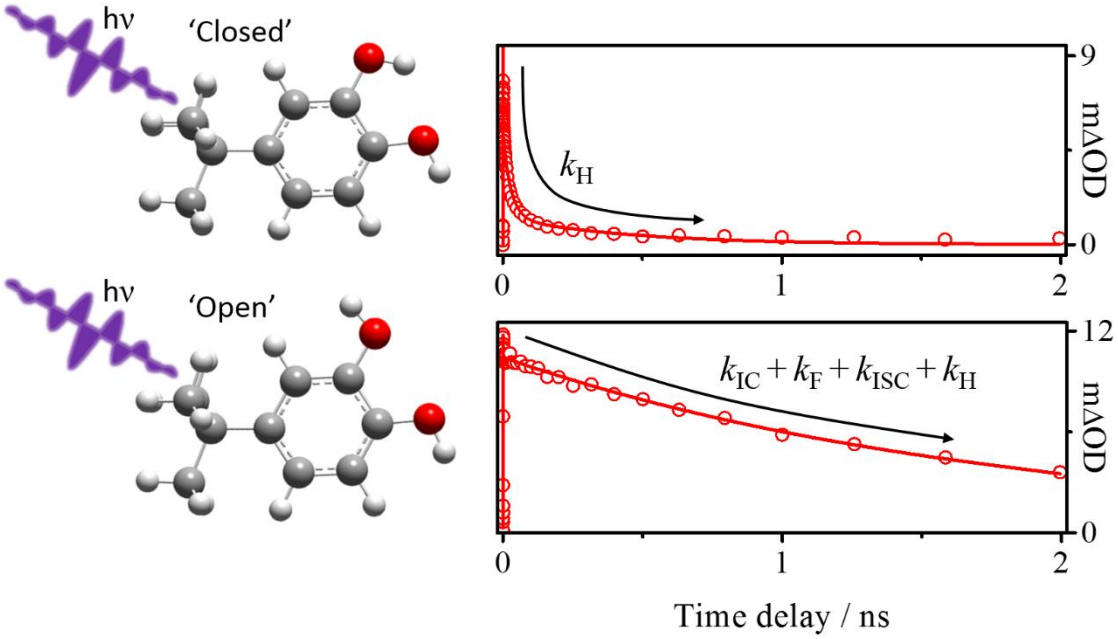

This chapter is based on the following publication:

> M. D. Horbury, L. A. Baker, W.-D. Quan, J. D. Young, M. Staniforth, S. E. Greenough, and V. G. Stavros, Bridging the Gap between the Gas and Solution Phase: Solvent Specific Photochemistry in 4-*tert*-Butylcatechol, *J. Phys. Chem. A.*, 2015, **119**, 11989-11996

The Time-Resolved Ion Yield and Time-Resolved Velocity Map Imagining data presented in Section 3.3.1 was collected by M. Staniforth and J. D. Young.

The deuteration of 4-*tert*-Butylcatechol, drying of acetonitrile and cyclohexane and the NMR spectra were carried out by W.-D. Quan

The theory calculation used in Figures 3.1, 3.8 and 3.13 were performed by M. Staniforth.

3.1 Introduction

In this chapter we explore the effects of solvation on the intrinsic photodynamics of 4-*tert*-butylcatechol (termed 4-TBC hereon), that have been determined *via* complementary gas-phase measurements. As previously discussed in Chapter 1, employing a bottom-up approach, in which the UV chromophore motif (or subunit itself) of a larger biomolecule is isolated and studied,[1,2] can lend valuable insights from which we may begin to understand the photochemistry of the larger biomolecule as a whole. One of these UV chromophores is catechol (1,2-dihydroxybenzene), a motif in a range of biomolecules, most notably eumelanin. As one of three types of melanin,[3] eumelanin is largely responsible for skin's frontline defence against UV exposure.[4,5] However, gaining a complete understanding of its photodynamics is ongoing, with much progress to be made,[6-9] evidenced by recent work implicating the long-term (after many hours of UVA exposure) phototoxicity of eumelanins.[10] Previous gas-phase studies of catechol[11] have shown that, after excitation to the first excited $^1\pi\pi^*$ state (S_1), H atom elimination is observed from dissociation of the non-intramolecular hydrogen bonded "free" O–H bond, leading to the formation of the catechoxyl radical in approximately 10 ps. Immediately, this suggests that catechol is not photostable following UV exposure, and yet it is a motif of a photoprotective biomolecule.[7] In nature, eumelanin resides within organelles as large heteropolymer fibrils;[12] thus gas-phase studies are unable to fully capture the photodynamics of catechol in its native environment. Therefore, we ask, do the natural surroundings of catechol influence its photodynamics? In this chapter, we try to address this question. Owing to catechol's poor solubility in nonpolar solvents, the functionalized catechol, 4-TBC, is used instead, shown in Figure 3.1. In order to gauge how well 4-TBC performs as a proxy for catechol, we performed time-resolved velocity mapped imaging (TR-VMI) and time-resolved ion yield (TR-IY) measurements in the gas-phase and compared these too previous measurements using these techniques on catechol. To model the role that the surrounding solvent plays in the excited state dynamics of 4-TBC after excitation to the S_1 state, we employ femtosecond transient electronic (UV/visible) absorption spectroscopy (TEAS), using the weakly perturbing, nonpolar solvent cyclohexane, and the highly perturbing, polar solvent acetonitrile.

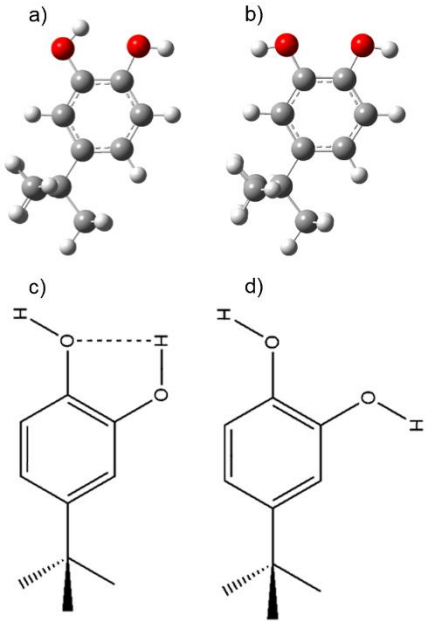

Figure 3.1 'Gas-phase' calculations of the first a) and second b) lowest energy conformers ('closed' and 'open' respectively) in the ground electronic (S_0) state of 4-TBC; the open conformer is 1662 cm^{-1} (0.21 eV) higher in energy. Molecular geometries calculated in Gaussian09 using the M052X functional with a 6-311G** basis set. The corresponding structural drawings are also shown, c) the closed conformer and shows the intramolecular hydrogen bond (dash bond) and d) shows the open conformer.

3.2 Methods

3.2.1 Experimental Methodology

The generation of the laser pulses used within these experiments are described in detail in Chapter 2, alongside a detailed explanation of the TEAS setup. The nuances for the TEAS experiment are as follows: the $h\nu_{pu}$ is centred at 267 nm with a fluence of 1–2 mJ cm^{-2} and the $h\nu_{pr}$ spans 330–675 nm. The 4-TBC (≥98%, Sigma-Aldrich) is dissolved in either cyclohexane (100%, VWR) or acetonitrile (99.9%, VWR) at a concentration of 35 mM. The spacer size used in the sample holder (See Section 2.5) was 100 μm.

Static UV/visible spectra of 4-TBC in the vapour-phase, cyclohexane and acetonitrile were taken using a Cary 50 spectrometer. These spectra are shown in Figure 3.2.

The detailed experimental procedures pertaining to TR-VMI and TR-IY, have been extensively described elsewhere.[13] For TR-VMI and TR-IY a pump pulse ($h\nu_{pu}$) centred at 267 nm (~6 μJ/pulse) and a probe pulse ($h\nu_{pr}$) set to 243 nm (~7 μJ/pulse) are used with a maximum temporal delay of 1.2 ns.

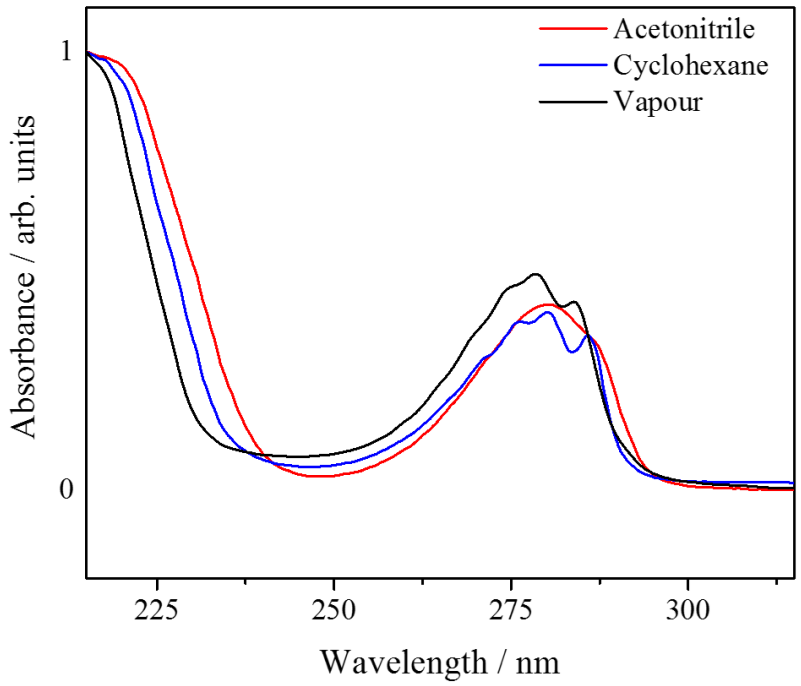

Figure 3.2 UV-Vis of 4-TBC in the vapour (black line), cyclohexane (blue line) and acetonitrile (red line).

3.2.2 Deuteration and Characterization

Comparative TR-VMI, TR-IY and TEAS studies were also carried out on the deuterated isotopologue of 4-TBC, *i.e.*, 4-TBC-d_2, in which we have selectively deuterated both O–H bonds ($C_{10}H_{12}O_2D_2$), synthesized and characterized according to the following

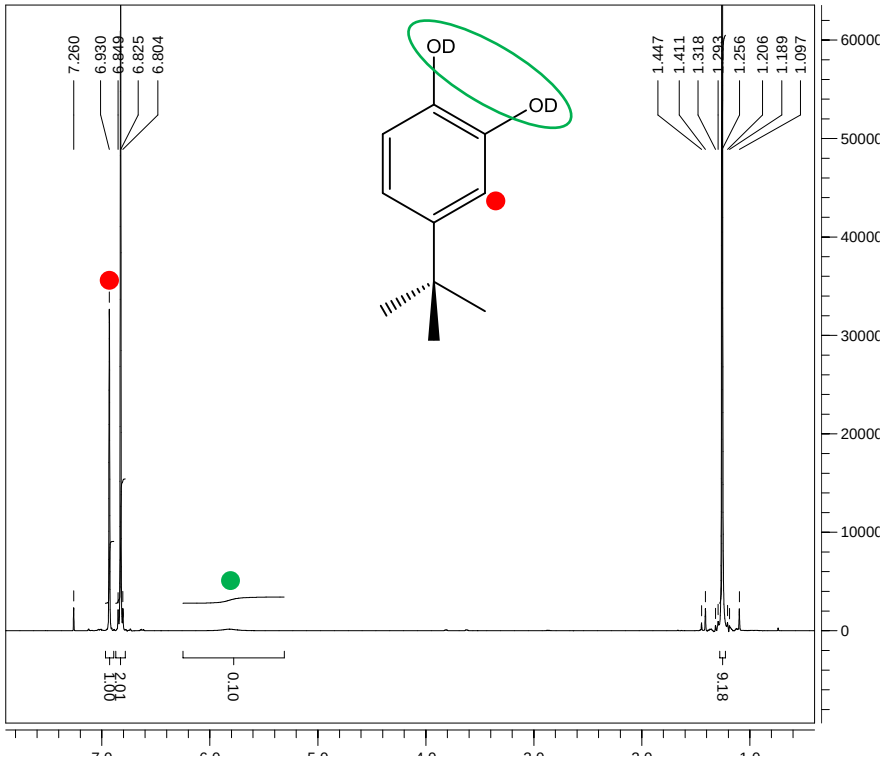

Figure 3.3 ^{1}H NMR spectrum of 4-TBC-d_2 (400 MHz, $CDCl_3$), the alcohol hydrogen peak is absent due to deuteration.

procedure. 1 g of 4-*tert*-butylcatechol (4-TBC) was added to an oven-dried 50 ml round bottom flask, which was then evacuated and back filled with dry N_2 three times before adding 20 ml of D_2O. The solution was stirred under dry N_2 for 18 hrs. D_2O was then removed by lipholysation (freeze-drying). This process was repeated twice and the yield was assumed to be quantitative. The hydroxyl proton peak in the NMR spectrum of 4-TBC (5.44-5.79 ppm, 2H) (Figure 3.3) was reduced by 95% as shown Figure 3.4.

Cyclohexane and acetonitrile, used for the deuterated sample scans, were freshly distilled over CaH_2 under dry N_2, collecting only the middle 80% of the distillate to ensure minimum atmospheric water contamination. Distillations were all carried out immediately prior to sample preparation.

An appropriate amount of the 4-TBC-d_2 was weighed and placed in an oven-dried ampule, which was evacuated and backfilled with dry N_2. 5 ml of deuterated methanol (MeOD-d_4) was then added to the ampule and stirred overnight. MeOD-d_4 was then removed under high vacuum at room temperature immediately prior to scans. The anhydrous solvents were then cannula transferred into the ampule under dry N_2 to give a sample volume of 50 ml and a 4-TBC-d_2 concentration of 35 mM for cyclohexane and 30 mM for acetonitrile; this lower concentration was due to the amount of 4-TBC-d_2 available. The prepared samples were once again cannula transferred into the airtight

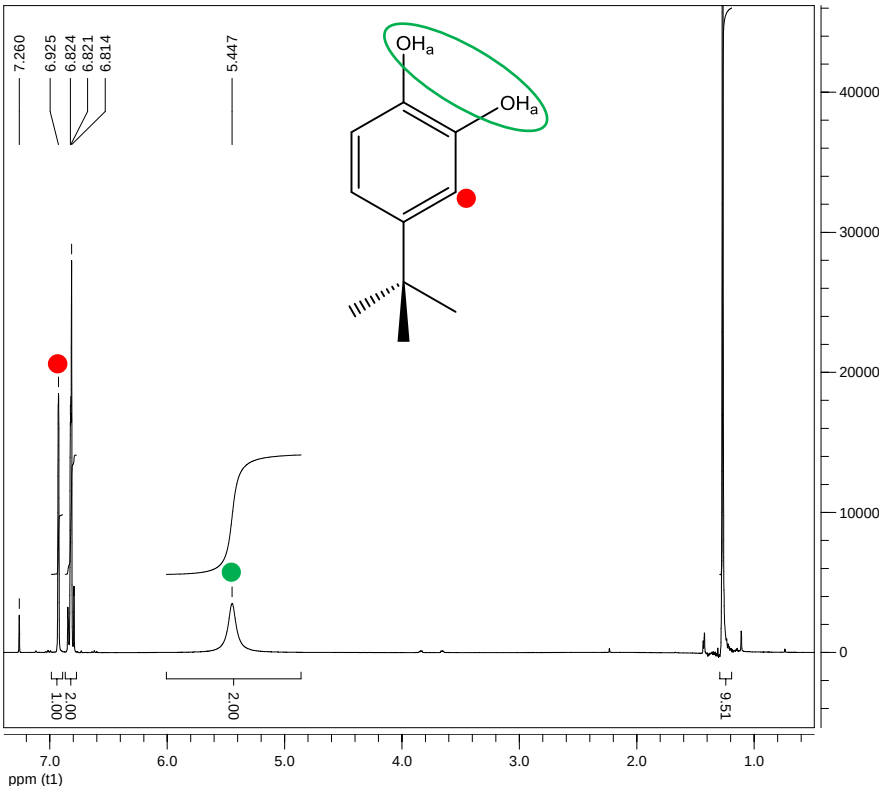

Figure 3.4 ^1H NMR spectrum of 4-TBC (400 MHz, $CDCl_3$), the green label denotes the alcohol hydrogen peak.

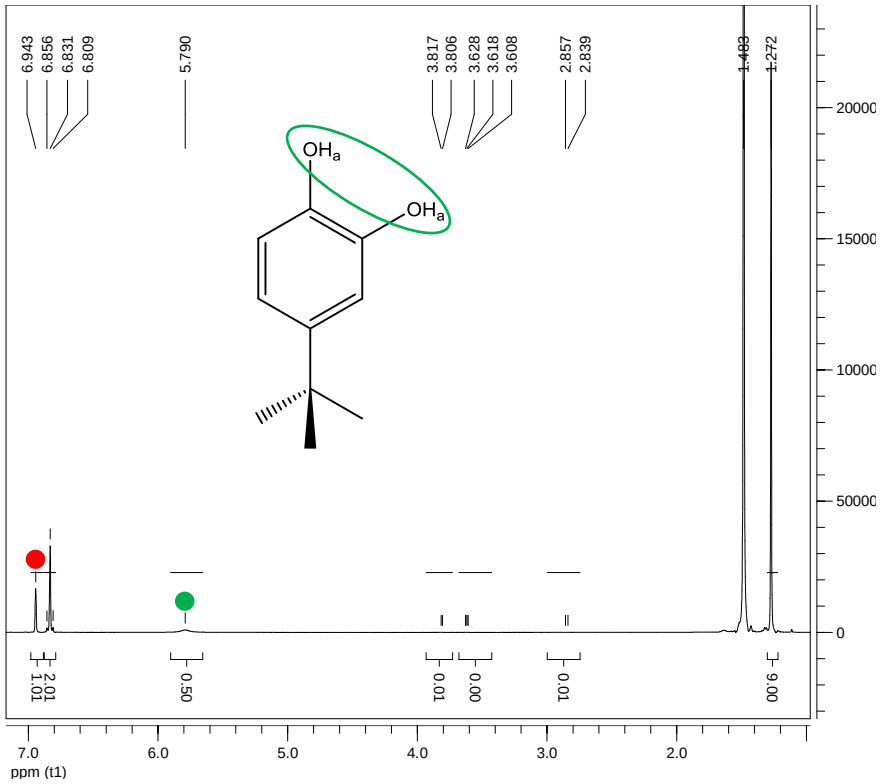

Figure 3.5 ^{1}H NMR spectrum of 4-TBC-d_2 (400 MHz, $CDCl_3$) after TAS scans. The alcohol hydrogen peak labelled green is now present, indicating some protonation of the deuterated sample.

flow set up that had been pre-evacuated and backfilled with dry N_2. A positive pressure was applied to the sample from the dry N_2 line for the duration of the TEAS scans to prevent H_2O in the atmosphere from leaking into the flow cell line. NMR was performed on recovered samples after scans, indicating only 20% of the sample was protonated by the end of TAS scans, see Figure 3.5.

3.2.3 Fitting Procedure

3.2.3.1. Solution-Phase

The fits $F(\Delta t)$ used for the solution-phase transient slices within this chapter are based on the single wavelength transient procedure described detail in Section 2.8.1 (Equation 2.7) though for ease the equation is repeated here:

$$F(\Delta t) = \sum_{i=1}^{n} \left[g(\Delta t) * A_i exp\left(\frac{-\Delta t}{\tau_i}\right) \right] \qquad (3.1)$$

The fit is convoluted ($*$) with a Gaussian function $g(\Delta t)$, τ_i is the time constant and A_i is the amplitude of the exponential. The number of exponentials (n) used for the fits varied depending on the trace fit. The number of exponential decay functions used for the neat cyclohexane solvent response was n = 3 as this was required to accurately fit the resulting transient. Both the 4-TBC and 4-TBC-d_2 in cyclohexane transients were fitted using n = 4 (tetra) exponential decay functions where the first three exponentials were

locked to those obtained in the neat cyclohexane solvent response fitting. Finally, 4-TBC and 4-TBC-d_2 in acetonitrile only required two exponential decay functions to fit the transients as negligible solvent response is observed.

3.2.3.2. Gas-Phase

All transients obtained from TR-IY and TR-VMI were modelled using slightly altered exponential decay functions compared to the solution-phase function; again these are convoluted ($*$) with a Gaussian instrument response function, $g(\Delta t)$. All 4-TBC$^+$ and 4-TBC-d_2^+ were fitted using a bi-exponential function $P(\Delta t)$:

$$H(\Delta t) = \left[g(\Delta t) * \left(Aexp\left(\frac{-\Delta t}{\tau_1}\right)\right)\right] + \left[g(\Delta t) * \left(Bexp\left(\frac{-\Delta t}{\tau_2}\right)\right)\right] \qquad (3.2)$$

and H^+ and D^+ transients were fitted using a bi-exponential function $H(\Delta t)$:

$$P(\Delta t) = \left[g(\Delta t) * \left(1 - Aexp\left(\frac{-\Delta t}{\tau_1}\right)\right)\right] + \left[g(\Delta t) * \left(1 - Bexp\left(\frac{-\Delta t}{\tau_2}\right)\right)\right] \qquad (3.3)$$

We note that we use τ_1 and τ_2 here for the rise/decay time constants for simplicity. In the main text, these are specifically labelled according to each individual dynamical process being probed.

3.3 Results and Discussion

3.3.1 Gas-Phase Studies

Figure 3.6a shows an example total kinetic energy release (TKER) spectrum with the image from which it was extracted shown inset; the left half corresponds to the recorded H^+ image while the right half shows the reconstructed slice through the centre of the 3-D ion distribution; the black arrow indicates the electric field polarization, $\boldsymbol{\varepsilon}$, of the pump pulse. A pump wavelength of 267 nm (4.64 eV) was used to photoexcite 4-TBC to the S_1 state, with any generated H-atoms subsequently ionized via a [2+1] resonance enhanced multiphoton ionization (REMPI) scheme using the $h\nu_{pr}$ wavelength of 243 nm. The pump−probe time delay (Δt) used when recording this particular image was set at Δt = 1.2 ns. A high kinetic energy (KE) feature is apparent in the TKER spectrum centred at ~7,500 cm^{-1}, which returns to the baseline by ~10,000 cm^{-1}. This high-KE signature strongly agrees with previous work by the group in catechol,[11] and is associated with H atoms generated through dissociation of the "free" (non-hydrogen bonded) O−H bond (see Figure 3.6a). Alongside the H-atoms produced, the dissociation also yields 4-tert-butylcatecoxyl radical species, $C_{10}H_{13}O_2$(X) (termed 4-TBC$^\bullet$, or 4-TBC-$d_1^\bullet$ for the deuterated isotopologue, hereon). This dissociation occurs along the $^1\pi\sigma^*$ surface (S_2),

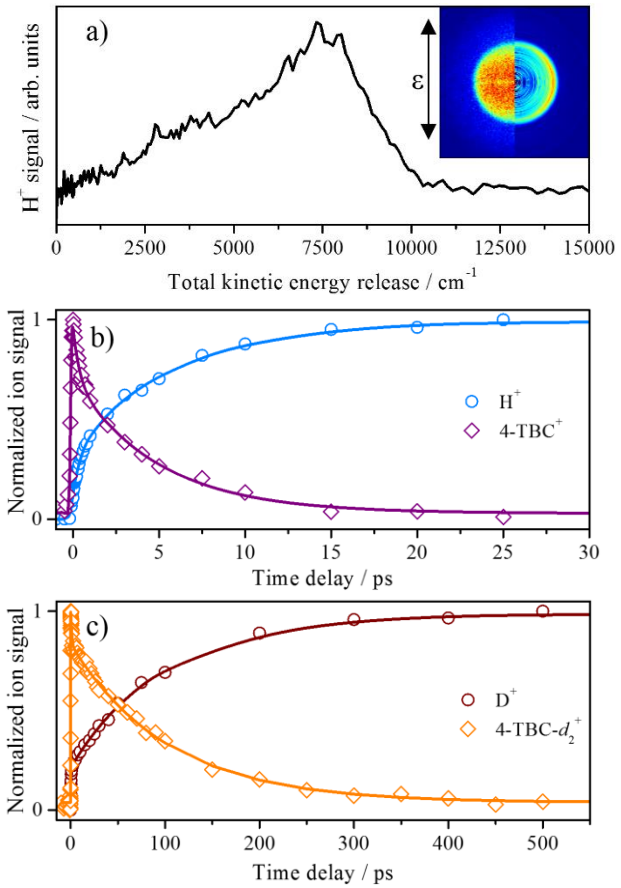

Figure 3.6 a) TKER spectrum of 4-TBC following excitation at 267 nm and probing H-atom photoproducts with a 243 nm probe pulse at Δt = 1.2 ns. Inset: H^+ velocity map image, left half showing raw image, right half showing reconstructed image. b) Normalized integrated H^+ signal transient (blue circles) and the corresponding parent ion signal transient (purple diamonds), solid lines show the kinetic fits. c) Normalized integrated D^+ signal transient (dark brown circles) and the corresponding parent (4-TBC-d_2^+) ion signal transient (light brown diamonds). Solid lines show kinetic fits.

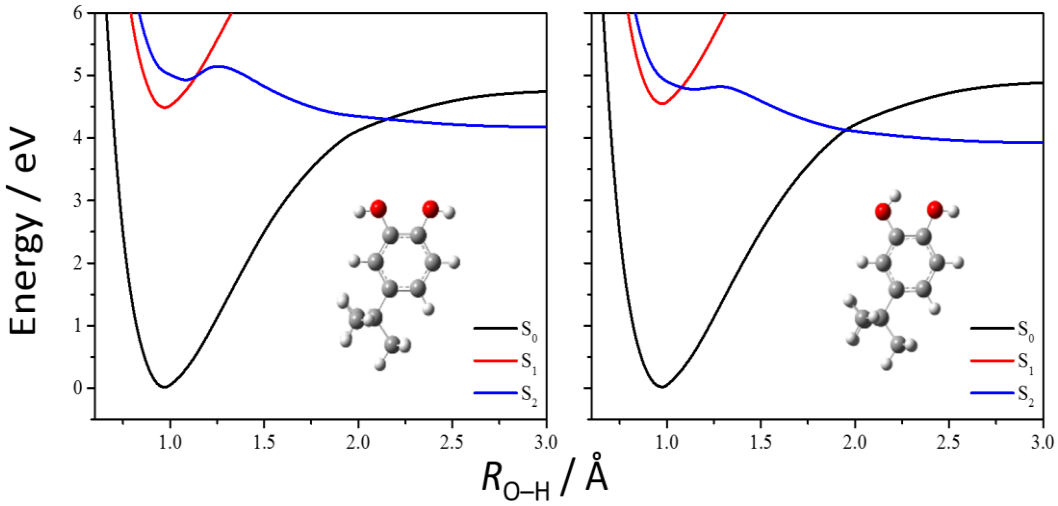

Figure 3.7 Calculated potential energy cuts along the extension of the "free" O–H of both the open conformer (left) and closed conformer (right) of 4-TBC in the gas-phase. The first three states are shown: the S_0 ground state (black), the S_1 $^1\pi\pi^*$ state (red) and the S_2 $^1\pi\sigma^*$ state (blue). Potential energy cuts were calculated in Gaussian 09 using CASSCF with a second order perturbation correction CASPT2, using an aug-cc-pVDZ basis set.

localised along the O–H bond coordinate. This is illustrated in the potential energy cuts shown in Figure 3.7 for the open and closed conformers, the latter preserving the intramolecular hydrogen bond. We return to discuss the significance of the open and closed conformers in the proceeding paragraphs.

Collecting a series of TKER spectra at varying Δ*t* and then integrating the high KE feature over the range ~5,500–8,500 cm^{-1} results in the H^+ transient shown in Figure 3.6b (blue circles). In order to obtain a time constant for the S_2 mediated O–H dissociation, a kinetic fit to the data is applied; this fit is shown by the blue line. Two (gas-phase, g) time constants (τ) are returned: ${}^{g}\tau_{MP}$ < 30 fs, which is associated with multiphoton processes (MP),[14,15] and a slower rise in the H^+ (and thus H atom) signal, ${}^{g}\tau_{H^+}$ = 5.9 ± 0.3 ps, which is likely due to quantum tunnelling beneath an S_1/S_2 conical intersection (CI, *vide infra*).[11] In addition to the H^+ transient, Figure 3.6b also shows a complementary TR-IY trace of the 4-TBC^+ parent ion signal, as a function of Δ*t* (purple diamonds), which provides a measure of the dynamics occurring on the photoprepared S_1 state following excitation at 267 nm. Cursory inspection of the 4-TBC^+ parent transient relative to the corresponding H^+ transient reveals that the S_1 state decays on a similar time scale to the appearance of H atoms associated with O–H dissociation. Indeed, fitting this transient with a biexponential decay function (purple line) returns time constants of ${}^{g}\tau_{IVR(H)}$ = 0.4 ± 0.1 ps, associated with rapid intramolecular vibrational redistribution (IVR) in the S_1 state as seen in our previous investigation in catechol,[11] and ${}^{g}\tau_{P^+}$ = 4.9 ± 0.6 ps, which is assigned to excited state population flux from the S_1 state, with the P^+ signifying decay of the nondeuterated isotopologue parent ion signal (and therefore S_1 state population). The difference between ${}^{g}\tau_{P^+}$ and ${}^{g}\tau_{H^+}$ is attributed to the parent signal decaying quicker due to the progression out of the Franck-Condon region, reducing the overlap between the excited state and dissociative state. Importantly, this shows a clear correlation to the appearance time of H^+.

To establish the role of tunnelling following photoexcitation to S_1, we have also carried out measurements on 4-TBC-d_2. The results of both the D^+ and 4-TBC-$d_2{}^+$ transients are shown in Figure 3.6c. Kinetic fits to the transients return time constants of ${}^{g}\tau_{D^+}$ = 98 ± 2 ps and ${}^{g}\tau_{DP^+}$ = 102 ± 3 ps and thus an average kinetic isotope effect (KIE, where KIE=k_H/k_D) of ~19. Here the time constant typography has the same meaning as above, but applied to the deuterated isotopologue. The large KIE obtained here is a tell-tale signifier that the "free" O–H dissociation is very likely mediated through tunnelling under the S_1/S_2 CI. For completeness, we also note that ${}^{g}\tau_{IVR(D)}$ = 1.0 ± 0.1 ps compares favourably with the value extracted for the nondeuterated isotopologue. Notably, the KIE

obtained for 4-TBC is similar to measurements carried out in catechol, which returned a KIE of ~30, supporting the use of 4-TBC as a proxy for catechol (*vide supra*).

3.3.2 Solution-Phase Studies

The nonpolar solvent, cyclohexane, was used as the starting point for unravelling the solution-phase dynamics of 4-TBC, as the weakly perturbing environment of cyclohexane serves as a good model for the gas-phase environment.[1,16] Figure 3.8a shows TAS of 4-TBC in cyclohexane, following 267 nm (4.65 eV) excitation, having two main features at early Δt (~1–5 ps): a peak centred around 370 nm and another broader feature centred at 495 nm. These features are attributed to the excited state absorption

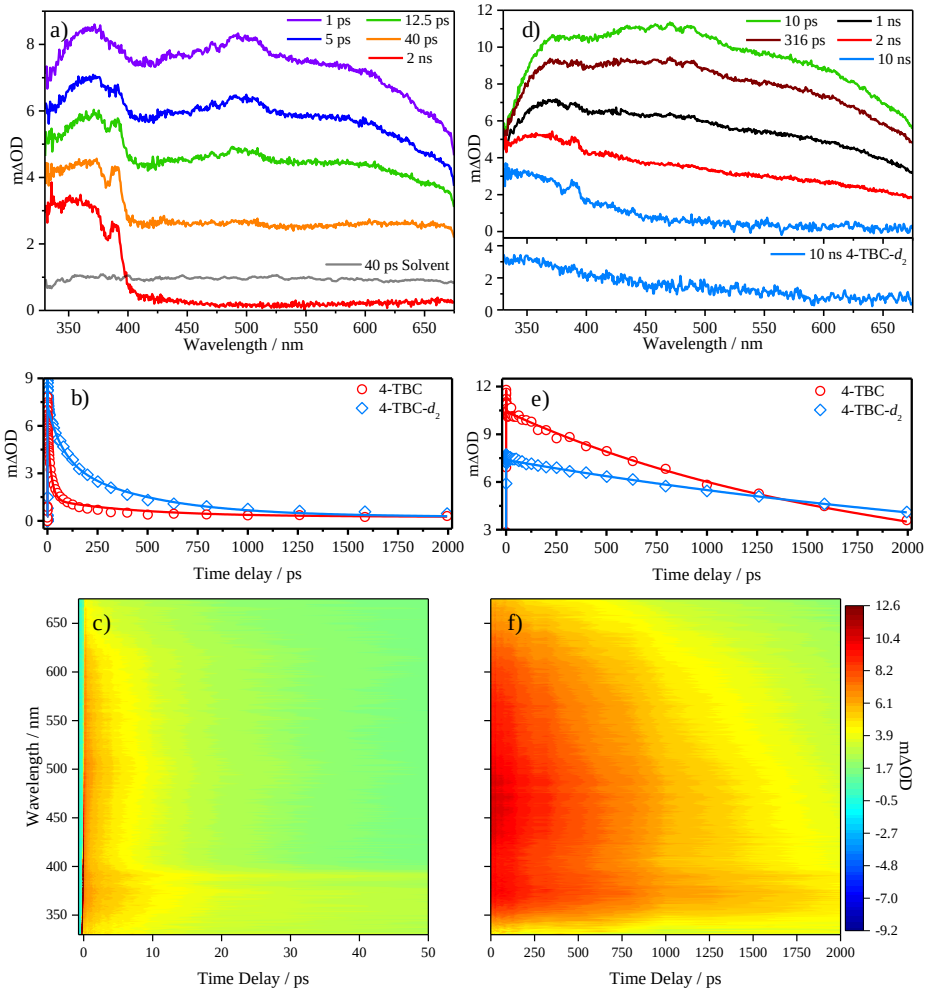

Figure 3.8 a) Selection of TAS of 35 mM 4-TBC in cyclohexane with an excitation wavelength of 267 nm. b) Transient slices of 35 mM 4-TBC in cyclohexane (red circles) and 35 mM 4-TBC-d_2 in cyclohexane (blue diamonds) acquired by integrating over a 5 nm window centred at 450 nm; solid lines are the kinetic fits. c) heat map representation of the cyclohexane TAS d) Selection of TAS of 35 mM 4-TBC in acetonitrile and 30 mM 4-TBC-d_2 in acetonitrile (bottom trace) with an excitation wavelength of 267 nm. e) Transient slices of 35 mM 4-TBC in acetonitrile (red circles) and 30 mM 4-TBC-d_2 in acetonitrile (blue diamonds) acquired by integrating over a 5 nm centred at 450 nm; solid lines are the kinetic fits. Note that optical density is plotted in the range mΔOD = 3-12 to magnify the extended decay. f) heat map representation of the acetonitrile TAS.

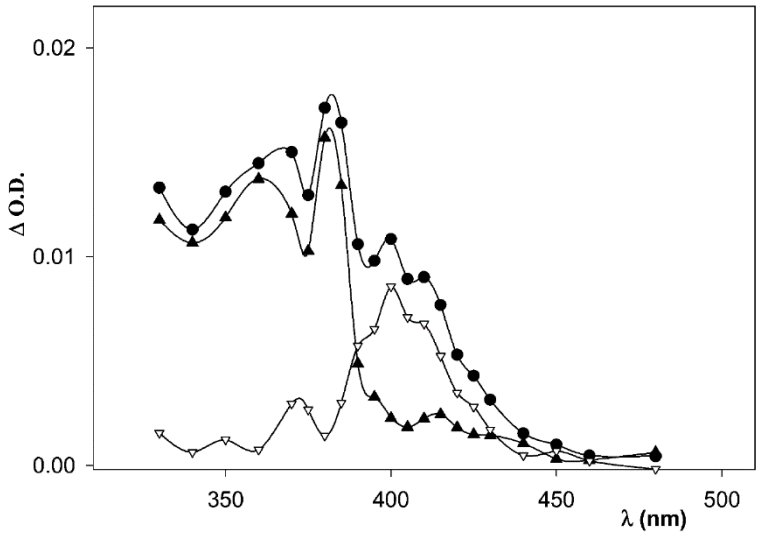

Figure 3.9 The absorption profiles of the catechol radical (solid triangles), the radical cation (open triangles) and there combined profile (circles).

(ESA) from the S_1 state to higher-lying S_n states.[17,18] At Δt = 5 ps, peaks at 375 and 390 nm appear to lie on top of the S_1 absorption; these peaks are the signature absorption of 4-TBC• (and not the radical cation) in concordance with literature on other phenols.[19,20] The radical and radical cation absorption are shown in Figure 3.9. The peak at 390 nm (and to a lesser extent 375 nm) appears to narrow as the spectra evolve over time (Δt = 5–40 ps). This may be explained by quenching of the initially produced hot radical through vibrational energy transfer (VET).[21,22]

Within these features, a significant cyclohexane solvent response is also present and appears as a flat absorption feature spanning the entire probe window and the evolution of this ESA is shown in Figure 3.10a. The origins of this solvent response is due to two-photon ionization of the cyclohexane which initial generates a geminate pair between

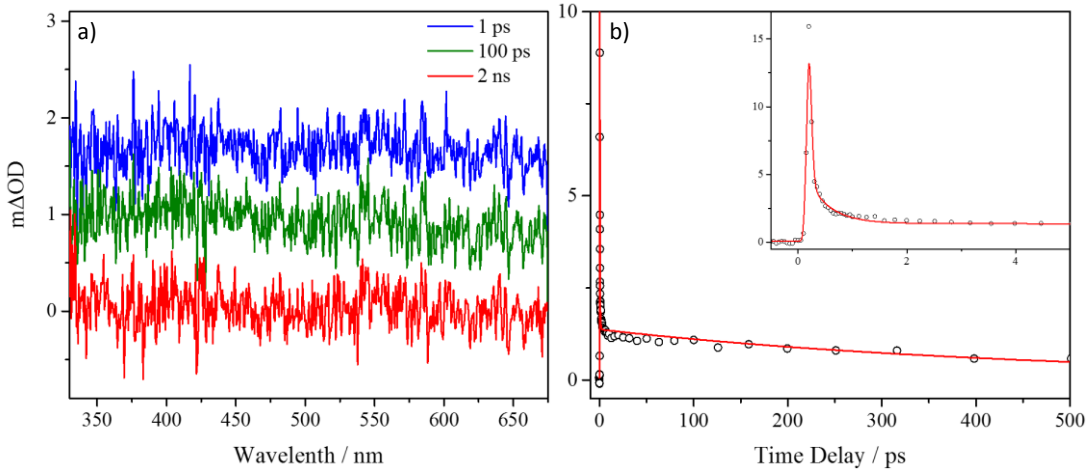

Figure 3.10 a) Selection of TAS of neat cyclohexane at an excitation wavelength of 267 nm. b) Transient slice at 450 nm for neat cyclohexane excited at 267 nm. A kinetic fit is shown by the red line.

the ejected election can cyclohexane cation. This geminate pair than rapidly recombines to produce cyclohexane in its first excited singlet state.[23] The TAS of neat cyclohexane were obtained in an identical manner to 4-TBC in cyclohexane and a transient, shown in Figure 3.10b, was acquired by integrating a 5 nm wide slice of the TAS, centred on 450 nm, as a function of Δ*t*. The reason behind the choice of this integration wavelength is provided below. This transient was fitted with a triexponential decay function, revealing three lifetimes that we attribute to the solvent (s) response: τ_{s1} = 23 ± 1 fs,[††††] τ_{s2} = 408 ± 148 fs and τ_{s3} = 447 ± 55 ps.

Returning once again to 4-TBC in cyclohexane, Figure 3.8b (red circles) shows a transient acquired by integrating a 5 nm wide slice of the TAS, centred on 450 nm, as a function of Δ*t*. This wavelength is chosen due to the absence of radical absorption in this region, ensuring that signal at this wavelength will come primarily from S_1 absorption. This transient was fit with a tetraexponential decay function (red line); the first three exponentials account for the cyclohexane solvent response (see above). The single time constant found for (non-deuterated, *i. e.*, H) 4-TBC in cyclohexane (c), $^{c}\tau_{(H)}$ = 18 ± 1 ps, is assigned to excited state population flux out of the S_1. TAS of 4-TBC-d_2 were also recorded, as shown by Figure 3.11a, to acquire a corresponding 4-TBC-d_2 transient centred at 450 nm. This was once again using a 5 nm integration around this spectral region; the results are presented in Figure 3.8b (blue diamonds). Our kinetic fit (blue line) returns an S_1 lifetime for the deuterated (D) species of $^{c}\tau_{(D)}$ = 74 ± 9 ps and thus a KIE of ~4. While the KIE returned from the cyclohexane measurements is less than that obtained from the gas-phase measurements (cf. KIE ~19), this still suggests O–H

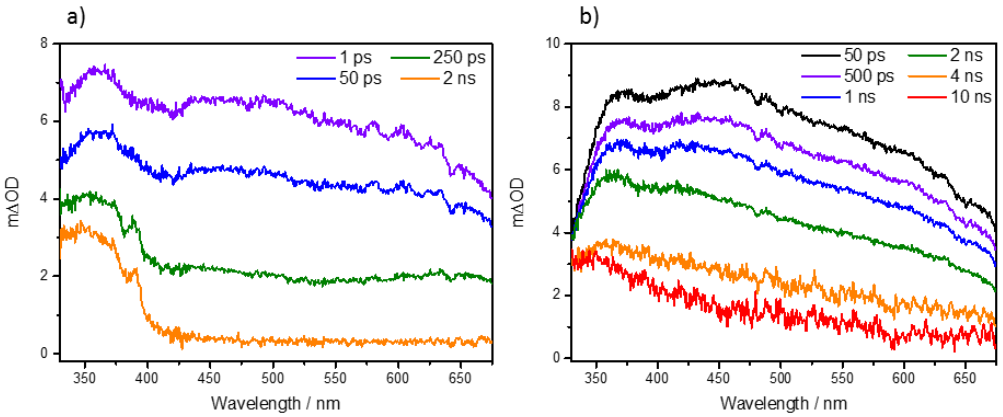

Figure 3.11 a) Selection of TAS of 35 mM 4-TBC-d_2 in cyclohexane and b) 30 mM 4-TBC-d_2 in acetonitrile with an excitation wavelength of 267 nm.

[††††] While generally we cannot quote lifetimes shorter than 40 fs, we quote the exact value here due to it being used in the fit for 4-TBC and 4-TBC-$d_2$cyclohexane.

dissociation is a barriered process with some *possible* involvement of tunnelling (*vide infra*).[24]

We now begin to evaluate the environmental influence on the excited state dynamics of 4-TBC by using a more perturbative, polar solvent. Acetonitrile was selected due to its high polarity and (apparent) low reactivity toward 4-TBC.‡‡‡‡ Figure 3.8c shows the TAS of 4-TBC in acetonitrile. The main feature at early Δt is a broad ESA across the entire probe window, which we once again attribute to absorption from the S_1 state to higher-lying S_n states.[17,18] At Δt = 300 ps, a smaller peak, which is assigned to the 4-TBC$^{\bullet}$ absorption, sits atop the S_1 state absorption at 390 nm. Beyond Δt = 2 ns, this radical signature appears more defined and the S_1 state absorption has decayed away sufficiently to reveal an absorption resembling that of an excited triplet state; these absorptions tend to slope up in the blue end of the spectrum.[25] By Δt = 10 ns the S_1 absorption appears to have completely decayed yielding the triplet state and radical species absorptions, reminiscent of previous studies in guaiacol.[18] TAS of 4-TBC-d_2 in acetonitrile do not show, within the signal-to-noise, the radical absorption; a Δt = 10 ns TAS is shown in the lower panel in Figure 3.8c, alongside more expansive TAS collated at a range of Δt shown in Figure 3.11b, highlights this. Unlike the transients obtained in cyclohexane, the transient in acetonitrile (Figure 3.8d) requires only two exponential decay functions to fit the data (red line), both of which are attributed to solute-only dynamics. Solvent contribution from acetonitrile was negligible and thus not shown. The (acetonitrile, a) time constants returned from the kinetic fit are ${}^{a}\tau_{VET(H)}$ = 230 ± 50 fs and ${}^{a}\tau_{(H)}$ = 1.7 ± 0.1 ns. The very fast decay manifests due to a decrease in the ESA as the Franck–Condon overlap for the $S_n \leftarrow S_1$ absorption evolves. This is attributed to both IVR and solvent rearrangement, the latter of which has been shown to influence the S_1 energy of the solute.[26] We note we are unable to resolve a similar decay pathway in 4-TBC/ cyclohexane due to the very large solvent-only dynamics at short time delays, though it would be expected that a similar process to that seen in acetonitrile would occur.

The second extracted time constant, ${}^{a}\tau_{(H)}$ = 1.7 ± 0.1 ns, is assigned to excited state population flux out of the S_1 state in accordance with our previous studies on guaiacol.[18] Intriguingly, we note there is a ~100-fold increase in the lifetime of the S_1 state in acetonitrile relative to cyclohexane (cf. ${}^{c}\tau_{(H)}$ = 18 ± 1 ps), the significance of which is discussed below. TAS of 4-TBC-d_2 in acetonitrile collected and then integrated with a 5 nm wide slice centred around 450 nm yielded a similar transient, and is presented in

‡‡‡‡ In methanol a yellowing of the sample occurred, we believe this to be caused by the solvent reacting with the 4-TBC to produce a quinone type species.

Figure 3.8d. Our kinetic fit (blue line) returned an S_1 lifetime of a $\tau_{(D)}$ = 3.3 ± 0.1 ns (as well as $^{a}\tau_{VET(D)}$ = 180 ± 50 fs for completeness) and thus a KIE of ~1.9, which suggests that the rate determining step in the excited state decay is inconclusive regarding whether it is a barriered process of not.

3.3.3 Gas-Phase Versus Solution-Phase Studies

We now compare our findings between the gas- and solution-phases. In the gas-phase, the parent^{+} transient, which directly reports on the S_1 lifetime, returns a time constant of $^{g}\tau_{(H)}$ = 4.9 ± 0.6 ps while the S_1 lifetime in cyclohexane is $^{c}\tau_{(H)}$ = 18 ± 1 ps. The almost 4-fold increase in the S_1 lifetime in cyclohexane may be attributed to the very modest polarity of cyclohexane (dielectric constant (ε_r) = 2.02),[27] which will perturb, albeit weakly, the electronic state energies. The KIE returned from both the gas- and solution-phases (gas ~19, solution ~4) suggests that, following excitation to S_1, O−H dissociation proceeds along a barriered pathway. Our attribution of tunnelling mediated dissociation along the "free" O−H bond (more so for the gas-phase with the larger KIE and a milder tunnelling behaviour in cyclohexane), beneath an S_1/S_2 CI, accords with previous studies on phenols in the gas- and solution-phases.[2,16-18,28] Studies on substituted phenols have also shown the quite dramatic effect substituents have on the topography of either the S_1 or S_2 (or both) potential energy surfaces (PES), resulting in noticeable effects on the S_1/S_2 tunnelling probability and hence S_1 lifetime.[11,29-32] Similar effects on the local topography of the S_1 or S_2 PESs even from a weakly perturbing solvent will undoubtedly have a comparable effect on the S_1 lifetime as observed here. Indeed, the increase in the S_1 lifetime in cyclohexane relative to the gas-phase (see above) suggests that the barrier along the O−H bond increases due to a stabilization of the S_1 state, destabilization of the S_2 state, or a combined effect. As discussed previously in Chapter 1 the rate of tunnelling displays an exponential dependence on the barrier height, therefore any small change in the barrier will have an appreciable effect on the observed time constant. However, this is counterintuitive to the observed decrease in KIE in cyclohexane; an increase in barrier would imply an increase in KIE (due to the increasing role of tunnelling along the O−H or O−D coordinate). One must recognize, however, that the KIE is dependent upon both the barrier height along the O−H coordinate and the influence of orthogonal modes and zero-point effects which may aid passage across (or through) this barrier. As such, a more complete description of the KIE requires proper treatment of the nuclear dynamics beyond a simple 1-D picture, which utilizes the multidimensional PES and how these are influenced by the nonpolar cyclohexane (and polar acetonitrile−see below).

While the gas-phase studies are relatively similar with those in the nonpolar cyclohexane, as expected, this is not the case in acetonitrile (ε_r = 37.5).[33] The S_1 lifetime of 4-TBC in acetonitrile, ${}^{a}\tau_{(H)}$ = 1.7 ± 0.1 ns, is ~100 times that of 4-TBC in cyclohexane and ~350 times that of gas-phase 4-TBC (${}^{c}\tau_{(H)}$ = 18 ± 1 ps and ${}^{g}\tau_{P+}$ = 4.9 ± 0.6 ps respectively). The polar acetonitrile is thought to induce the same conformer change to 4-TBC as with catechol, where the intramolecular hydrogen bond is broken, resulting in two intermolecular hydrogen bonds with the solvent.[34,35] To explore the role of conformational change on the observed dynamics, time-dependent density functional theory calculations were performed with the Gaussian 09[36] package using both the M052X[37] and CAM-B3LYP[38] functionals and a 6- 311G**[39] basis set. These calculations show that the "open" and "closed" conformers are planar in the S_0 state (see Figure 3.12). In contrast, in the S_1 state, while the "open" conformer retains planarity, the "closed" conformer becomes distorted.

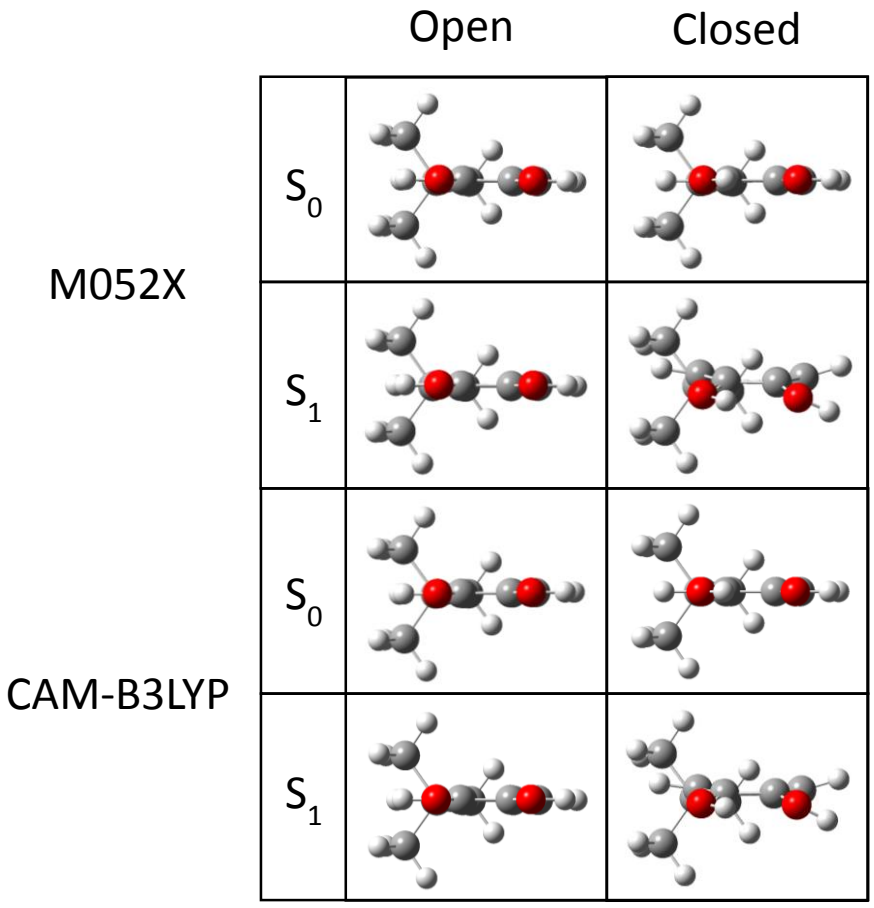

Figure 3.12 Calculated minimum geometries in the ground state (S_0) and first excited state (S_1) of 4-TBC in its intramolecular hydrogen bonded (closed) and non-intramolecular hydrogen bonded (open) conformers, calculated in Gaussian09 using M052X and CAM-B3LYP functionals with a 6-311G** basis set.

In the gas-phase and in cyclohexane, the photoexcited S_1 state is nonplanar.[40] The nonplanar "closed" conformer has been proposed to explain the dramatic decrease in S_1 lifetime in catechol relative to phenol, due to symmetry enhanced tunnelling.[11,41] A similar reasoning can be applied here for 4- TBC in both "non-perturbing" environments, of the isolated gas-phase and non-polar cyclohexane solution. In the polar solvent, acetonitrile, the photoexcited S_1 state retains its planar geometry (see Figure 3.12). Such a conformer change (with solvent polarity) has also been observed in guaiacol,[34,35] resulting in considerably altered photodynamics.[18] In 4-TBC we see an analogous alteration in the observed photodynamics of the S_1 excited state in the form of an increased lifetime, an appearance of the triplet state absorption, whose absorption is similar to phenol's triplet absorption profile,[25] at large values of Δt, and a smaller radical absorption appearing at $\Delta t \sim 300$ ps and beyond. These dynamics are extremely similar to those seen for guaiacol in methanol[18] as well as bearing a resemblance to their archetype, phenol in cyclohexane.[16,17] This leads to the conclusion that a solvent-induced conformer change most likely causes the suppression of the O−H bond fission pathway, likely due to an enhanced barrier to tunnelling, allowing for additional decay pathways such as IC, fluorescence, and ISC to effectively compete with "free" O−H dissociation.[17,18,42] The absence of 4-TBC-d_1• out to Δt = 10 ns in our deuterated studies supports this idea; O−D bond fission is kinetically outcompeted by other pathways, which will now contribute to the measured KIE of ~1.9, and is unsurprising given that D atom tunnelling through the barrier beneath an S_1/S_2 CI will be significantly suppressed. As such, we see an increase in the triplet state signal. We must recognize that the solvent will also modify the S_1 and S_2 state topographies irrespective of any conformational change. Therefore, both processes (conformational change and solvent perturbations) are intimately linked in modifying the S_1 and S_2 state energies. Combined, this leads to an enhanced barrier to O−H bond fission and thus suppression of the O−H bond fission pathway.

On the basis of our discussion above, a proposed schematic summarizing the various decay pathways in 4-TBC, in both perturbative and non-perturbative environments, is given in Figure 3.13. Photoexcitation with 267 nm radiation prepares 4- TBC in the S_1 state. In the gas-phase, the excited state decays through dissociation of the "free" O−H bond, along a pathway that has a barrier. The KIE of ~19 strongly suggests that O−H dissociation is mediated through tunnelling beneath the S_1/S_2 CI. In the weakly perturbing cyclohexane solvent, the photoexcited S_1 state decay appears to follow a similar path: tunnelling mediated O−H dissociation. While a milder KIE of ~4 makes this supposition less conclusive, it is still supportive of a barriered O−H dissociation

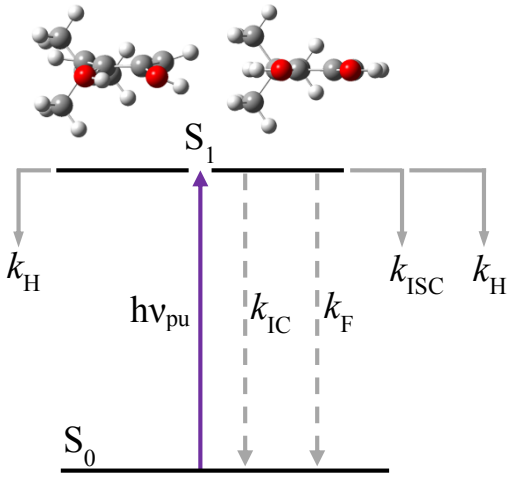

Figure 3.13 Schematic representation of the observed decay processes in 4-TBC. The left side demonstrates the S_1 decay of the 'closed' (non-planar) conformer, which dominates in the gas-phase and in the non-polar cyclohexane. The right side shows the S_1 decay of the 'open' (planar) conformer, which dominates in the polar acetonitrile. Dashed grey arrows represent processes that our current measurements cannot/do not probe and are based on previous work in related systems (see text for details).

coordinate. The left side of Figure 3.12 contains a single, dominant process involved in the non-perturbative, gas-phase and weakly perturbative, (cyclohexane) solution-phase: k_H signifies the rate constant of O–H dissociation. In the strongly perturbing acetonitrile solvent, we have contrasting dynamics. The "open" conformer, which now dominates, displays a diminished 4-TBC• feature. Upon deuteration, the 4-TBC-d_1• absorption signature is almost completely extinguished. Instead, the excited state decay reveals an absorption feature in the TAS that is reminiscent of triplet state absorption. As a consequence, we propose that excited state decay in 4-TBC (acetonitrile) is multicomponent in nature, including O–H dissociation, ISC, and likely IC and fluorescence, characterized by the associated rate constants k_H, k_{ISC}, k_{IC}, and k_F respectively. The right side of Figure 3.13 shows these processes.

We close by returning to the original question regarding whether the natural surroundings impact the photostability of biomolecules. In 4-TBC, a close analogue to the catechol chromophore, it is clear that the photoinduced dynamics in non-perturbing environments compare favourably with those in the gas-phase; both cases involve O–H dissociation to yield the phototoxic radical species 4-TBC•.[43] When 4-TBC is placed into a polar solvent, this pathway is severely suppressed. This is a consequence of a change in molecular geometry, as well as electronic structure, through solvent interactions. These structural changes reduces the excited state decay, with the phototoxic radical pathway becoming less favourable, and opens up alternative (and competitive) relaxation pathways, including potentially harmful triplet state formation.[10] Interestingly, the triplet state formation accords with previous studies by Sundström

and co-workers on 5,6-dihydroxyindole,[9] one of the main building blocks of eumelanin, which incorporates the catechol chromophore motif. Thus, the present bottom-up study provides a key stepping-stone between a model UV chromophore (motif) in the gas-phase and a larger biomolecule within its native environment. This also emphasizes the critical role of environment-induced photodynamics.

3.4 Conclusions

The excited state dynamics of 4-TBC have been investigated in both the gas- and solution-phases using a combination of TR-VMI, TR-IY, and TEAS, following photoexcitation of the $S_1(^1\pi\pi^*)$ state at 267 nm. Through the recorded gas-phase TKER spectra and associated H^+ transient, a time constant for H atom elimination of ${}^g\tau_{H^+} = 5.9 \pm 0.3$ ps is found. Complementary TR-IY transients of the parent$^+$ results in a time constant of ${}^g\tau_{P^+} = 4.9 \pm 0.6$ ps. Comparative studies in 4-TBC-d_2 yield time constants of ${}^g\tau_{D^+} = 98 \pm 2$ ps and ${}^g\tau_{DP^+} = 102 \pm 3$ ps and thus an average KIE of ~19. A dominant dissociation of the non-intramolecular hydrogen bonded "free" O–H bond is deduced, very likely mediated through tunnelling beneath an S_1/S_2 CI. Solution-phase studies in the weakly perturbing cyclohexane solvent yield excited state decay time constants of ${}^c\tau_{(H)} = 18 \pm 1$ ps and ${}^c\tau_{(D)} = 74 \pm 9$ ps for 4-TBC and 4-TBC-d_2 respectively. The KIE of ~4 implies, together with the emergent 4-TBC-d_1• feature, that a similar relaxation pathway in 4-TBC/cyclohexane is operative as in 4-TBC in the gas-phase: a barriered pathway to O–H dissociation with a milder contribution of tunnelling. In the strongly perturbing, polar acetonitrile solvent, excited state decay occurs with time constants of ${}^a\tau_{(H)} = 1.7 \pm 0.1$ ns and ${}^a\tau_{(D)} = 3.3 \pm 0.1$ ns for 4-TBC and 4-TBC-d_2 respectively, leading to a KIE of ~1.9. The dominant decay channel in acetonitrile is no longer solely O–H dissociation, but rather multicomponent, involving ISC, IC, and fluorescence together with O–H dissociation. The dramatic differences in excited state lifetime in the two solvents is largely attributed to a conformational change between 4-TBC (and 4- TBC-d_2) in cyclohexane and acetonitrile, in which, respectively, the closed and open conformers dominate. This result thus serves to highlight the critical importance of the influence of environment and structure on dynamics. Furthermore, this work serves as a starting point for the work presented in Chapter 4, as caffeic acid is a functionalized form of 4-TBC. Additionally, the effects of differing solvent environments are explored, which as shown in this chapter, can have a drastic impact on the observed dynamics.

3.5 Bibliography

1. G. M. Roberts and V. G. Stavros, *Chem. Sci.*, 2014, **5**, 1698-1722.
2. M. Staniforth and V. G. Stavros, *Proc. R. Soc. A*, 2013, **469**, 20130458.

3. P. Meredith and T. Sarna, *Pigm. Cell Res.*, 2006, **19**, 572-594.
4. N. Kollias, R. M. Sayre, L. Zeise and M. R. Chedekel, *J. Photochem. Photobiol. B*, 1991, **9**, 135-160.
5. T. Sarna, *J. Photochem. Photobiol. B*, 1992, **12**, 215-258.
6. A. Corani, A. Pezzella, T. r. Pascher, T. Gustavsson, D. Markovitsi, A. Huijser, M. d'Ischia and V. Sundström, *J. Phys. Chem. Lett.*, 2013, **4**, 1383-1388.
7. A. Huijser, A. Pezzella and V. Sundström, *Phys. Chem. Chem. Phys.*, 2011, **13**, 9119-9127.
8. M. Gauden, A. Pezzella, L. Panzella, M. T. Neves-Petersen, E. Skovsen, S. B. Petersen, K. M. Mullen, A. Napolitano, M. d'Ischia and V. Sundstrom, *J. Am. Chem. Soc.*, 2008, **130**, 17038-17043.
9. M. Gauden, A. Pezzella, L. Panzella, A. Napolitano, M. d'Ischia and V. Sundström, *J. Phys. Chem. B*, 2009, **113**, 12575-12580.
10. S. Premi, S. Wallisch, C. M. Mano, A. B. Weiner, A. Bacchiocchi, K. Wakamatsu, E. J. H. Bechara, R. Halaban, T. Douki and D. E. Brash, *Science*, 2015, **347**, 842-847.
11. A. S. Chatterley, J. D. Young, D. Townsend, J. M. Zurek, M. J. Paterson, G. M. Roberts and V. G. Stavros, *Phys. Chem. Chem. Phys.*, 2013, **15**, 6879-6892.
12. J. Borovansky and P. A. Riley, *Melanins and Melanosomes: Biosynthesis, Structure, Physiological and Pathological Functions*, John Wiley & Sons, Germany, 2011.
13. M. Staniforth, J. D. Young, D. R. Cole, T. N. V. Karsili, M. N. R. Ashfold and V. G. Stavros, *J. Phys. Chem. A*, 2014, **118**, 10909-10918.
14. G. M. Roberts, A. S. Chatterley, J. D. Young and V. G. Stavros, *J. Phys. Chem. Lett.*, 2012, **3**, 348-352.
15. G. M. Roberts, C. A. Williams, H. Yu, A. S. Chatterley, J. D. Young, S. Ullrich and V. G. Stavros, *Farad. Discuss.*, 2013, **163**, 95-116.
16. S. J. Harris, D. Murdock, Y. Zhang, T. A. Oliver, M. P. Grubb, A. J. Orr-Ewing, G. M. Greetham, I. P. Clark, M. Towrie, S. E. Bradforth and M. N. R. Ashfold, *Phys. Chem. Chem. Phys.*, 2013, **15**, 6567-6582.
17. Y. Zhang, T. A. A. Oliver, M. N. R. Ashfold and S. E. Bradforth, *Farad. Discuss.*, 2012, **157**, 141-163.
18. S. E. Greenough, M. D. Horbury, J. O. F. Thompson, G. M. Roberts, T. N. V. Karsili, B. Marchetti, D. Townsend and V. G. Stavros, *Phys. Chem. Chem. Phys.*, 2014, **16**, 16187-16195.
19. O. Brede, S. Kapoor, T. Mukherjee, R. Hermann and S. Naumov, *Phys. Chem. Chem. Phys.*, 2002, **4**, 5096-5104.
20. E. J. Land and G. Porter, *T. Faraday Soc.*, 1963, **59**, 2016-2026.

21. J. C. Owrutsky, D. Raftery and R. M. Hochstrasser, *Annu. Rev. Phys. Chem.*, 1994, **45**, 519-555.
22. J. Aßmann, M. Kling and B. Abel, *Angew. Chem. Int. Ed.*, 2003, **42**, 2226-2246.
23. H. Miyasaka and N. Mataga, *Chem. Phys. Lett.*, 1986, **126**, 219-224.
24. A. Douhal, F. Lahmani and A. H. Zewail, *Chem. Phys.*, 1996, **207**, 477-498.
25. D. V. Bent and E. Hayon, *J. Am. Chem. Soc.*, 1975, **97**, 2599-2606.
26. E. W. Castner Jr, M. Maroncelli and G. R. Fleming, *J. Chem. Phys.*, 1987, **86**, 1090-1097.
27. S. Malanowski, R. Patz, M. Rätzsch and C. Wohlfarth, *FFE*, 1979, **3**, 291-312.
28. T. A. A. Oliver, Y. Zhang, M. N. R. Ashfold and S. E. Bradforth, *Farad. Discuss.*, 2011, **150**, 439-458.
29. D. J. Hadden, G. M. Roberts, T. N. V. Karsili, M. N. R. Ashfold and V. G. Stavros, *Phys. Chem. Chem. Phys.*, 2012, **14**, 13415-13428.
30. J. D. Young, M. Staniforth, A. S. Chatterley, M. J. Paterson, G. M. Roberts and V. G. Stavros, *Phys. Chem. Chem. Phys.*, 2013, **16**, 550-562.
31. T. N. V. Karsili, A. M. Wenge, S. J. Harris, D. Murdock, J. N. Harvey, R. N. Dixon and M. N. R. Ashfold, *Chem. Sci.*, 2013, **4**, 2434-2446.
32. G. A. Pino, A. N. Oldani, E. Marceca, M. Fujii, S.-I. Ishiuchi, M. Miyazaki, M. Broquier, C. Dedonder and C. Jouvet, *J. Chem. Phys.*, 2010, **133**, 124313.
33. J.-F. Côté, D. Brouillette, J. E. Desnoyers, J.-F. Rouleau, J.-M. St-Arnaud and G. Perron, *J. Solution Chem.*, 1996, **25**, 1163-1173.
34. M. A. Varfolomeev, D. I. Abaidullina, A. Z. Gainutdinova and B. N. Solomonov, *Spectrochim. Acta Mol. Biomol. Spectrosc.*, 2010, **77**, 965-972.
35. J. T. Navarrete and F. J. Ramirez, *Spectrochim. Acta A. Mol. Spectrosc.*, 1993, **49**, 1759-1767.
36. M. J. Frisch, G. W. Trucks, H. B. Schlegel, G. E. Scuseria, M. A. Robb, J. R. Cheeseman, G. Scalmani, V. Barone, B. Mennucci, G. A. Petersson, H. Nakatsuji, M. Caricato, X. Li, H. P. Hratchian, A. F. Izmaylov, J. Bloino, G. Zheng, J. L. Sonnenberg, M. Hada, M. Ehara, K. Toyota, R. Fukuda, J. Hasegawa, M. Ishida, T. Nakajima, Y. Honda, O. Kitao, H. Nakai, T. Vreven, J. A. Montgomery, Jr., J. E. Peralta, F. Ogliaro, M. Bearpark, J. J. Heyd, E. Brothers, K. N. Kudin, V. N. Staroverov, R. Kobayashi, J. Normand, K. Raghavachari, A. Rendell, J. C. Burant, S. S. Iyengar, J. Tomasi, M. Cossi, N. Rega, J. M. Millam, M. Klene, J. E. Knox, J. B. Cross, V. Bakken, C. Adamo, J. Jaramillo, R. Gomperts, R. E. Stratmann, O. Yazyev, A. J. Austin, R. Cammi, C. Pomelli, J. W. Ochterski, R. L. Martin, K. Morokuma, V. G. Zakrzewski, G. A. Voth,

P. Salvador, J. J. Dannenberg, S. Dapprich, A. D. Daniels, Ö. Farkas, J. B. Foresman, J. V. Ortiz, J. Cioslowski and D. J. Fox, *Wallingford, CT*, 2009, **19**, 227-238.

37. Y. Zhao, N. E. Schultz and D. G. Truhlar, *J. Chem. Theory Comput.*, 2006, **2**, 364-382.
38. T. Yanai, D. P. Tew and N. C. Handy, *Chem. Phys. Lett.*, 2004, **393**, 51-57.
39. R. B. J. S. Krishnan, J. S. Binkley, R. Seeger and J. A. Pople, *J. Chem. Phys.*, 1980, **72**, 650-654.
40. G. A. King, T. A. Oliver, R. N. Dixon and M. N. R. Ashfold, *Phys. Chem. Chem. Phys.*, 2012, **14**, 3338-3345.
41. M. Weiler, M. Miyazaki, G. r. Féraud, S.-i. Ishiuchi, C. Dedonder, C. Jouvet and M. Fujii, *J. Phys. Chem. Lett.*, 2013, **4**, 3819-3823.
42. R. Hermann, G. R. Mahalaxmi, T. Jochum, S. Naumov and O. Brede, *J. Phys. Chem. A*, 2002, **106**, 2379-2389.
43. L. J. Machlin and A. Bendich, *FASEB J.*, 1987, **1**, 441-445.

4. Photodynamics of Potent Antioxidants: Ferulic and Caffeic Acids

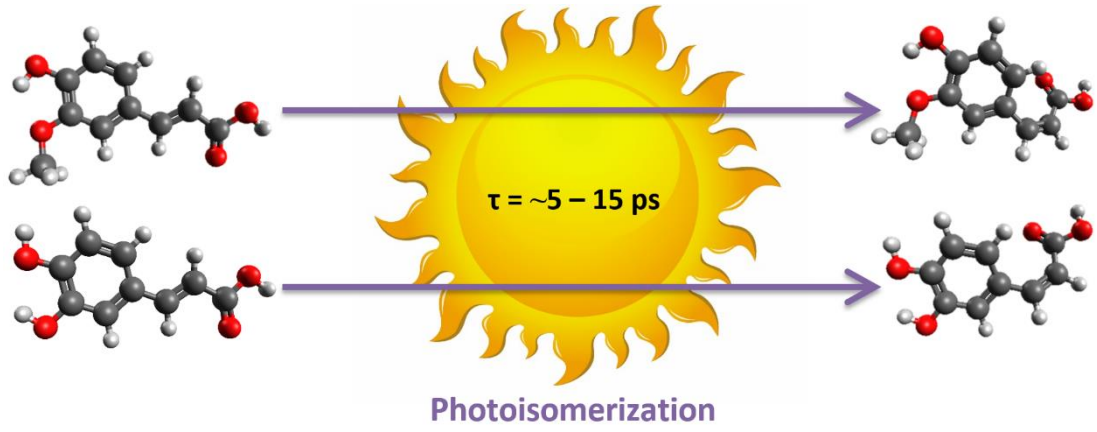

This chapter is based on the following submitted work:

> M. D. Horbury, L. A. Baker, W.-D. Quan, S. E. Greenough and V.G. Stavros, Photodynamics of Potent Antioxidants: Ferulic and Caffeic Acids, *submitted*.

Preparation of the buffer solutions was carried out by W.-D. Quan

4.1 Introduction

As discussed in Chapter 1, there is a lack of dynamical insight into the photodynamics of various sunscreening agents. Alongside this, there are also several controversies over certain molecules currently used within commercial sunscreens, in particular the formation of reactive oxygen species (ROS) due to photodegradation of the constituent components.[1,2] This has led to the concept of including molecules with antioxidant properties within sunscreen products, either to increase the photostability of sunscreen molecules, or to "mop up" any ROS.[2-4] A particularly potent set of antioxidants are hydroxycinnamic acids. Within this set, ferulic acid and caffeic acid, shown in Figure 4.1,[5,6] have been shown to stabilize vitamins C and E exposed to ultraviolet (UV) radiation.[7,8] These molecules also possess strong absorptions in the UVA (400 – 315 nm) and UVB (315 – 280 nm) regions (Figure 4.2); this is critical for their use as absorbing species in sunscreens.

Previous time-resolved studies have been performed on other related hydroxycinnamic acids, though much of this work has been focused upon the archetypal *p*-coumaric acid (3-(4-hydroxyphenyl)-2-propenoic acid) as either the isolated molecule or a functionalized chromophore to mimic the photoactive yellow protein (PYP).[9-16] In these studies, *p*-coumaric acid was excited to the first excited electronic state ($1^1\pi\pi^*$, S_1). The main relaxation pathway of the S_1 state was identified as a *trans-cis* photoisomerization, resulting in the formation of the *cis*-photoproduct. A two-step mechanism was proposed for this photoisomerization. The initial step involved geometry relaxation out of the vertical Franck-Condon (vFC) region to a local minimum in the S_1 state and a solvent reorientation. This was followed by the excited state crossing

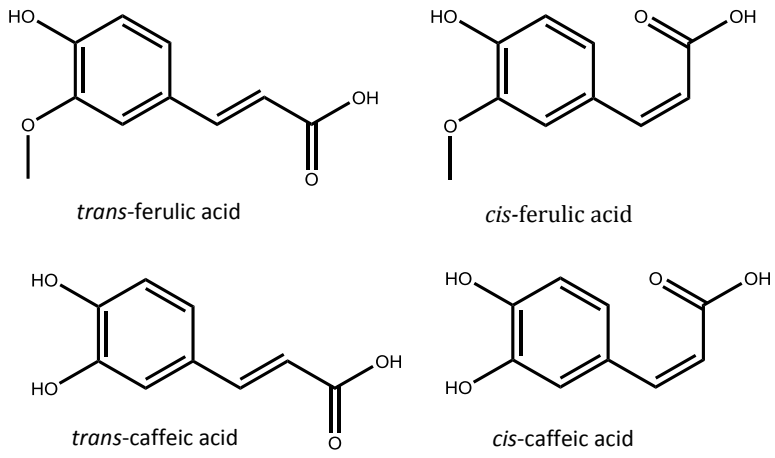

Figure 4.1 Structures of ferulic and caffeic acids in their *trans* and *cis* isomeric forms.

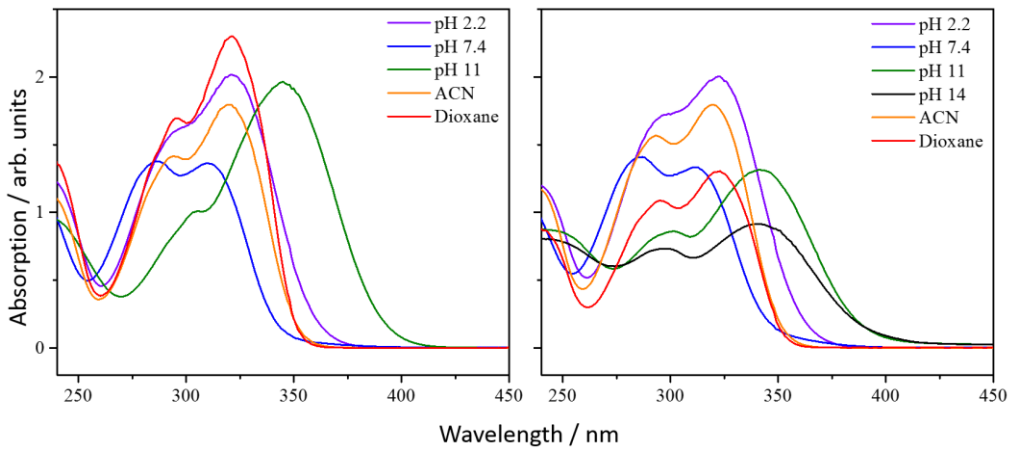

Figure 4.2 Static UV/vis spectra of ferulic (left) and caffeic (right) acids in several solvent environments.

a barrier along the isomerization reaction coordinate, proceeding to an S_1/S_0 conical intersection (CI) to either form the *cis*-isomer or return to the original *trans*-isomer.

Ferulic acid has also been studied previously, at different pHs, by van Grondelle and co-workers.[17] In this study, ferulic acid was photoexcited to the S_1 state, before probing the excited state decay with transient electronic (UV/visible) absorption spectroscopy (TEAS). A global analysis of their data required two time constants; except for ferulic acid at pH 10.5 which required three, to fully describe the dynamics data. The first time constant was attributed to a solvent rearrangement and geometry relaxation out of the initially populated vFC region (in accordance to *p*-coumaric acid, *vide supra*), which manifested as a change in the detected stimulated emission (SE). The second time constant was assigned to the decay of the excited state *via* an aborted isomerization as no *cis*-isomer was detected. This aborted isomerization in the propenoic acid "tail" of the molecule leads to a coupling between the S_1 state and the electronic ground state (S_0) by an S_1/S_0 CI. In contrast, static absorption studies of the effects of UV irradiation on both ferulic acid and caffeic acid have observed the formation of the *cis*-isomer after exposure to UV.[18-21] This was achieved by using chromatography to separate the two isomers from the irradiated solution.

Recent gas-phase *ab initio* calculations[22] for ferulic and caffeic acids have suggested that photoisomerization occurs in the $2^1\pi\pi^*$ (S_3) state (in contrast to occurring on the S_1 as proposed previously[21-28]) proceeding to a S_3/S_0 CI. Additionally, this work also highlighted a potential dissociation of the hydrogen atom on the phenolic hydroxyl group *via* tunnelling; this mechanism has been previously seen experimentally in the building blocks of ferulic and caffeic acids (guaiacol and catechol respectively),[23,24] and also discussed in Chapter 3. In light of these works, and the need for a better understanding of the photodynamics of ferulic acid and caffeic acid as sunscreening

agents, we use TEAS to revisit the photodynamics of ferulic acid and provide new insight toward the hitherto unstudied caffeic acid, following photoexcitation to the S_1 state, in a range of solvent environments of varying polarity.

4.2 Methods

The detailed experimental procedures pertaining to TEAS have been described in Chapter 2. In this section, we therefore provide information on the specifics concerning the experiments performed within this chapter. The wavelength range of the femtosecond white light continuum used in the probe pulse is 330-675 nm. The pump pulse employed the use of the TOPAS-C, using the following wavelengths: 319 nm (3.88 eV) for ferulic acid; and 314 nm (3.95 eV) for caffeic acid. These photoexcitation wavelengths correspond to the first absorption maximum in water at pH 2.2 (Figure 4.2), with fluences between 1 – 2 mJ cm^{-2}. The ferulic acid (99%, Sigma Aldrich) and caffeic acid (98%, Sigma Aldrich), samples were made to a concentration of 3 mM in: buffer solutions at pH 2.2 (50 mM Glygly), pH 7.4 (50 mM HEPES), pH 11 (50 mM Glygly) and pH 14 (caffeic acid only, 50 mM KCL) with nano-pure water, acetonitrile (≥99.9%, Sigma Aldrich) and dioxane (>99%, Fisher Chemical). A 100 μm optical path length was used in our Harrick Cell. The pH values were confirmed *via* a Accumet® portable AP110 pH meter (Fisher Scientific) which was calibrated with pH 4, 7 and 10 stock buffer solutions (Fisher Scientific).

In addition to the transient absorption spectra (TAS), static difference absorption spectra, which are referred to as "ΔUV/vis spectra" hereon, were collected. These were acquired by irradiating the solutions using an arc lamp (OBB, Tunable KiloArc) for 10 minutes. The desired irradiation wavelength was selected using a monochromator, providing light centred at the same wavelength as the pump wavelength in the TEAS measurements, with a 10 nm bandwidth and a power of 3 W. The "before" and "after" UV-vis spectra were obtained using a UV/vis spectrometer (Cary 300, Agilent Technologies). To generate the ΔUV/vis spectra, the "before" spectra were subtracted from the "after" spectra and then normalized.

4.3 Results

4.3.1 Transient Absorption Spectra

We first consider the TAS of ferulic and caffeic acids in water at all pH levels studied here, which correspond to pH 2.2, pH 7.4, pH 11 and pH 14. The effects of pH on the alcohol (OH) and carboxylic acid (CO_2H) groups are shown in Figure 4.3 and Table 4.1 shows the level of protonation at each pH.[25] As one can see, at the lowest pH, both groups are fully

Table 4.1: Percentage protonation for each O–H group at the pH values used in the present studies. The labels $O–H_1$, $O–H_2$ and $O–H_3$ are expanded upon in Figure 4.3.Valuesare calculated using the equation $\mathbf{10}^{\boldsymbol{pH-pKa}} = [\boldsymbol{A}^-]/[\boldsymbol{HA}]$.[26]

		pKa		
		$O–H_1$	$O–H_2$	$O–H_3$
FERULIC ACID	pH	4.50	8.92	n/a
	2.2	99.50%	>99.99%	n/a
	7.4	0.13%	96.98%	n/a
	11	<0.01%	0.83%	n/a
CAFFEIC ACID	pH	4.38	8.58	11.50
	2.2	99.34%	>99.99%	>99.99%
	7.4	0.10%	93.40%	>99.99%
	11	<0.01%	0.38%	68.28%
	14	<0.01%	<0.01%	0.32%

protonated. At pH 7.4, the proton on the carboxylic acid group is removed. At pH 11, both the proton on the acid and the alcohol groups are removed. Finally, at the highest pH of 14, this is sufficient to now remove the proton from the second alcohol group on caffeic acid (in ferulic acid this is replaced by methyl).

Having considered the effects of pH on the alcohol and carboxylic acid groups, we are now poised to begin to appreciate the TAS collated at these pHs, which are shown in Figure 4.4. Broadly speaking, all the TAS display the same general features which we label **i**, **ii** and **iii**, in Figure 4.4, albeit their evolution and spectral positions differ. After the initial excitation to the S_1 state, the TAS possess three dominant features. The first of these is a large excited state absorption (ESA, **i**) centred around ~375 nm. The second is a SE (**ii**) signal spanning from ~425 - 550 nm. Finally, a broad absorption (**iii**) is present in the region of ~550 – 675 nm. The feature **i**, is attributed to absorption from the initially populated S_1 state, the feature **ii** also comes from the S_1 state *via* SE to the ground state. As these features evolve, they both experience a slight spectral shift, although the direction and extent is dependent on the pH. Both **i** and **ii** decay concomitantly and as this occurs, a negative-going signal, which we attribute to the ground state bleach (GSB), at the blue edge of the spectra and an absorption peak at ~360 nm are uncovered. These two features, along with **iii**, persist out to the maximum experimental time delay of 500 ps, as shown in Figure 4.5. We return to discuss these long-lived features in the TAS later in this chapter.

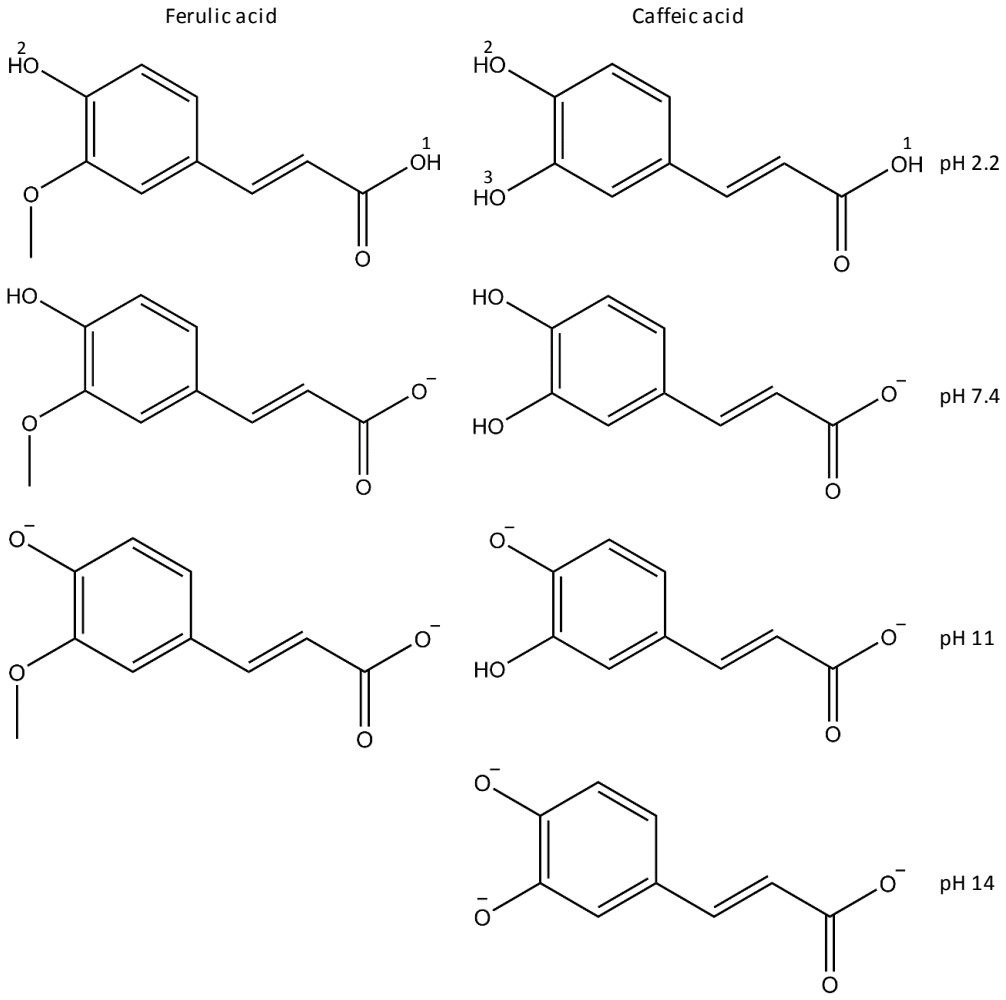

Figure 4.3 The level of protonation of the O–H groups of ferulic and caffeic acid at pHs 2.2, 7.4, 11 and 14.

To further our grasp of the environmental effects, we also performed TEAS upon ferulic and caffeic acids in acetonitrile a polar aprotic environment (ε_r = 37.5).[27] These TAS, presented in Figure 4.4, appear very similar to those acquired in aqueous solution, possessing both the features **i** and **ii**, though **iii** is now absent. Although not immediately evident, a difference exists at early times (<200 fs) however, the TAS displaying a large absorption peak at ~395 nm. This peak rapidly decays and corresponds to the appearance of **i**, at ~365 nm, and **ii** ranging from 425 – 500 nm. A broad absorption is also present akin to **iii**, however, in acetonitrile this absorption decays away with **i** and **ii**. We therefore attribute this signal to the S_1 ESA. At the limit of our time delay (Δt), a number of additional differences in the TAS compared to the aqueous measurements are also seen (Figure 4. 5). Firstly, the GSB appears to be stronger. Secondly no broad sloped absorption in the red-end of the spectrum is seen. Finally, a broad flat absorption is seen between 450 – 600 nm. Like the aqueous measurements, the origins of these features

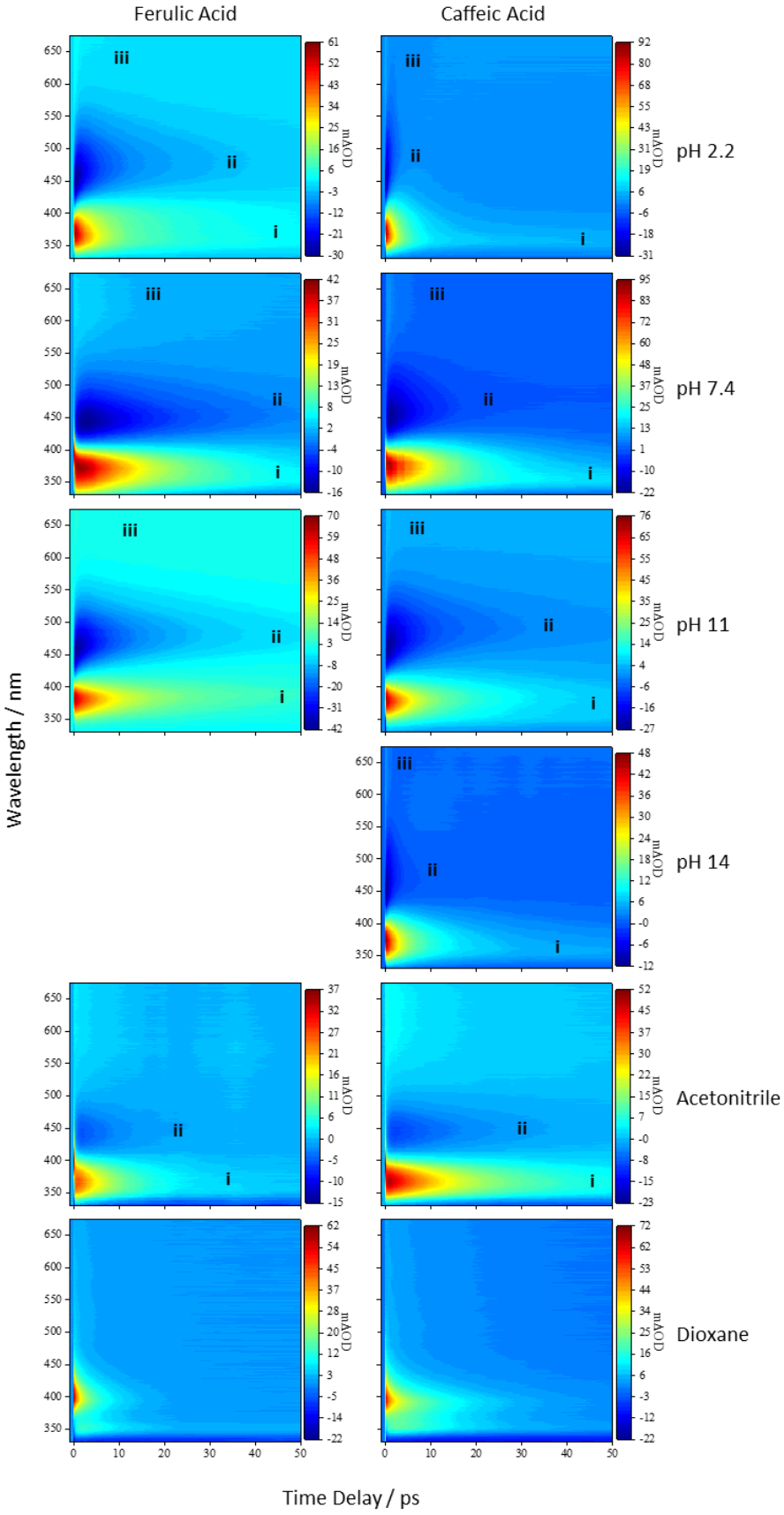

Figure 4.4 TAS of ferulic and caffeic acids at pH 2.2, pH 7.4, pH 11, pH 14, and acetonitrile, and dioxane. The label **i** designates the large ESA, **ii** signifies the SE and finally **iii** shows the absorption of the solvated electron.

are discussed below.

Finally, both ferulic and caffeic acid were studied in dioxane due to its low polarity (ε_r = 2.3).[28] The TAS for ferulic and caffeic acids, shown in the lowest panels in Figures 4.4, display a notable difference to the corresponding TAS in an aqueous environment and acetonitrile; the features **i**, **ii** and **iii** are either very different or absent. Conversely, as with acetonitrile, an initial large absorption is present at ~400 nm, though unlike acetonitrile, this does not swiftly decay away to reveal a second absorption peak. Instead it decays over the course of picoseconds and as it decays, a smaller shoulder grows in at around 355 nm. The large absorption finally returns to the baseline leaving the shoulder peak that has spectrally narrowed and also undergone a small spectral blue-shift, centred ~350 nm. This shoulder persists out to the maximum time delay of our

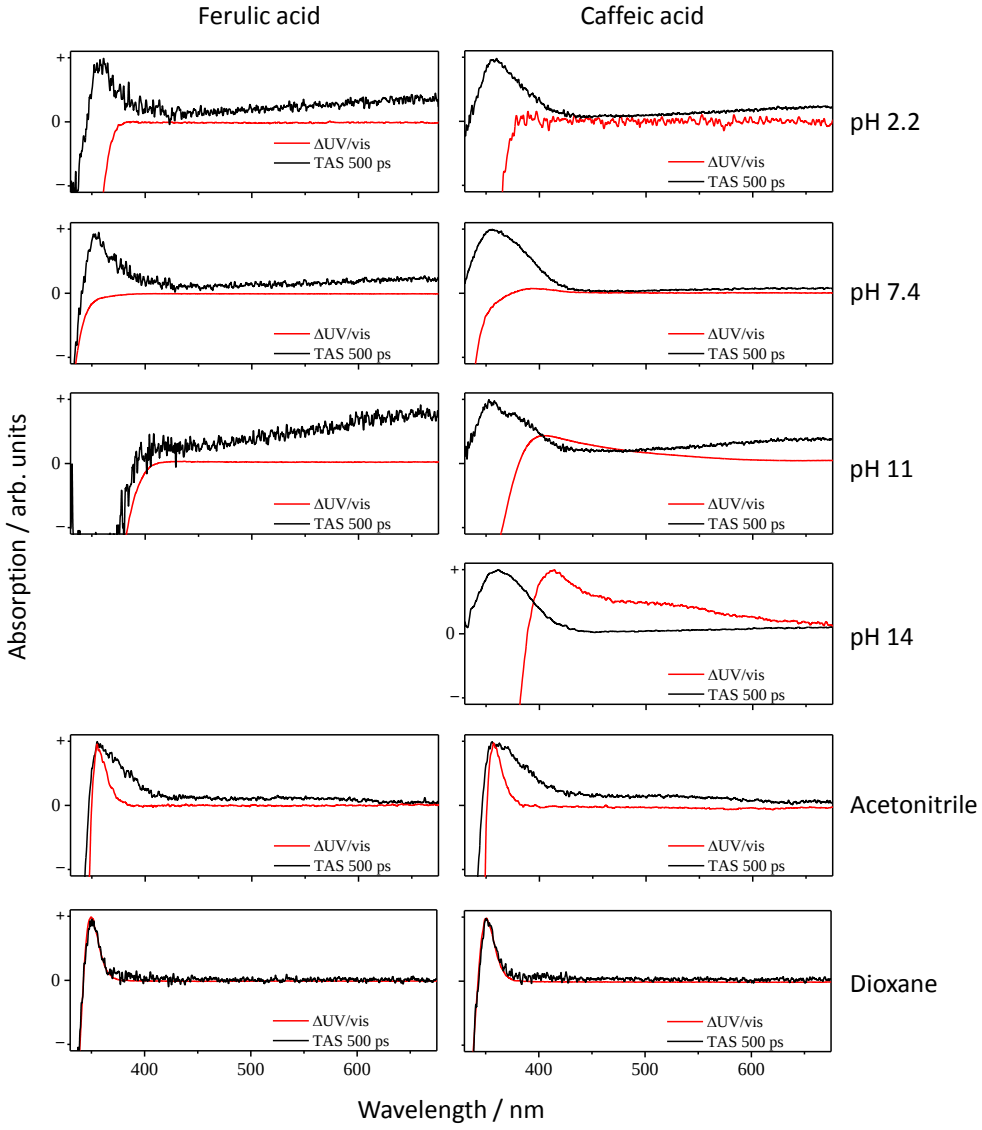

Figure 4.5 Comparison between the TAS spectra at a $\Delta t = 500$ ps and the ΔUV/vis spectra.

Table 4.2 Time constants (τ) for ferulic acid and caffeic acid in varying solvent environments. Values are determined from global analysis of the TAS, with the errors calculated using asymptotic standard errors (see Figure 4.8 and 4.9 and Chapter 2 for details). The errors represent the 95% (2σ) confidence interval.

		τ_1 / fs	τ_2 / ps	τ_3 / ps
FERULIC ACID	pH 2.2	406 ± 32	2.60 ± 0.19	15.4 ± 0.9
	pH 7.4	275 ± 29	1.13 ± 0.11	17.8 ± 0.5
	pH 11	527 ± 36	4.89 ± 0.33	23.5 ± 1.3
	Acetonitrile	47^{+6}_{-2}	0.45 ± 0.04	8.9 ± 0.3
	Dioxane	68^{+79}_{-2}	0.97 ± 0.13	6.3 ± 0.4
CAFFEIC ACID	pH 2.2	279 ± 58	1.05 ± 0.13	4.8 ± 0.4
	pH 7.4	401 ± 76	5.65 ± 1.63	14.6 ± 2.0
	pH 11	286 ± 33	2.90 ± 0.37	15.0 ± 1.2
	pH 14	328 ± 46	1.13 ± 0.11	8.3 ± 0.5
	Acetonitrile	78 ± 6	0.52 ± 0.04	16.7 ± 0.5
	Dioxane	88^{+93}_{-4}	1.15 ± 0.12	14.1 ± 0.7

measurements, and is shown in Figure 4.5. The cause of this feature is also revisited and discussed in detail below.

4.3.2 Global Fitting

In order to recover dynamical information from the TAS, a global fitting technique (see Chapter 2 for further details) using the sum of 5 exponentials, is used. One of the exponentials represents the instrument response, which includes signal attributed to the solvent- and glass-only dynamics (<40 fs). The second exponential represents a baseline offset, which we attribute to long-lived species generated following photoexcitation (*vide infra*). This persists beyond the temporal window of our measurements (>500 ps). The remaining three exponentials are used to recover the time constants of the observed dynamics in ferulic and caffeic acids and are labelled as τ_1, τ_2 and τ_3, as shown in Table 4.2; corresponding decay associated spectra (DAS) are shown in Figure 4.6. The processes these time constants represent are considered in the discussion below guided closely by the recent *ab initio* calculations on ferulic and caffeic acid.[22] The residuals of these fits are shown in Figure 4.7, to highlight the effectiveness of the global fit to reproduce the collected TAS. Furthermore, the accuracy of the recovered time constants to 2σ (95%) was obtained using an asymptotic standard error analysis that is described in Chapter 2, the resultant graphs of which are also shown for completeness in Figures 4.8 and 4.9 for ferulic acid and caffeic acid respectively.

4.3.3 ΔUV/vis Spectra

The *trans*- and *cis*-isomers have been shown to exhibit different ground state UV-vis absorption spectra.[18] We can therefore use this difference to determine if the *cis*-isomer is present in appreciable quantity in the TAS. We performed steady state UV-vis spectroscopy, before and after irradiation with 319 nm and 314 nm radiation for ferulic and caffeic acids respectively. Subtraction of the UV-vis absorption spectra before irradiation from the UV-vis absorption spectra after irradiation results in the ΔUV/vis spectra, and are shown in Figures 4.5, along with the TAS retrieved at the maximum experimental time delay, 500 ps, for comparison.

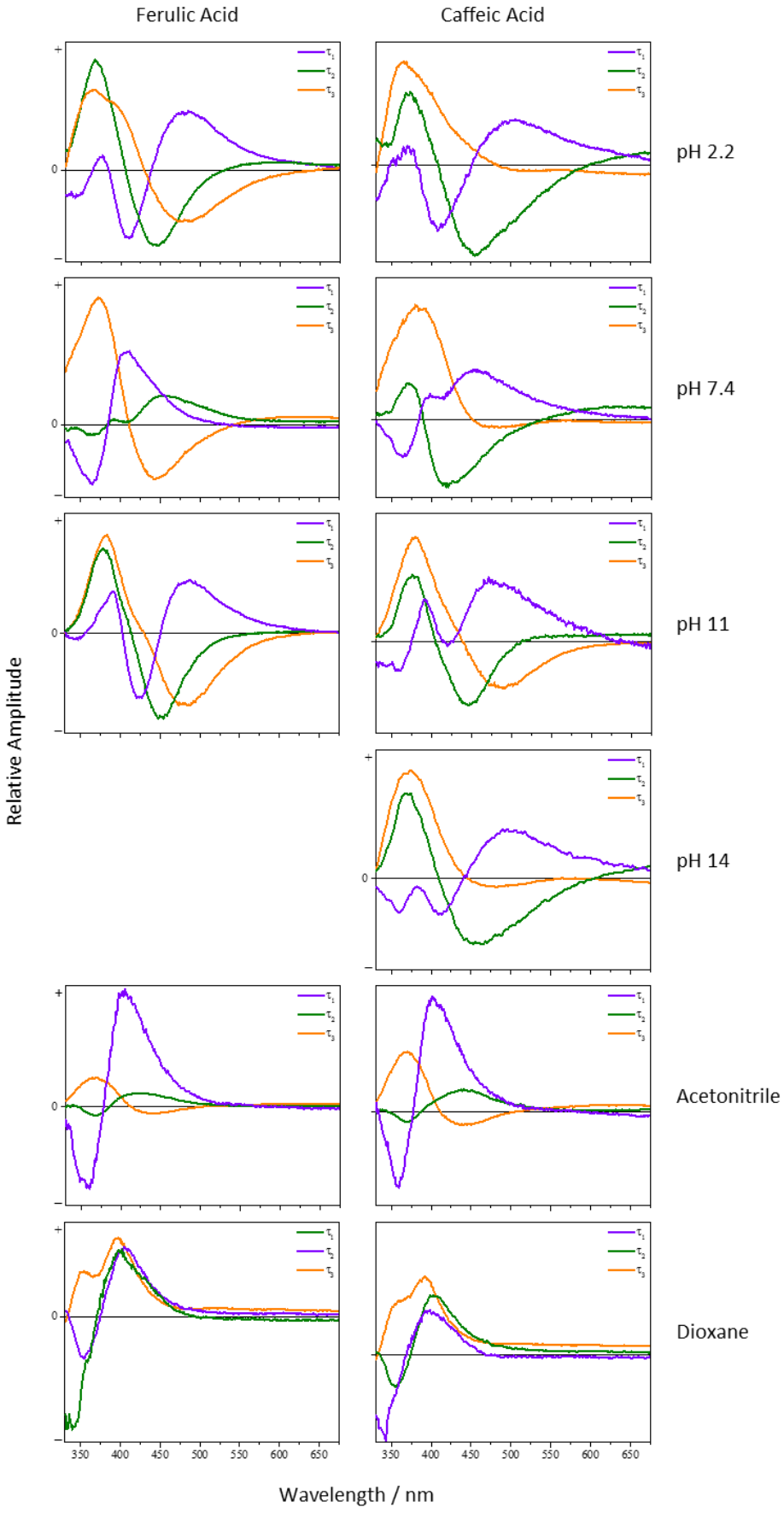

Figure 4.6 The DAS of ferulic and caffeic acids in water pH 2.2, pH 7.4, pH 11, pH 14, acetonitrile and dioxane.

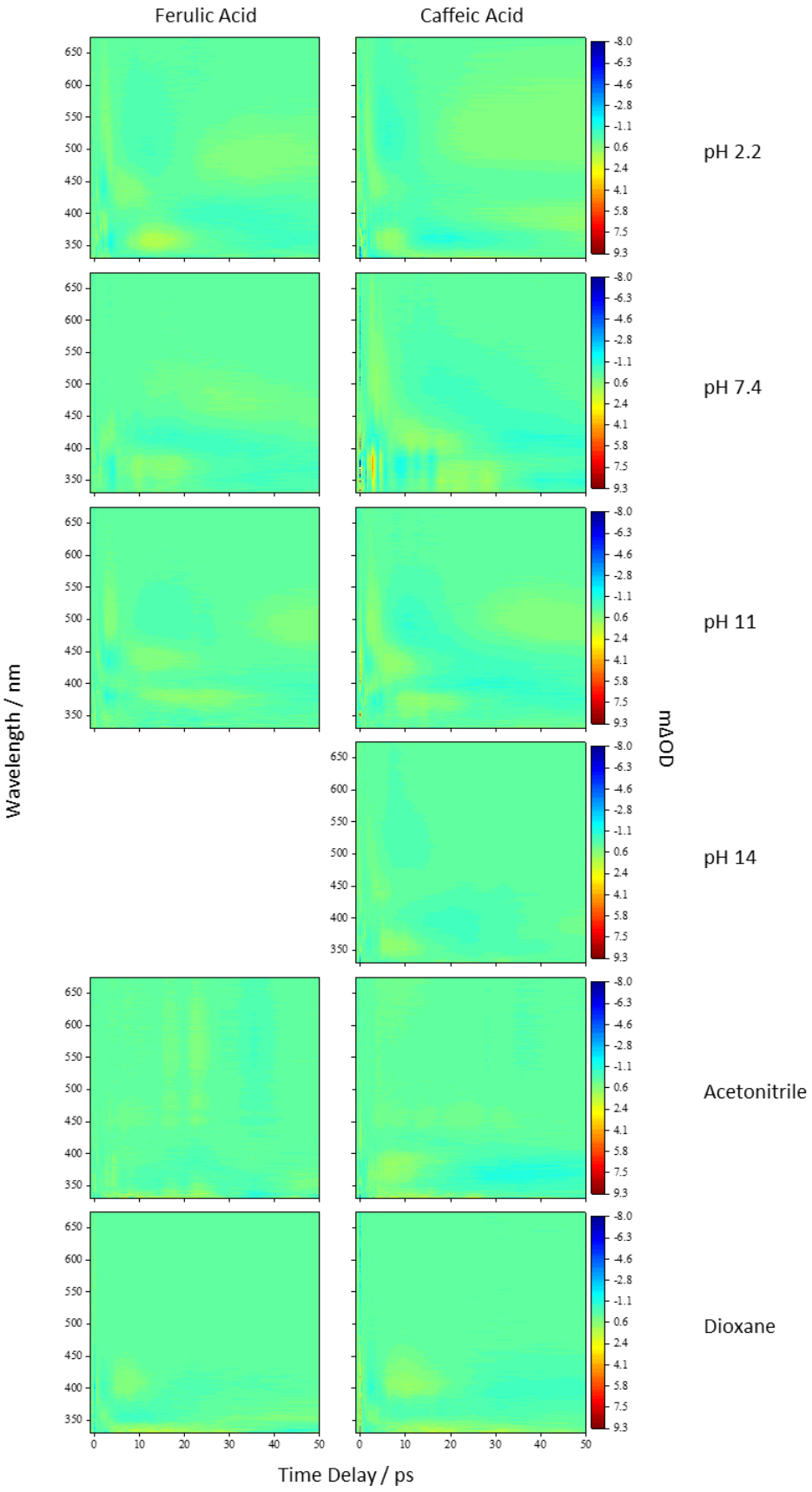

Figure 4.7 Global fit residuals demonstrating the effectiveness in the reproduction of the collected TAS data for ferulic and caffeic acids in water pH 2.2, pH 7.4, pH 11, pH 14, acetonitrile and dioxane.

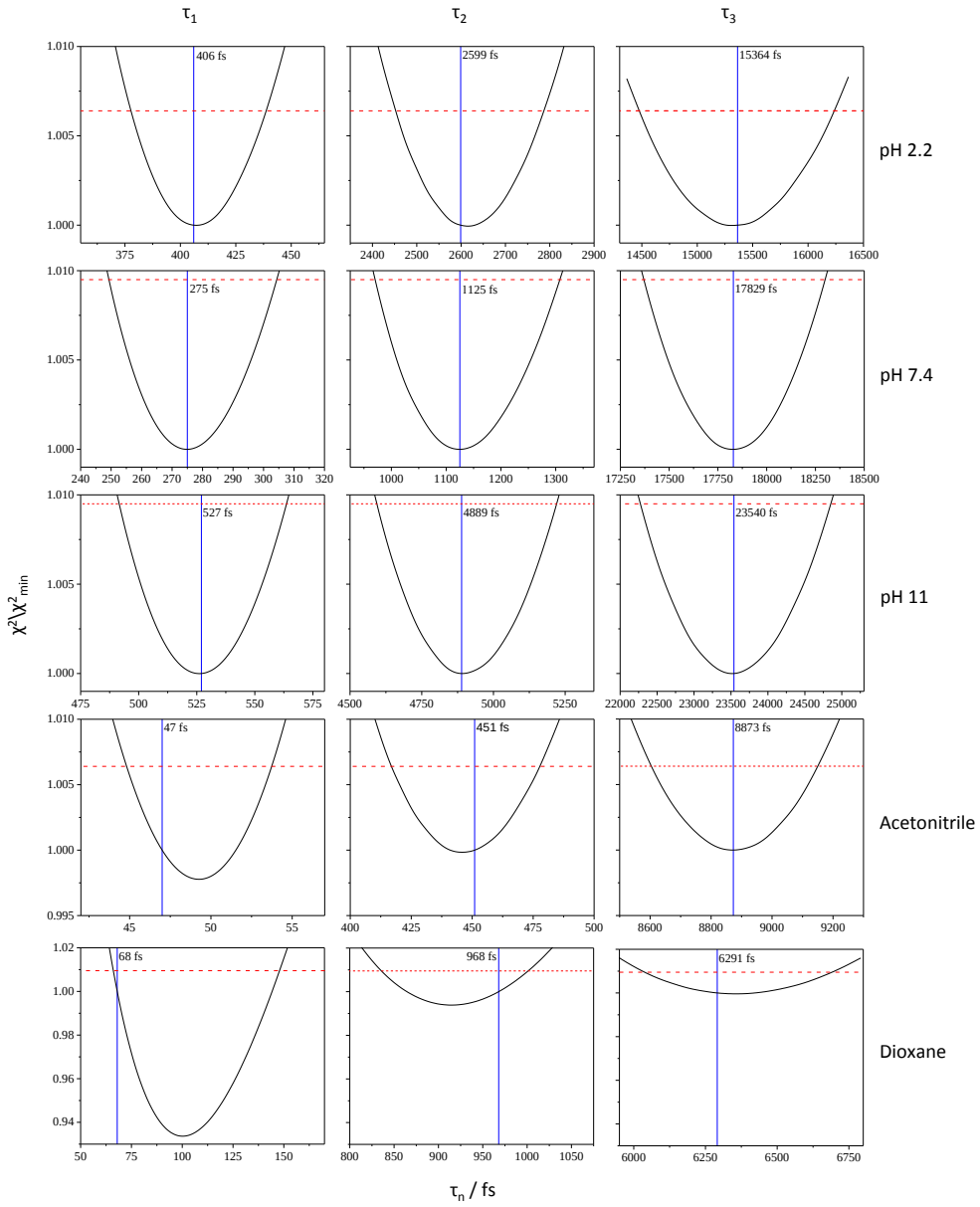

Figure 4.8 Plots of the goodness of fit for ferulic acid produced *via* asymptotic standard error analysis, the time constants τ_1 (left), τ_2 (middle) and τ_3 (right) are shown. The 95% confidence interval (red line), the value of τ_n (blue line) and χ^2/χ^2_{min} values (black line) are shown.

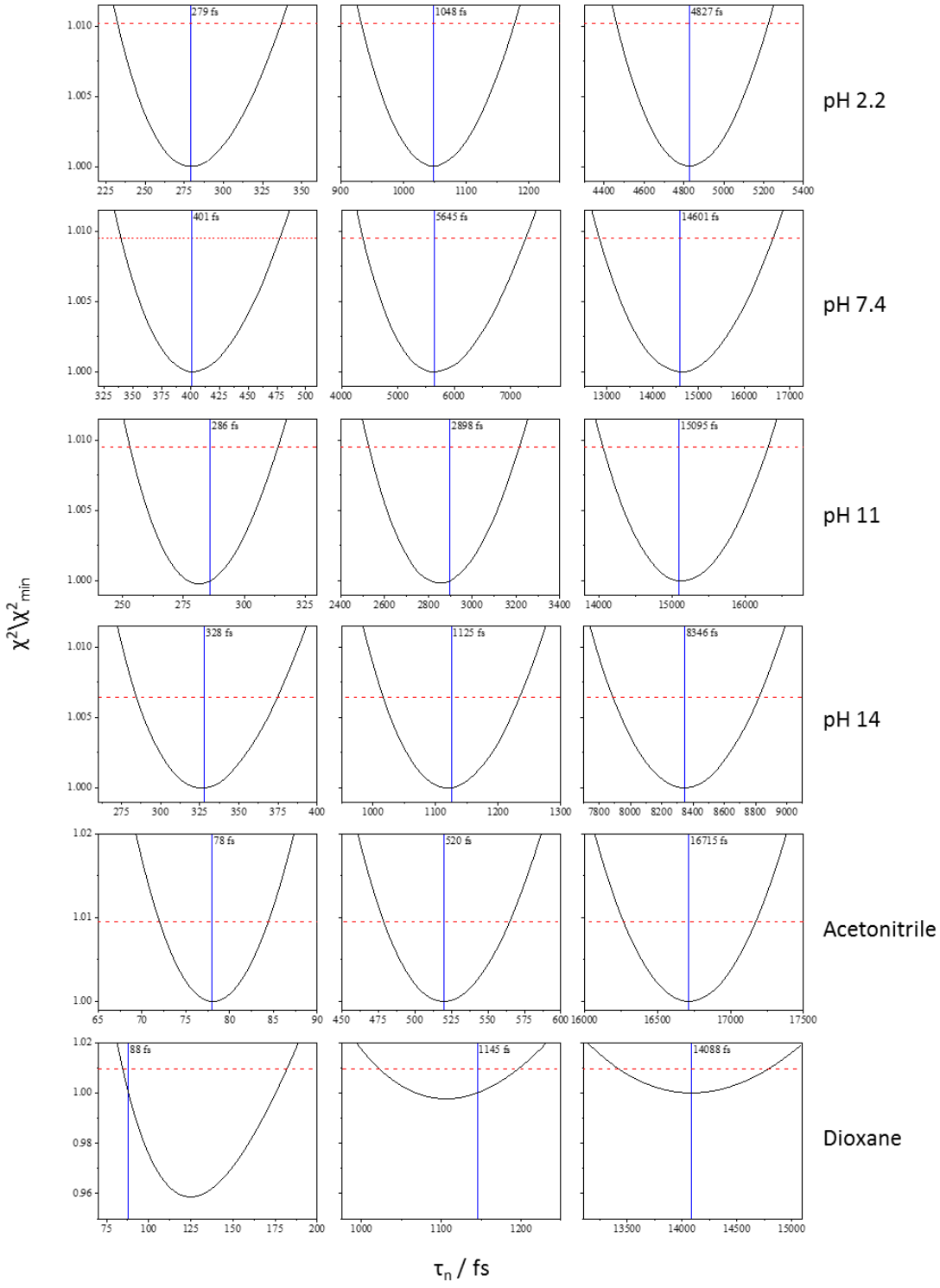

Figure 4.9 Plots of the goodness of fit for caffeic acid produced *via* asymptotic standard error analysis, the time constants τ_1 (left), τ_2 (middle) and τ_3 (right) are shown. The 95% confidence interval (red line), the value of τ_n (blue line) and χ^2/χ^2_{min} values (black line) are shown.

4.4 Discussion

We now discuss the three extracted time constants and the dynamical processes we attribute them to. We reiterate that in the previous study by van Grondelle and co-workers on ferulic acid,[11,17] the authors used two time constants at pH 7 to sufficiently model their transient data at similar excitation wavelengths (318 nm here *versus* their 319 nm); here two time constants were insufficient to fully model our TAS (including our pH 7.4, see ESI) which is likely due to the enhanced time-resolution of the present measurements. This, we believe, has enabled us to effectively separate the first time constant into two components (τ_1 and τ_2) leaving the third time constant (τ_3) in excellent agreement with van Grondelle and co-workers measurements. Considering τ_1, we attribute this time constant to the population flux from the vFC region, induced by a geometry relaxation, as well as any solvent reorientation, lowering the energy of the initially excited S_1 state. This is in agreement with previous ultrafast studies where similar changes to the features occurred within this timeframe.[11,17] We also recognise that with acetonitrile and dioxane, the values of τ_1 are similar to the instrument response and time-zero artefacts, which will undoubtedly contribute to this time constant.

As the TAS evolve over time, the initial features undergo a spectral shift or new absorption peaks emerge. These are attributed to the depopulation of the S_1 state and population of a second electronically excited state. Recent *ab initio* calculations determined that a photoisomerization pathway exists in ferulic and caffeic acids, which occurs on another electronically excited state than the S_1 state. The state that was

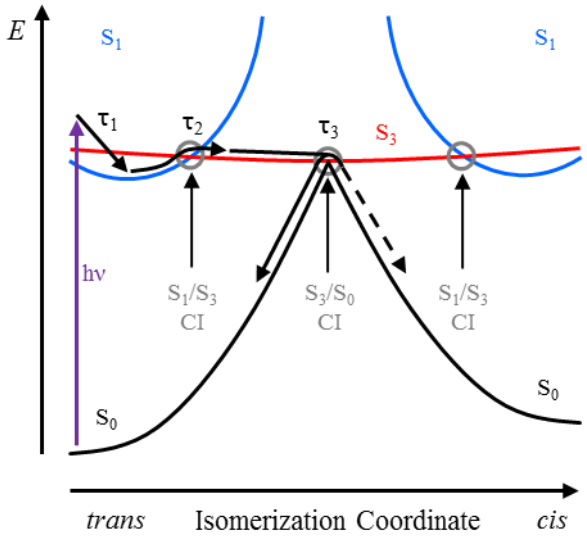

Figure 4.10 A representative schematic of the proposed relaxation pathway, based upon previously calculated potential energy surfaces along the *trans-cis* isomerization coordinate.[22] The S_2 has been omitted for visual simplicity.

identified to mediate this isomerization was the S_3 state.[22] Figure 4.10 shows a schematic of the relevant potential energy cuts (PECs) along the isomerization coordinate and the relaxation mechanism we begin to outline. The spectral displacement in the ESA, and SE seen in the aqueous solutions and acetonitrile, could be due to population of the S_3 excited state, following a nonadiabatic transition via an S_1/S_3 CI. It should be expected then, that following the relaxation of the S_1 on the timescale, τ_1, we would see a second time constant arising from evolution out of it. We believe that τ_2 mainly represents the flux through this S_1/S_3 CI, but due to the global fitting method, it will also capture some of the early relaxation processes assigned to τ_1 along with the initial evolution along the S_3 surface. One caveat is in order here: these calculations[22] suggest that this pathway is ~8,500 cm^{-1} above the photoexcitation wavelengths used in the present experiments. Therefore, it is possible that instead of τ_2 arising due to a S_1 to S_3 state crossing, it is a progression along the initially populated S_1 state. Yet, if this were the case, we would anticipate the spectral features to undergo minor changes, while in the TAS obtained, significant spectral shifts are seen and in some case absorption peaks decay while others grow in. Additionally, these *ab initio* calculations are conducted for a gas-phase environment. It is feasible that when in the presence of solvent, the S_1 to S_3 state crossing pathway becomes energetically accessible as suggested in other studies of similar molecules.[29]

Once the excited state population ends up on the S_3 state, a second CI becomes of interest which is between the S_3 state and electronic ground state, (S_3/S_0). This CI lies along the isomerization coordinate between *trans*- and *cis*-isomers.[22] Therefore, upon reaching the CI, excited state flux is able to progress onto either the *trans* or *cis* ground state such that the quantum yield for photoisomerization (through this pathway alone) is nonzero, as illustrated in the schematic of Figure 4.10. The decay of absorption features, **i** and **ii** in the TAS, and in the aqueous solutions and acetonitrile the decay of SE feature, **ii**, are attributed to the depopulation of the S_3 state through this CI. Since the DAS corresponding to the time constant, τ_3, demonstrate the decay of these absorption (**i** and **iii**) and SE (**ii**) features, we therefore assigned τ_3, to the evolution of excited state flux along the S_3 state and through the S_3/S_0 CI. As with τ_2, we cannot completely rule out that the dynamics are occurring on the S_1 akin to coumaric acid and proceed via a S_1/S_0 CI instead, though one would expect this to require only two time constants to model the dynamics like previous works on PYP.[11,15,17]

It is clear that the solvent environment has an effect upon the values of τ_1, τ_2 and τ_3, yet no trend is apparent which is not unexpected given the highly complex in nature of

these molecules. Indeed, the level of interaction from the solvent will affect the energies of the S_1, S_2 ($1^1n\pi^*$) and S_3 states and this is exemplified in the UV-vis spectra shown in Figure 4.2, at the outset of this chapter. Therefore, it is possible these changes could lead to changes in the state ordering causing the positions of the various CIs and topology of the states along the isomerization coordinates to change. Additionally, it is conceivable that these changes could lead to population being funnelled away from the isomerization coordinate, potentially into the S_2 state (*vide infra*). Indeed, calculations have shown the possibility that the S_2 state crosses both the S_1 and S_3 states.[22]

4.4.1 Photoproducts

After the decay of the S_3 ESA and SE, several features are still present within the TAS and persist out to the longest available time delay, as shown in Figure 4.5. By comparing these features to the ΔUV/vis spectra, we can determine if these features are potentially caused by long-lived photoproducts such as the *cis*-photoproduct; expected from our proposed model. Regarding the 500 ps TAS collected in water, this displays a broad absorption in the red that is indicative to the absorption of the solvated electron.[30] The absorption feature in the blue-end of the spectrum also matches closely to the absorption of a phenolic radical species, which has been seen in other hydroxycinnamic acids.[11,15,17,29] However, as mentioned previously, recent *ab initio* calculations have suggested that the phenolic radical could form through dissociation of the O–H bond *via* a tunnelling mechanism.[22]

Therefore, to determine the origin of the radical in the aqueous solutions, power dependence measurements were performed in water at pH 2.2, the results of which are shown in Figure 4.11. The spectral regions selected for the integration were: (1) a 10 nm wide slice centred at 360 nm which corresponds to the absorption maximum; and (2) a 10 nm slice centred at 670 nm which is within the region the solvated electron absorbs. These measurements show a near quadratic dependence upon pump fluence, which is indicative of two-photon absorption. Therefore, we can confidently assign the origins of the radical and solvated electron absorption to a stepwise two-photon ionization involving the following steps, $S_0 \rightarrow S_1 \rightarrow$ionization, as seen in other related studies.[11,15,17] We note that two-photon ionization is unlikely to occur from exposure to solar UV, or the irradiation used in collecting the ΔUV/vis spectra, and is therefore an unfortunate artefact of the experimental setup due to the high photon fluxes of fs lasers. Unfortunately, the presence of this two-photon driven process, in the TAS, means that it will mask any other transient species which has a spectral signature in this region, including the *cis*-isomer. It is worth mentioning however, in the ΔUV/vis spectra of

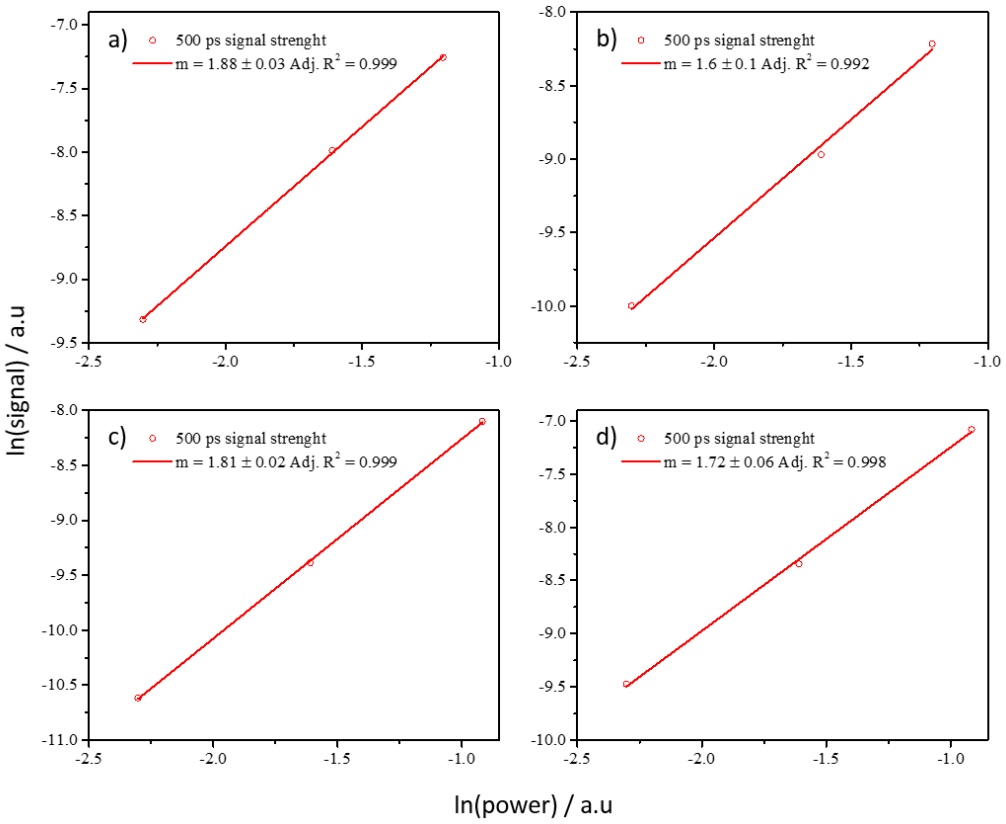

Figure 4.11 Power dependence of the absorption peak at 360 nm and 670 nm in ferulic acid a) and b) respectively, and caffeic acid c) and d) respectively.

caffeic acid at pH 11 and 14, that the absorption appears to undergo a significant red-shift moving it out of the radical's absorption region. Whether this is due to a large spectral-shift in the *cis*-isomer's absorption or the appearance of a new photoproduct is unknown; yet it is absent within the TAS. While the radical absorption masks any potential *cis*-isomer absorption within the TAS, excluding caffeic acid at pH 11 and 14, previous studies have observed the formation of the *cis*-isomer after UV exposure[18-21] and evidence for the *cis*-isomer features being present in our ΔUV/vis spectra. Therefore, we believe that the *cis*-isomer is being formed within our experiments, but it is forming with a quantum yield too low to be detected within our measurements and is shrouded by the non-linear processes.

In the case of acetonitrile as the solvent, the absorption peak in the TAS shown in Figure 4.5 overlays well with the peak in the ΔUV/vis spectrum for both ferulic and caffeic acids. However, a discrepancy between the two is still present, making it tentative to determine whether the *cis*-isomer is actually being formed. The peak in the ΔUV/vis spectrum is significantly narrower than the absorption peak in the TAS which also possesses a long, sloped shoulder in the red end of the absorption. Furthermore the broadness of this peak is akin to that of the phenolic radical for both ferulic and caffeic acid.[31] In order to determine if this feature is the radical absorption, formed through two-

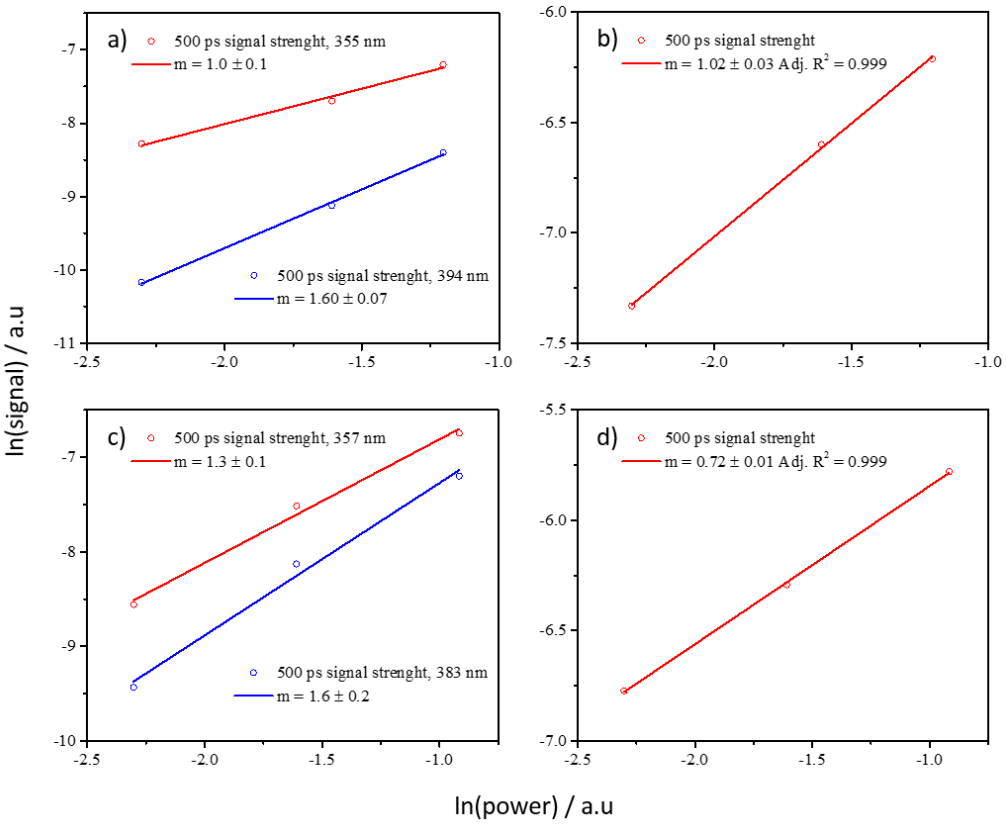

Figure 4.12 Power dependence of a) ferulic acid in acetonitrile at 355 nm (red line) and 394 nm (blue line), b) ferulic acid in dioxane at 360 nm, c) caffeic acid in acetonitrile at 357 nm (red line) and 383 nm (blue line), and d) caffeic acid in dioxane at 360 nm.

photon ionization analogous to the aqueous solutions, we once again performed power dependence measurements, the results of which are presented in Figure 4.12. These measurements demonstrate that different spectral regions in the TAS display differing dependences upon pump power. Integrating the signal at the peak of the absorption in the ΔUV/vis spectrum ferulic acid, shows a linear dependence, while caffeic acid is near-linear. It is worth noting that the peak maximum in the ΔUV/vis spectrum is at the same wavelength as the peak maximum in the TAS. Yet when we integrate signal where no absorption is present in the ΔUV/vis spectrum, both ferulic and caffeic acid display a power dependence of ~1.6. Therefore, we propose that the long-lived absorption is a convolution between the phenolic radical generated by two-photon ionization, akin to the aqueous measurements (*vide supra*), and the absorption from the *cis*-isomer photoproduct.

We close by discussing the data obtained in dioxane, given in Figure 4.5. Firstly, we note that there is a lack of SE in the TAS unlike water and acetonitrile. We believe this is caused by either a spectral shift in the emission causing it to be masked by the ESA, or the probability of emission is too low and again becomes masked by the ESA. Regarding the photoproduct, we see excellent agreement between the 500 ps TAS and ΔUV/vis

spectrum, providing strong evidence that in dioxane, the *cis*-isomer is being formed. Adding to this, the power dependency measurements show that this peak has a linear dependence on power for ferulic acid, while it has a near-linear dependence for caffeic acid. Furthermore, if this peak was indeed caused by the radical absorption it would be absent in the ΔUV/vis spectrum as the radical is unexpected to be present in solution on a second to a minute timescale. This observation of the *cis*-isomer is in contrast to the work of van Grondelle and co-workers[17] where no *cis*-isomer is seen. However, their measurements are *only* performed in water at pH 7.4 and 10.5 and, as with our measurements presented, struggle with convolution with the large radical absorption feature.

It is worth mentioning as a closing statement here that while we have determined if the *cis*-isomer is present or not, we are unable to determine the extent to which it is being formed. Therefore, it is apparent that further studies are needed that are more sensitive to the structural differences between the two isomers. Measurements deploying time-resolved vibrational spectroscopy would certainly be warranted and will be discussed in the final chapter under the outlook section.

4.5 Conclusion

The S_1 excited state relaxation dynamics following UV photoexcitation of both ferulic and caffeic acids, have been studied in a range of solvent environments using transient electronic absorption spectroscopy. The relaxation mechanism proposed, is based closely on the recent theory on these two systems, and involves a geometry rearrangement out of the initial Franck-Condon region with the time constant τ_1. This is then followed by an internal conversion from the S_1 to the S_3 state, *via* an S_1/S_3 conical intersection, assigned the time constant τ_2. Once on the S_3 state, the excited state flux progresses towards an S_3/S_0 conical intersection, induced by an isomerization motion in the "tail" of the acids, leading to either the reformation of the *trans*-ground state or a *cis*-photoproduct on the timescale τ_3.

Finally, we return to briefly assess the sunscreening capabilities of ferulic and caffeic acids, in light of the present findings. Both display a photostability induced by the molecules' ability to quickly deactivate the excess electronic energy via a very likely isomerization pathway, leading to the reformation of the initial ground state or the *cis*-isomer. It is expected that the *cis*-isomer will display a similar excited state relaxation pathway, providing comparable levels of photoprotection as the *trans*-isomer, though further studies are needed to confirm this.

4.6 Bibliography

1. N. Serpone, A. Salinaro, A. V. Emeline, S. Horikoshi, H. Hidaka and J. Zhao, *Photochem. Photobiol. Sci.*, 2002, **1**, 970-981.
2. S. Afonso, K. Horita, J. P. S. e Silva, I. F. Almeida, M. H. Amaral, P. A. Lobão, P. C. Costa, M. S. Miranda, J. C. G. E. da Silva and J. M. S. Lobo, *J. Photochem. Photobiol. B*, 2014, **140**, 36-40.
3. M. S. Matsui, A. Hsia, J. D. Miller, K. Hanneman, H. Scull, K. D. Cooper and E. Baron, *J. Investig. Dermatol. Symp. Proc*, 2009, **14**, 56-59.
4. A. Saija, A. Tomaino, D. Trombetta, A. De Pasquale, N. Uccella, T. Barbuzzi, D. Paolino and F. Bonina, *Int. J. Pharm.*, 2000, **199**, 39-47.
5. H. Kikuzaki, M. Hisamoto, K. Hirose, K. Akiyama and H. Taniguchi, *J. Agric. Food Chem.*, 2002, **50**, 2161-2168.
6. K. Sevgi, B. Tepe and C. Sarikurkcu, *Food Chem. Toxicol.*, 2015, **77**, 12-21.
7. F.-H. Lin, J.-Y. Lin, R. D. Gupta, J. A. Tournas, J. A. Burch, M. A. Selim, N. A. Monteiro-Riviere, J. M. Grichnik, J. Zielinski and S. R. Pinnell, *J. Invest. Dermatol.*, 2005, **125**, 826-832.
8. J. C. Murray, J. A. Burch, R. D. Streilein, M. A. Iannacchione, R. P. Hall and S. R. Pinnell, *J. Am. Acad. Dermatol.*, 2008, **59**, 418-425.
9. A. Espagne, D. H. Paik, P. Changenet-Barret, M. M. Martin and A. H. Zewail, *ChemPhysChem*, 2006, **7**, 1717-1726.
10. N. Mataga, H. Chosrowjan, S. Taniguchi, N. Hamada, F. Tokunaga, Y. Imamoto and M. Kataoka, *Phys. Chem. Chem. Phys.*, 2003, **5**, 2454-2460.
11. H. Kuramochi, S. Takeuchi and T. Tahara, *J. Phys. Chem. Lett.*, 2012, **3**, 2025-2029.
12. K. Heyne, O. F. Mohammed, A. Usman, J. Dreyer, E. T. J. Nibbering and M. A. Cusanovich, *J. Am. Chem. Soc.*, 2005, **127**, 18100-18106.
13. A. Espagne, P. Changenet-Barret, P. Plaza and M. M. Martin, *J. Phys. Chem. A*, 2006, **110**, 3393-3404.
14. G. Groenhof, M. Bouxin-Cademartory, B. Hess, S. P. De Visser, H. J. C. Berendsen, M. Olivucci, A. E. Mark and M. A. Robb, *J. Am. Chem. Soc.*, 2004, **126**, 4228-4233.
15. D. S. Larsen, I. H. M. van Stokkum, M. Vengris, M. A. van der Horst, F. L. de Weerd, K. J. Hellingwerf and R. van Grondelle, *Biophys. J.*, 2004, **87**, 1858-1872.
16. P. Changenet-Barret, A. Espagne, S. Charier, J.-B. Baudin, L. Jullien, P. Plaza, K. J. Hellingwerf and M. M. Martin, *Photochem. Photobiol. Sci.*, 2004, **3**, 823-829.
17. M. Vengris, D. S. Larsen, M. A. van der Horst, O. F. A. Larsen, K. J. Hellingwerf and R. van Grondelle, *J. Phys. Chem. B*, 2005, **109**, 4197-4208.
18. J. S. Challice and A. H. Williams, *J. Chromatogr. A*, 1966, **21**, 357-362.

19. R. D. Hartley and E. C. Jones, *J. Chromatogr. A*, 1975, **107**, 213-218.
20. T. W. Fenton, M. M. Mueller and D. R. Clandinin, *J. Chromatogr. A*, 1978, **152**, 517-522.
21. G. Kahnt, *Phytochemistry*, 1967, **6**, 755-758.
22. T. N. V. Karsili, B. Marchetti, M. N. R. Ashfold and W. Domcke, *J. Phys. Chem. A*, 2014, **118**, 11999-12010.
23. S. E. Greenough, M. D. Horbury, J. O. F. Thompson, G. M. Roberts, T. N. V. Karsili, B. Marchetti, D. Townsend and V. G. Stavros, *Phys. Chem. Chem. Phys.*, 2014, **16**, 16187-16195.
24. M. D. Horbury, L. A. Baker, W.-D. Quan, J. D. Young, M. Staniforth, S. E. Greenough and V. G. Stavros, *J. Phys. Chem. A*, 2015, **119**, 11989-11996.
25. F. Borges, J. L. Lima, I. Pinto, S. Reis and C. Siquet, *Helv. Chim. Acta*, 2003, **86**, 3081-3087.
26. K. Hasselbalch, *Biochem Z*, 1916, **78**, 112-144.
27. J.-F. Côté, D. Brouillette, J. E. Desnoyers, J.-F. Rouleau, J.-M. St-Arnaud and G. Perron, *J. Solution Chem.*, 1996, **25**, 1163-1173.
28. G. Åkerlöf and O. A. Short, *J. Am. Chem. Soc.*, 1936, **58**, 1241-1243.
29. L. A. Baker, M. D. Horbury, S. E. Greenough, F. Allais, P. S. Walsh, S. Habershon and V. G. Stavros, *J. Phys. Chem. Lett.*, 2016, **7**, 56-61.
30. J. Peon, G. C. Hess, J.-M. L. Pecourt, T. Yuzawa and B. Kohler, *J. Phys. Chem. A*, 1999, **103**, 2460-2466.
31. S. Foley, S. Navaratnam, D. J. McGarvey, E. J. Land, T. G. Truscott and C. A. Rice-Evans, *Free Radic. Bio. Med.*, 1999, **26**, 1202-1208.

5. Photodynamics of *cis*-$[Ru(bpy)_2(NA)_2]^{2+}$ after Two-Photon Absorption

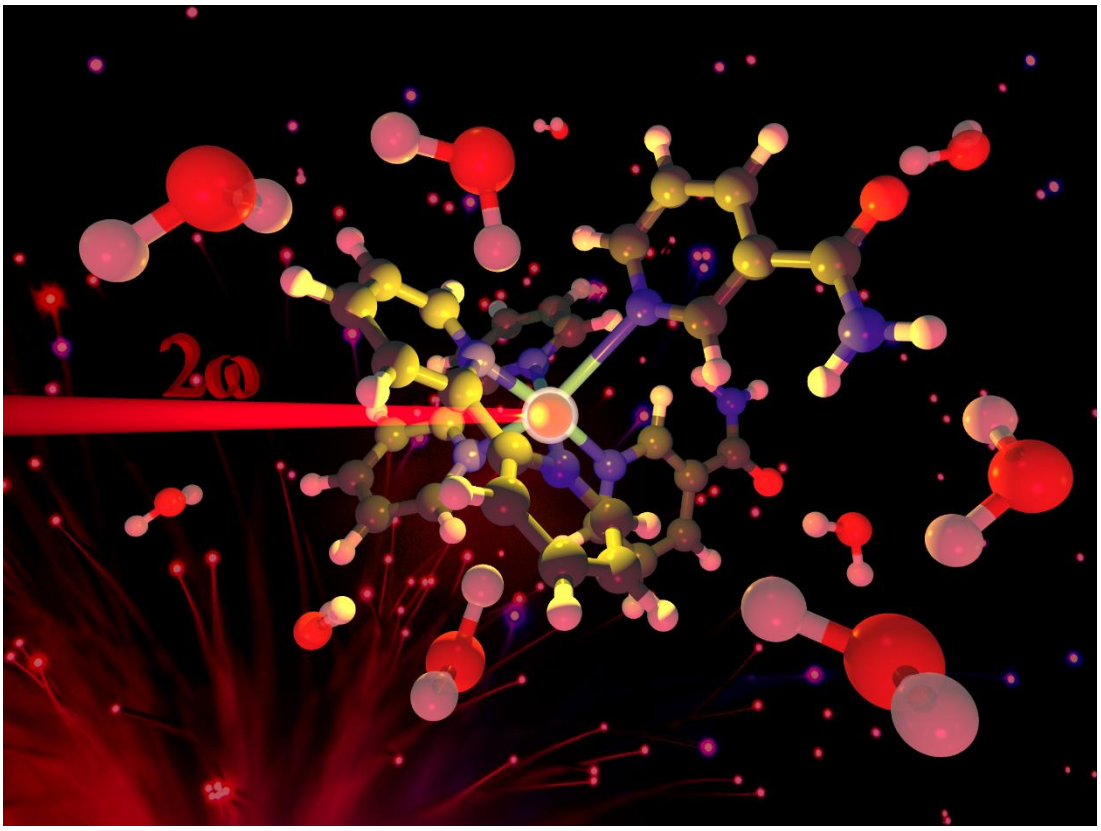

This chapter is based on the following publication:

> S. E. Greenough, M. D. Horbury, N. A. Smith, P. J. Sadler, M. J. Paterson and V.G. Stavros, Excited-State Dynamics of a Two-Photon-Activatable Ruthenium Prodrug, *ChemPhysChem*, 2016, **17**, 221-224

The theory calculations were performed by M. J. Paterson.

The synthesis and characterisation of complex **1** was performed by N. A. Smith and P. J. Sadler

5.1 Introduction

In Chapters 3 and 4 we have explored the photodynamics of relatively photostable molecules linked with the photoprotection of the skin against solar irradiation. However, while these protective measures are highly efficient, they do not always succeed leading to potentially harmful effects such as cancers of the skin.[1-3] Therefore in the chapter, we look at the ruthenium poly-pyridyl complex, *cis*-$[Ru(bpy)_2(NA)_2]^{2+}$ (**1**, shown in Figure 5.1 inset, bpy = 2,2'-bipyridine and NA = nicotinamide, pyridine-3-carboxamide) that has a potential therapeutic role towards these cancers. **1** has been shown to undergo the loss of a ligand after irradiation leading to the formation of the active species.[4] Unfortunately as mentioned in Section 1.7, the human skin has a spectral window between 620 - 1000 nm[5-7] and as can be seen from Figure 5.1 the absorption of this complex starts ~550 nm. However, it is clear that it would be possible to activate the complex *via* two-photon absorption (TPA, Section 1.2.8) within the required spectral window.

Currently, there is an apparent paucity of photodynamical insight following TPA of ruthenium poly-pyridyl complexes. Therefore, in this chapter we aim to investigate the photodynamics of **1** after TPA. The photodynamics after excitation *via* OPA of **1** with UV/visible light, are well established.[4] The initial photoactivation mechanism has been

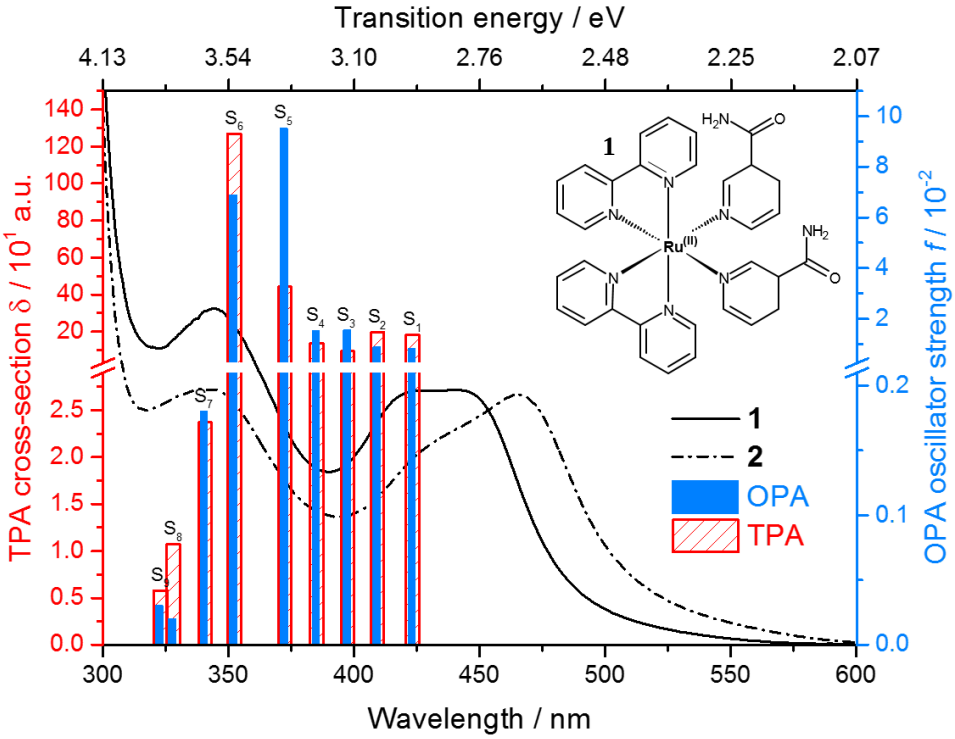

Figure 5.1 Static UV/visible absorption spectra of *cis*-$[Ru(bpy)_2(NA)_2]^{2+}$ (solid line, **1** structure shown) and its mono-aquated form, *cis*-$[Ru(bpy)_2(NA)(H_2O)]^{2+}$ (dashdot line, **2**) formed by irradiation of **1** in water with a blue (465 nm) light source which yields **2**. DFT calculated OPA oscillator strengths, *f* (blue, right axis) and TPA cross-sections, δ (red, left axis) for **1** in the gas phase.

mapped to the formation of the monoaquated species $[Ru(bpy)_2(NA)(H_2O)]^{2+}$ (**2**), whose UV/visible absorption spectrum is shown in Figure 5.1. This transformation occurs on a ps timescale, and is mediated via a pentacoordinate intermediary species $[Ru(bpy)_2(NA)]^{2+}$, PCI).[4] To allow activation of **1** in the photodynamic therapy (PDT) window existing between 620 and 1000 nm,[5-7] we use 800 nm radiation to induce TPA. The work presented in this chapter, addresses whether there are significant differences between the one- and two-photon activation mechanisms of **1**, by tracking the dynamics of photoactivation following TPA. Particularly, it is the role of the excited state deactivation pathways that compete with the formation of **2** that are of interest in this work and whether they differ between OPA and TPA. The main processes of concern are internal conversion of the lowest excited electronic state to the ground state and geminate or caged recombination of the nascent pentacoordinate species and free NA ligand. While the latter is unlikely to be affected between OPA and TPA, the relaxation of excited states following TPA may differ to OPA. The initial populated states are going to differ due to TPA and OPA having different selection rules (Section 1.2.8) that govern absorption. Therefore, the efficiency of the flow into the 'desirable' pathway may be lessened. If the OPA *vs* TPA dynamics are comparable, then TPA drug design may be approached using knowledge garnered from the more numerous and easily conducted OPA studies. As with Chapters 3 and 4, we have used transient electronic (UV/visible) absorption spectroscopy (TEAS) and complementary density functional theory (DFT) calculations to elucidate the excited state dynamics of **1** following TPA.

5.2 Methods

5.2.1 Transient Electronic Absorption Spectroscopy

The details pertaining to the TEAS setup can be found in Chapter 2; the experimental variables specific to this work are described here. The sample consists of 650 μM aqueous sample of **1**, whose synthesis is briefly provided for completeness.[4] NA was purchased from Sigma Aldrich and used as received. $[Ru(bpy)_2Cl_2]$ was prepared following the procedure in the literature.[8] **1**·$(PF_6)_2$, was synthesized in an analogous manner to other ruthenium(II) complexes of the type $[Ru(bpy)_2(L)_2](PF_6)_2$.[9] $[Ru(bpy)_2Cl_2]$ (104 mg, 0.2 mmol) was added to 10 mL degassed water and the solution was heated in the dark at 353 K for 15 min. NA (122 mg, 1 mmol) was added and the solution was heated for a further 2 h. The resulting dark red solution was allowed to cool, and any insoluble material was removed by filtration. NH_4PF_6 (163 mg, 1 mmol) was added to give an orange precipitate. The solution was cooled for 2 h (ca. 277 K) and

filtered under suction. The precipitate was washed with 40 mL cold water and 40 mL diethyl ether. The yield was determined to be 48.5%.

The spacers between the CaF_2 windows were set to 950 μm (maximum available spacer) in order to provide a useable transient absorption signal, due to the low TPA probability. The wavelength of the pump beam was centred on 800 nm (1.55 eV) with a pump fluence of 10 – 20 mJ cm^{-2}. The portion of the while light continuum used for the probe beam spanned 340 – 675 nm.

5.2.2 Computational Details

The ground state geometry of **1** was optimized using DFT and were performed using the Gaussian09 program.[10]

For calculating the TPA transitions strengths, the CAM-B3LYP functional was selected. The calculations were performed using the Dalton2015 program.[11] This has been shown to give accurate TPA transition-strengths relative to highly correlated methods.[12]

5.2.3 Kinetic Analysis and Fitting

The kinetic traces for each of the individual species involved in the photodissociation of **1** were extracted using a target analysis approach. The reader is directed to Chapter 2, Section 2.8.3.2 for further details regarding this approach. Each of these traces were then fit using a single exponential decay as described, as shown by the following equation:

$$F(\Delta t) = g(\Delta t) * Aexp\left(\frac{-\Delta t}{\tau}\right) \quad (5.1)$$

Here τ is the time constant, A is the amplitude of the exponential and $g(\Delta t)$ is the convoluted $(*)$ Gaussian.

5.3 Results and discussion

The recorded transient absorption spectra (TAS) for select pump-probe time delays are shown in Figure 5.2. The initial 5 ps is dominated by dynamics from heating effects in the CaF_2 window. In vein we tried to reduce this instrument-artifact through manipulating pulse intensity, CaF_2 window thickness and increase sample pathlength. Unfortunately, this meant that we were blind to the initial excited state evolution, in contrast to our previous OPA studies (see below). The UV/visible excitation of this class of Ru(II) poly-pyridyl complex (most notably $[Ru(bpy)_3]^{2+}$) has been heavily studied[13] and it is typical for the initial excited singlet metal-to-ligand charge-transfer (^{1}MLCT) state to evolve to a manifold of near degenerate triplet states (^{3}MLCT), mediated by

intersystem crossing, with a near-unity quantum yield.[14-16] Dissociation may then occur via the ^{3}MLCT or a triplet metal-centred (^{3}MC, d-d ligand field) state, if it is of a similar energy as seen in similar systems.[17-19]

5.3.1 Computational Study

To further address the nature of the initially populated excited states, we performed DFT calculations with the CAM-B3LYP functional for both OPA and TPA. This functional has been shown to give accurate TPA transition-strengths relative to highly correlated methods,[12] due to its ability to better describe transitions to and from intermediate states.[20,21] The one- and two-photon intensities of the first nine singlet state transitions are shown in Figure 5.1. Assessment of the optically bright states, shown in Table 5.1, indicates that the dominant contribution of these transitions is of MLCT character, with MC states adding very little to either OPA or TPA intensities. It is worth noting that states that possess large oscillator strength also display large TPA cross-sections which is in contrast to the selections rules described in Sections 1.2.7 and 1.2.8. However, the transitions shown here display mixing of state characteristics. While direct population of the dissociative state may be possible, *i.e.* ^{1}MLCT → ^{3}MC, little evidence is found for such behaviour in the literature.

Table 5.1 Calculated CAM-B3LYP transition energies, oscillator strengths, *f*, and two-photon absorption cross-sections, δ, for the first 11 singlet states of complex **1** in the gas-phase. For dominant (Dom.) contributions H denotes the HOMO and L designates the LUMO.

STATE	Energy / eV	λ / nm	*f*	δ^{TPA}	Character	Dom. Contribution
S_1	2.93	423	0.0080	182.0	MLCT	78% H→ L
S_2	3.03	409	0.0088	196.0	MLCT	77% H → L+1
S_3	3.12	397	0.0154	94.6	MLCT	57% H-1 → L 29% H-1 → L+1
S_4	3.22	385	0.0152	138.0	MLCT	59% H-1 → L+1 23% H-1 → L
S_5	3.33	372	0.0952	442.0	MLCT	86% H-2 → L
S_6	3.52	352	0.0688	1270.0	MLCT	70% H-2 → L+1
S_7	3.64	341	0.0018	23.7	LF	43% H→ L+16
S_8	3.78	328	0.0002	10.7	LF	23% H-2→ L+15
S_9	3.84	323	0.0003	5.8	LF	30% H-1→ L+15
S_{10}	4.17	297	0.0311	812.0	MLCT	44% H → L+3
S_{11}	4.22	294	0.0090	95.3	MLCT	57% H → L+2

5.3.2 Transient Absorption Study

The TAS shown in Figure 5.2 comprises three identifiable regions for Δ*t* of 1 to 100 ps and an additional feature appearing from 200 ps onwards. A strong negative signal is observed, centred on 420 nm (Figure 5.2, **ii**), which we assign to the ground state bleach

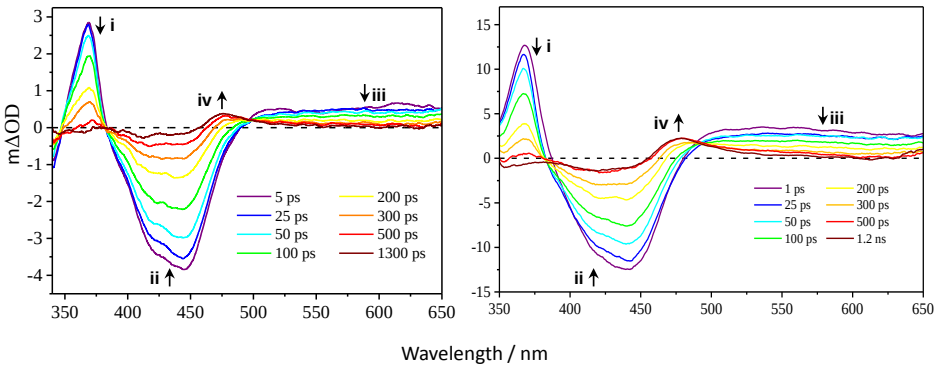

Figure 5.2 Two-photon excitation (800 nm) transient absorption spectra of *cis*-$[Ru(bpy)_2(NA)_2]^{2+}$ in water for select time delays (left). The features seen are very similar to those seen following OPA (right).

(GSB), due to its close resembles the static UV/Vis absorption of **1** (Figure 5.1, solid line). This GSB is narrowed significantly due to the overlapping of positive signals at ~370 and ~475 nm. UV/visible spectroelectrochemistry measurements of $[Ru(bpy)_3]^{2+}$ [22] and related complexes with functionalized bpy derivatives,[23] indicate that the large positive feature at ~370 nm (Figure 5.2, **i**) can be assigned to the excited state absorption (ESA) of a ^{3}MLCT excited state. Specifically to the absorption from the bpy anion (bpy^-) present within the formally charge-separated character of the ^{3}MLCT state *i.e.* $[Ru^{III}(bpy)(bpy^-)(NA)_2]^{2+}$.[24] The broad positive plateau at $\lambda > 550$ nm (Figure 5.2, **iii**) is assigned to a PCI complex, $[Ru(bpy)_2(NA)]^{2+}$, in agreement with its previously calculated gas-phase absorption spectrum.[4,18] Following these features over the first few hundred picoseconds, **ii** recovers back toward zero whilst **i**, and **iii**, concomitantly decay. As mentioned above, beyond 200 ps, there is a new absorption feature centred at 475 nm (Figure 5.2, **iv**) that reaches a maximum after ~500 ps. Due to its resemblance to the static UV/visible absorption spectrum of **2** (Figure 5.1, dash-dot line), this is assigned to formation of photoproduct **2**; from the aquation of the PCI. The photoproduct signal and the corresponding GSB signal remain constant for the remaining probed time delays (up to 2 ns).

5.3.3 Power Dependence

To confirm that absorption present within the TAS is due to TPA, the dependence of the GSB signal (magnitude of GSB signal at 420 nm at Δt = 100 ps) with laser excitation power was determined. The laser excitation powers used were 12, 15, 18, 21 and 24 mW corresponding to excitation fluences of between ~10 and ~20 mJ cm^{-2}. The retrieved GSB signal strength against laser excitation power is shown in a log-log plot in Figure 5.3, as the gradient of a linear fit provides the GSB dependence to laser power. The gradient of the linear fit in Figure 5.3 (red line) has a value of ~2 which is a clear indicator

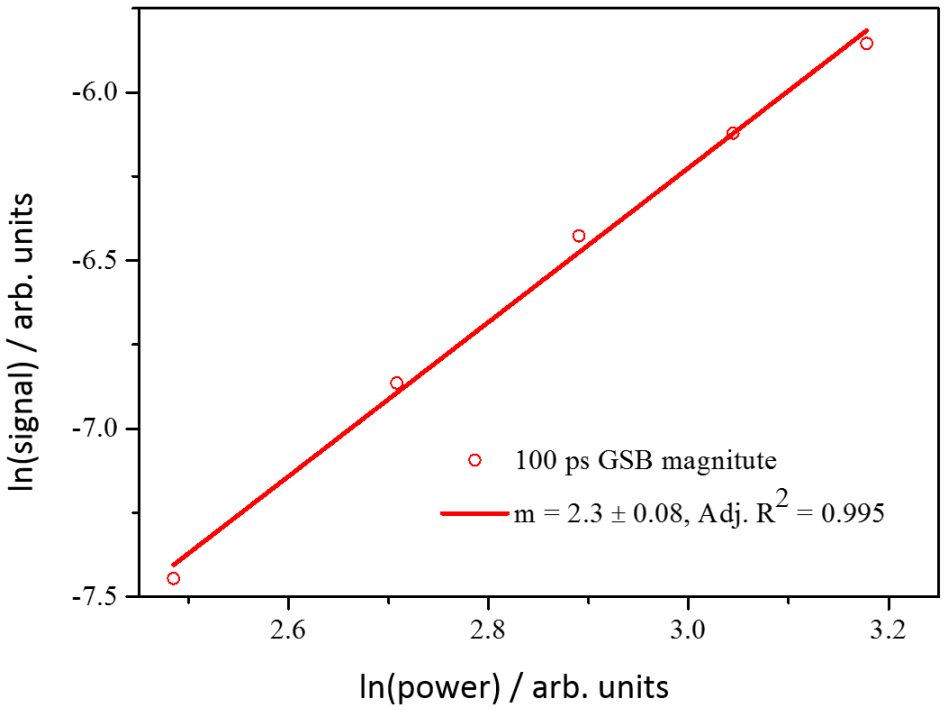

Figure 5.3 Log-log plot of GSB signal at 100 ps against excitation power.

of second order power dependence and hence indicative of TPA. Importantly, we have also tried various other methods to generate such log-log plots (integrating each basis function and integrating several spectral regions) and they all revealed similar slopes. We are therefore confident that the signal present in the TAS, and hence the ensuing dynamical studies presented herein, is primarily (if not solely) driven by TPA.

5.4 Discussion

From this point on we seek to gain insight into the TPA activation mechanism, and identify differences to the OPA activation mechanism, by examining kinetic traces for these key features and the timescales involved. These traces are illustrated in Figures 5.4 and 5.5 for TPA and OPA respectively. Due to the shrouding of early time dynamics by the glass-only signal (see above), a full analysis discovering ultrafast (<5 ps) processes cannot be performed. In our previous OPA study however (excitation at 340 nm),[4] this time-resolution was available, allowing for a detailed 'target analysis' approach to be used in order to extract time constants and quantum yields for the branched kinetics. This analysis and fitting allowed for the formulation of the general photoactivation mechanism, as summarised by Figure 5.6, which we return to discuss in the ensuing paragraphs. In the case of TPA, the 'target analysis' is used to extract the kinetic traces (Figure 5.4) only. In both 'target analysis' of OPA and TPA, the basis functions are derived from known absorption profiles and fitted to the TAS at each value of Δt to extract an integrated signal for each spectral component over time (Section

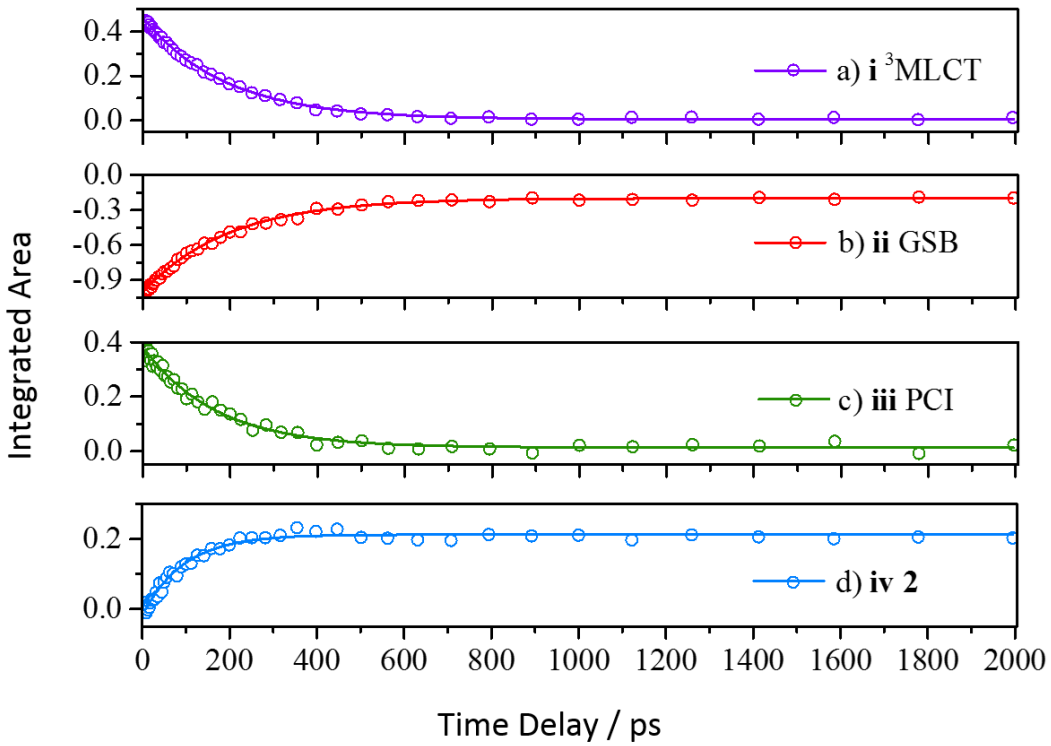

Figure 5.4 Kinetic traces for time-dependent evolution (following excitation with two photons of 800 nm) of a) ^{3}MLCT (**i**) state population, b) GSB (**ii**) recovery, c) PCI (**iii**) population, and d) **2** the photoproduct (**iv**), obtained from integration of basis functions used in the 'target analysis'. The obtained lifetimes are summarized in Table 5.2.

2.8.3.2). The resulting transients are shown in Figure 5.4 and Figure 5.5, for TPA and OPA respectively. The fitting of single exponential decay functions (Equation 5.1) to the TPA kinetic traces yields time constants for the evolution of the ^{3}MLCT, GSB, PCI and **2** recovery, summarised in Table 5.2. It is important to note that for a branched kinetics scheme used previously in our OPA studies (see reference 4), there are competing relaxation pathways for these features, *e.g.* the ^{3}MLCT state, which may convert to either the ground state or ^{3}MC state. Therefore, there are at least two lifetimes contributing to the time constant extracted from a single exponential fits of the TPA kinetic traces. The fits return time constants for the evolution of features **i**, **ii**, **iii** and **iv** shown in Figure 5.4a), b) c) and d), respectively of 188 ± 2 ps for the ^{3}MLCT state, 198 ± 4 ps for the GSB recovery, 167 ± 7 ps for the PCI species and 95 ± 5 ps for the formation of **2**.

Table 5.2 Time constants obtained from the kinetic analysis.

	^{3}MLCT	GSB	PCI	**2**
OPA	183 ± 2 ps	179 ± 3 ps	168 ± 9 ps	151 ± 9 ps
TPA	188 ± 2 ps	198 ± 4 ps	167 ± 7 ps	95 ± 5 ps

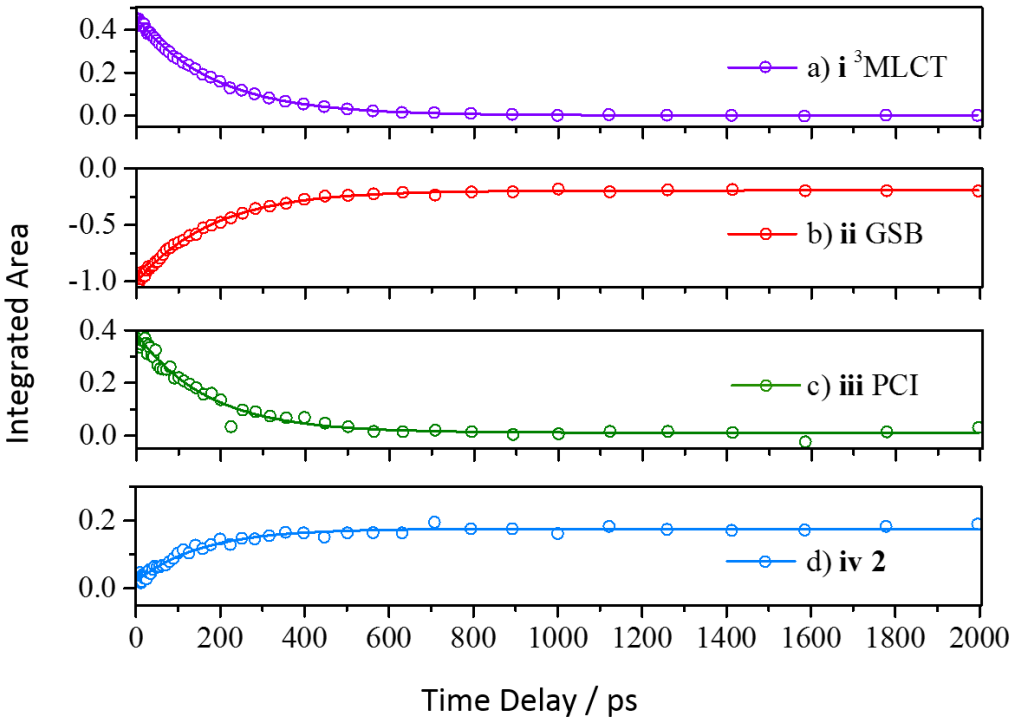

Figure 5.5 Kinetic traces for time-dependent evolution (following 340 nm excitation) of a) ^{3}MLCT (**i**) state population, b) GSB (**ii**) recovery, c) PCI (**iii**) population, and d) **2** the photoproduct (**iv**), obtained from integration of basis functions used in the 'target analysis'. The obtained lifetimes are summarized in Table 5.2.

These time constants compare very favourably with the time constants determined using the same analysis of OPA data (Figure 5.5) with the exception of the time constant for the formation of **2**. This is unsurprising given the strong overlap between the spectral features of **2** and all other features here, and that population (amplitude) of this signal is determined at an early time (< 5 ps) that we do not fully resolve for our TPA data (as was done with the OPA experiment). This shows that qualitatively the photoactivation of **1** following TPA proceeds *via* the same (if not, very similar) pathway as that following OPA *i.e.* **1** + hν →→ ^{3}MLCT → ^{3}MC → PCI → **2**. While it is only the initially populated states that are different for either OPA or TPA, due to the selection rules, the population still appears to arrive at the ^{3}MLCT state following intersystem crossing.

In order to fully assert this, a complete kinetic analysis using fitting functions derived from the branched kinetic scheme (not simple exponentials) and fitted simultaneously would be needed. For the previously published OPA data, it was possible to evaluate all quantum yields for branching of reaction pathways using target analysis and simultaneously fitting traces with multi-exponential functions derived from a full kinetic scheme, leading to the proposed photoactivation mechanism in Figure 5.6. As previously mentioned, the lack of early time data (<5 ps) for TPA, makes it unachievable to elucidate critical ultrafast timescales that affect the evolution of the initially excited

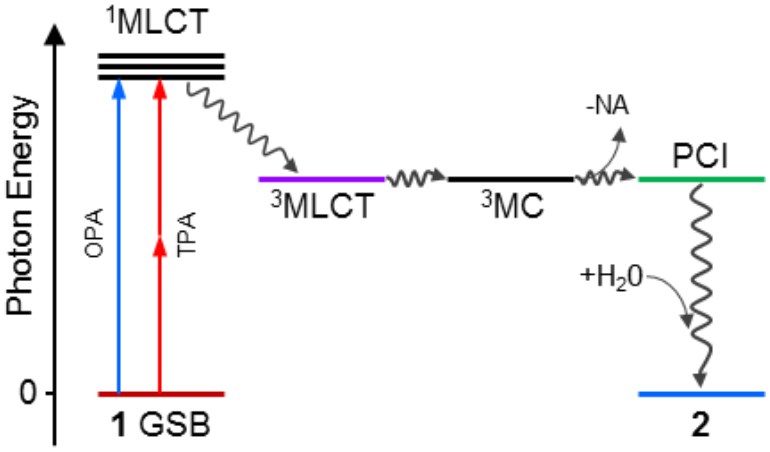

Figure 5.6 Schematic for the photoactivation mechanism of **1**. Following excitation with either OPA or TPA of energy equivalent to ~3 – 4 eV, **2** is formed via a dissociative ^{3}MC state and 5-coordinate intermediary state. Non-reactive pathways are omitted. Coloured states correspond to features in the TAS that are used in the kinetic analysis (see Figures 5.4 and 5.5): GSB of **1**, red, feature **ii**; ^{3}MLCT, violet, feature **i**; PCI, green, feature **iv**; and **2**, blue, feature **iii**.

states and branching ratios, hence we do not present quantum yields. Certainly, we cannot fully rule out other deactivation pathways that compete with intersystem crossing of the ^{1}MLCT to ^{3}MLCT, for example, ^{1}MLCT → ^{3}MC → GS.[25] However, we can still compare the final GSB recovery of both OPA and TPA. Doing so reveals that the GSB recovery after TPA is approximately equal to that of the OPA, suggesting that the quantum yield for formation of **2** by TPA is similar to OPA ($\Phi \approx 0.4$, based on previous OPA analysis).

5.5 Conclusion

To summarize, we have demonstrated that the evolution of the photoactivatable prodrug *cis*-$[Ru(bpy)_2(NA)_2]^{2+}$ following two-photon activation can be probed. Surprisingly, TPA and OPA produce the same photochemistry. The fact that the TPA and OPA mechanisms are the same (or at the very least very similar) attributed here to "funnelling" of excited state flux into the ^{3}MLCT manifold, means that it may be possible to alter the structure of **1** and repeat OPA measurements with the intention of employing TPA in a final clinical stage.

The "bottom-up approach" to study and tune these candidate prodrugs with OPA is more easily achieved due to the higher absorption strengths and the experimental simplicity this provides. Further studies, where the glass response is reduced enabling the study of the very early dynamics may, however, prove lucrative. This could be achieved through the use of molecules with larger TPA cross-sections, allowing for lower

laser excitation powers, or glass-free sample delivery such as with a thin-film liquid 'jet', an approach we have used previously in the laboratory to study guaiacol.[26] Additionally, photoexcitation to higher energies, where the effects of different selection rules for OPA versus TPA are likely to be more pronounced, due to the increased density of states, may well result in different excited state dynamics, thus providing interesting results. In particularly, if other competing pathways to the main MLCT → GS relaxation are identifiable at these excitation energies, the pronounced differences in the photodynamics following OPA and TPA could be stark.

We conclude by noting that the photophysics of Ru(II) complexes are well studied and as such provides a fruitful base from which other similar complexes may be designed. Particularly, the use of ligands with increased conjugation and thus increased TPA cross-section, will prove critical if this type of species is to find clinical use. Such complexes have been made and are now being studied using OPA TEAS to evaluate their efficacy. We return to discuss this in Chapter 6 under outlook.

5.6 Bibliography

1. J. P. Ortonne, *Br. J. Dermatol.*, 2002, **146**, 7-10.
2. R. S. Mason and J. Reichrath, *Anticancer Agents Med. Chem.*, 2013, **13**, 83-97.
3. S. González, M. Fernández-Lorente and Y. Gilaberte-Calzada, *Clin. Dermatol.*, 2008, **26**, 614-626.
4. S. E. Greenough, G. M. Roberts, N. A. Smith, M. D. Horbury, R. G. McKinlay, J. M. Żurek, M. J. Paterson, P. J. Sadler and V. G. Stavros, *Phys. Chem. Chem. Phys.*, 2014, **16**, 19141-19155.
5. L. Carroll and T. R. Humphreys, *Clin. Dermatol.*, 2006, **24**, 2-7.
6. K. Ogawa and Y. Kobuke, *Anti-Cancer Agents in Medicinal Chemistry (Formerly Current Medicinal Chemistry-Anti-Cancer Agents)*, 2008, **8**, 269-279.
7. A. M. Smith, M. C. Mancini and S. Nie, *Nat. Nanotechnol.*, 2009, **4**, 710-711.
8. B. Sullivan, D. Salmon and T. J. Meyer, *Inorg. Chem.*, 1978, **17**, 3334-3341.
9. L. Zayat, C. Calero, P. Alborés, L. Baraldo and R. Etchenique, *J. Am. Chem. Soc.*, 2003, **125**, 882-883.
10. M. J. Frisch, G. W. Trucks, H. B. Schlegel, G. E. Scuseria, M. A. Robb, J. R. Cheeseman, G. Scalmani, V. Barone, B. Mennucci, G. A. Petersson, H. Nakatsuji, M. Caricato, X. Li, H. P. Hratchian, A. F. Izmaylov, J. Bloino, G. Zheng, J. L. Sonnenberg, M. Hada, M. Ehara, K. Toyota, R. Fukuda, J. Hasegawa, M. Ishida, T. Nakajima, Y. Honda, O. Kitao, H. Nakai, T. Vreven, J. A. Montgomery, Jr., J. E. Peralta, F. Ogliaro, M. Bearpark, J. J. Heyd, E. Brothers, K. N. Kudin, V. N.

Staroverov, R. Kobayashi, J. Normand, K. Raghavachari, A. Rendell, J. C. Burant, S. S. Iyengar, J. Tomasi, M. Cossi, N. Rega, J. M. Millam, M. Klene, J. E. Knox, J. B. Cross, V. Bakken, C. Adamo, J. Jaramillo, R. Gomperts, R. E. Stratmann, O. Yazyev, A. J. Austin, R. Cammi, C. Pomelli, J. W. Ochterski, R. L. Martin, K. Morokuma, V. G. Zakrzewski, G. A. Voth, P. Salvador, J. J. Dannenberg, S. Dapprich, A. D. Daniels, Ö. Farkas, J. B. Foresman, J. V. Ortiz, J. Cioslowski and D. J. Fox, *Wallingford, CT*, 2009, **19**, 227-238.

11. K. Aidas, C. Angeli, K. L. Bak, V. Bakken, R. Bast, L. Boman, O. Christiansen, R. Cimiraglia, S. Coriani, P. Dahle, E. K. Dalskov, U. Ekström, T. Enevoldsen, J. J. Eriksen, P. Ettenhuber, B. Fernández, L. Ferrighi, H. Fliegl, L. Frediani, K. Hald, A. Halkier, C. Hättig, H. Heiberg, T. Helgaker, A. C. Hennum, H. Hettema, E. Hjertenæs, S. Høst, I.-M. Høyvik, M. F. Iozzi, B. Jansík, H. J. A. Jensen, D. Jonsson, P. Jørgensen, J. Kauczor, S. Kirpekar, T. Kjærgaard, W. Klopper, S. Knecht, R. Kobayashi, H. Koch, J. Kongsted, A. Krapp, K. Kristensen, A. Ligabue, O. B. Lutnæs, J. I. Melo, K. V. Mikkelsen, R. H. Myhre, C. Neiss, C. B. Nielsen, P. Norman, J. Olsen, J. M. H. Olsen, A. Osted, M. J. Packer, F. Pawlowski, T. B. Pedersen, P. F. Provasi, S. Reine, Z. Rinkevicius, T. A. Ruden, K. Ruud, V. V. Rybkin, P. Sałek, C. C. M. Samson, A. S. de Merás, T. Saue, S. P. A. Sauer, B. Schimmelpfennig, K. Sneskov, A. H. Steindal, K. O. Sylvester-Hvid, P. R. Taylor, A. M. Teale, E. I. Tellgren, D. P. Tew, A. J. Thorvaldsen, L. Thøgersen, O. Vahtras, M. A. Watson, D. J. D. Wilson, M. Ziolkowski and H. Ågren, *Wiley Interdisciplinary Reviews: Computational Molecular Science*, 2014, **4**, 269-284.
12. M. J. Paterson, O. Christiansen, F. Pawłowski, P. Jørgensen, C. Hättig, T. Helgaker and P. Sałek, *J. Chem. Phys.*, 2006, **124**, 054322.
13. R. J. Watts, *J. Chem. Educ.*, 1983, **60**, 834.
14. J. Van Houten and R. J. Watts, *J. Am. Chem. Soc.*, 1976, **98**, 4853-4858.
15. B. Durham, J. V. Caspar, J. K. Nagle and T. J. Meyer, *J. Am. Chem. Soc.*, 1982, **104**, 4803-4810.
16. N. H. Damrauer, G. Cerullo, A. Yeh, T. R. Boussie, C. V. Shank and J. K. McCusker, *Science*, 1997, **275**, 54-57.
17. E. Borfecchia, C. Garino, L. Salassa, T. Ruiu, D. Gianolio, X. Zhang, K. Attenkofer, L. X. Chen, R. Gobetto, P. J. Sadler and C. Lamberti, *Dalton Trans.*, 2013, **42**, 6564-6571.
18. Y. Liu, D. B. Turner, T. N. Singh, A. M. Angeles-Boza, A. Chouai, K. R. Dunbar and C. Turro, *J. Am. Chem. Soc.*, 2009, **131**, 26-27.

19. L. Salassa, C. Garino, G. Salassa, R. Gobetto and C. Nervi, *J. Am. Chem. Soc.*, 2008, **130**, 9590-9597.
20. J. Arnbjerg, M. J. Paterson, C. B. Nielsen, M. Jørgensen, O. Christiansen and P. R. Ogilby, *J. Phys. Chem. A*, 2007, **111**, 5756-5767.
21. L. T. Bergendahl and M. J. Paterson, *J. Phys. Chem. B*, 2012, **116**, 11818-11828.
22. G. A. Heath, L. J. Yellowlees and P. S. Braterman, *J. Chem. Soc., Chem. Commun.*, 1981, 287-289.
23. N. H. Damrauer and J. K. McCusker, *J. Phys. Chem. A*, 1999, **103**, 8440-8446.
24. J. K. McCusker, *Acc. Chem. Res.*, 2003, **36**, 876-887.
25. J. D. Knoll, B. A. Albani and C. Turro, *Acc. Chem. Res.*, 2015, **48**, 2280-2287.
26. S. E. Greenough, M. D. Horbury, J. O. F. Thompson, G. M. Roberts, T. N. V. Karsili, B. Marchetti, D. Townsend and V. G. Stavros, *Phys. Chem. Chem. Phys.*, 2014, **16**, 16187-16195.

6. Conclusion and Outlook

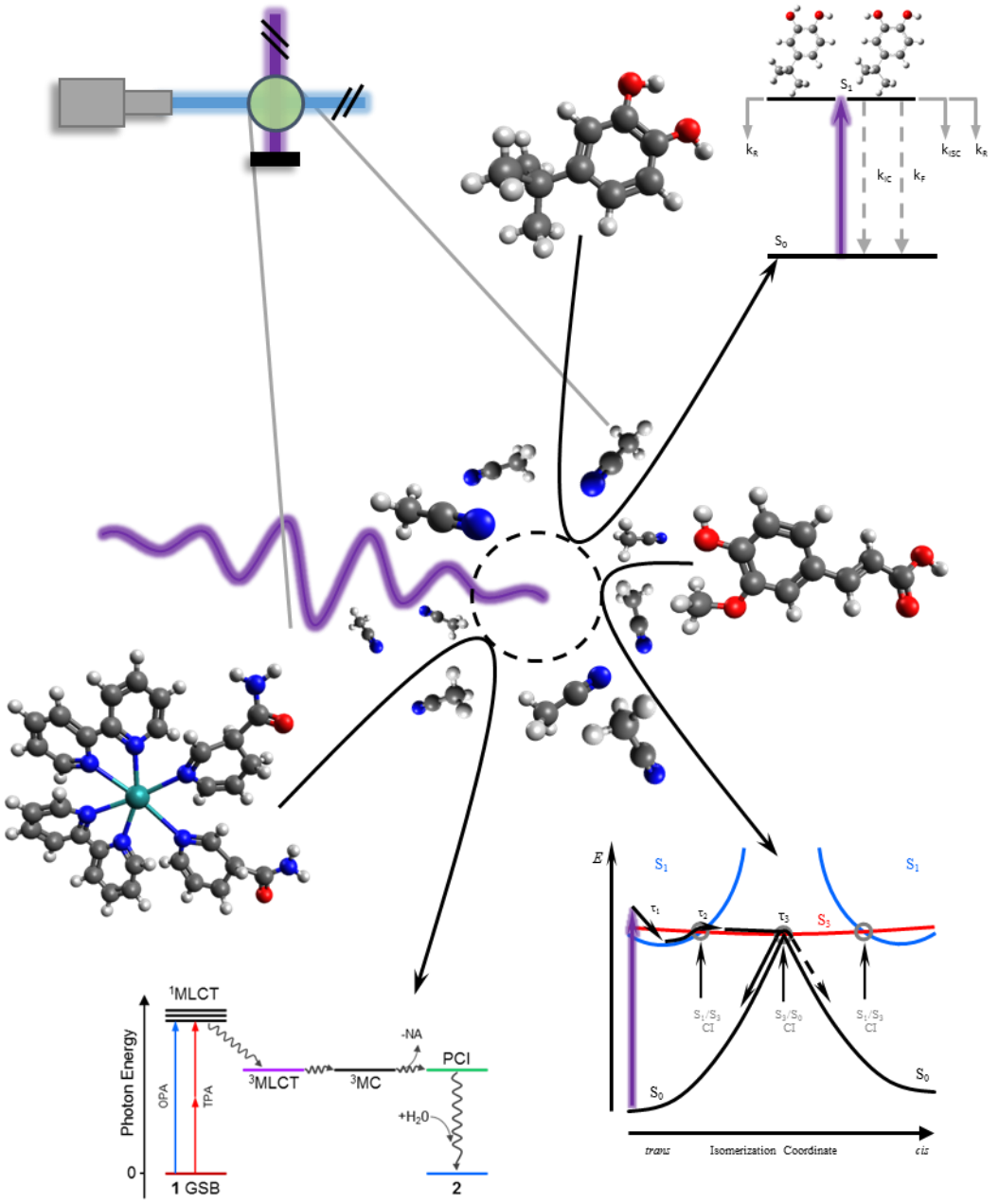

"The only way of discovering the limits of the possible is to venture a little way past them into the impossible."

Arthur C. Clarke

6.1 Summary

This thesis has used femtosecond transient electronic (ultraviolet/visible) absorption spectroscopy (TEAS) to glean dynamical insight on three different systems. While the study on each individual system has its own distinct aim, there still exists a link between each study. Each one of these systems plays a potential role in the protection of biological systems from the deleterious effects of ultraviolet exposure, whether it is an internal protective mechanism within the biological material itself, a preventive measure in the case of a sunscreening agent, or a method of treating any damage that might be induced when the first two fail.

The first chapter of this thesis consisted of an introduction into the physics behind the initial absorption of ultraviolet light to an electronically excited state, followed by a discussion on the various ways in which these excited states can relax. Furthermore, information was provided for TEAS, time-resolved ion yield and time-resolved velocity map imaging, which can be used to observe the evolution of these relaxation processes in real-time, though the main focus was on TEAS. Finally, a brief introduction to the three areas of research on which this thesis focuses on was given.

The second chapter provided a more in-depth overview of the experimental setup used to perform the TEAS measurements presented in Chapters 3, 4 and 5. A description of the laser system used to generate the femtosecond laser pulses was provided, followed by a description of the optical phenomena used to convert the fundamental beam into the required pump and probe beams that are used to interrogate our samples. This included the optical setup required to induce these phenomena. Alongside this was a discussion on the sample delivery system and finally the method for data collection and analysis was explained.

The third chapter demonstrated the environmental effects on the photodynamics of 4-*tert*-butylcatechol (4-*tert*-butly-1,2-dihydroxybenzene, 4-TBC) excited to its first excited state (S_1, $^1\pi\pi^*$). 4-TBC was used as a proxy for catechol (1,2-dihydroxybenzene), an ultraviolet absorbing subunit in the natural photoprotective molecule eumelanin. This work demonstrated that the photoexcited dynamics of 4-TBC displayed a dependence upon the molecule's environment. In the isolated gas-phase, 4-TBC undergoes a rapid dissociation of the non-intramolecularly hydrogen bonded O–H leading to the production of the 4-tert-butylcatecoxyl radical. This process was measured to occur in ~5 ps. This was proposed to occur by tunnelling through the barrier between the photoexcited S_1 state and the dissociative $^1\pi\sigma^*$ (S_2) state, as demonstrated by deuteration of the O–H bond and the measured kinetic isotope effect.

The ultrafast nature of this tunnelling mechanism is believed to be due to the buckled geometry of the S_1 excited state. When solvated in the weakly interacting cyclohexane, 4-TBC displays similar dynamics with a S_1 excited state lifetime of ~18 ps. This excited state is proposed to decay *via* a similar mechanism as the gas-phase, leading to the formation of the 4-tert-butylcatecoxyl radical as evidenced in the long-time TEAS. Once again, deuterated experiments were performed which tentatively suggested O–H fission occurred *via* a tunnelling mechanism (or at the very least a process which involved a barrier along the O–H bond). The difference in the excited state lifetime in cyclohexane compared to the gas-phase, is believed to be induced by subtle changes to the energies of the S_1 and S_2 state leading to a change in the barrier height between the two electronic states. Finally the effects of a strongly interactive environment were investigated by using the solvent acetonitrile and in this environment, 4-TBC displayed a drastic change in the S_1 ESA decay. Instead of a lifetime on the order of picoseconds (as seen in cyclohexane), the S_1 state exhibited a lifetime of ~1.7 ns, with multiple decay pathways being present, though radical formation was still observed. This radical formation disappeared however upon deuteration of 4-TBC, suggesting, once again, that the mechanism for radical formation is mediated, in part, by tunnelling. It was rationalized that this change in dynamics coincided with a structural change, involving the breaking of the intramolecular hydrogen bond between the two hydroxyl groups, which 4-TBC undergoes in a strongly interacting solvent such as acetonitrile.

Chapter 4 looked into the photodynamics of a pair of potential sunscreening agents, ferulic acid (3-(4-hydroxy-3-methoxyphenyl)-2-propenoic acid) and caffeic acid (3-(3,4-dihydroxyphenyl)-2-propenoic acid). The TEAS measurements combined with static ultraviolet/visible difference spectra demonstrated that both molecules can undergo relaxation along a *trans-cis* photoisomerization coordinate. With the help of recent *ab initio* calculations the states involved in this isomerization and the associated time constants were determined. The initial excitation leads to the population of the $1^1\pi\pi^*$ which undergoes a geometry relaxation on a timescale around 50 – 500 fs. Following this the excited state population flows through a conical intersection between the $1^1\pi\pi^*$ and the $2^1\pi\pi^*$ state. Finally once on the $2^1\pi\pi^*$ state, the excited state flux progresses along the *trans-cis* isomerization pathway towards a conical intersection between the $2^1\pi\pi^*$ state and ground state. This leads to either the formation of the initial *trans*-isomer or the *cis*-isomer. In the aqueous TEAS measurements it was impossible to determine whether the *cis*-isomer was being formed. This was because of the phenolic radical absorption being present and occurring in the same spectral region as the spectral signature of the *cis*-isomer. The phenolic radical was shown to be formed *via* a two-

photon ionization process. The formation of the phenolic radical due to two-photon ionization also occurred in acetonitrile. Fortunately, the absorption signatures for the radical and *cis*-isomer were separated enough allowing for observation of the *cis*-isomer. Finally the *cis*-isomer signature was present in the TEAS measurements in dioxane as the formation of the phenolic radical *via* two-photon ionization is evidently strongly supressed.

Chapter 5 explored the photodynamics of the *cis*-$[Ru(bpy)_2(NA)_2]^{2+}$ in water after two-photon excitation and compared this to previously determined photodynamics after one-photon excitation. These dynamics consist of population funnelling through the initially populated singlet metal to ligand charge transfer state into a triplet charge transfer state. From this state, the molecule either undergoes vibration cooling, followed by relaxation back down to the ground electronic state, or it can undergo a ligand dissociation to from a penta-coordinated intermediate species, generated through elimination of the nicotinamide (NA) ligand. If the NA ligand does not possess enough energy to leave the solvent shell, recombination occurs to reform the initial ground state complex, however if it does leave the solvent shell, a solvent molecule will combine with this penta-coordinate intermediate to from the mono-aquated species. The formation of this mono-aquated species is the desired outcome, *i.e.* the key initial step involved in photoactivation. While the long-time dynamics (> 5 ps, after the formation of the triplet metal to ligand charge transfer state) were shown to be akin to that of one-photon excitation, it was impossible to observe the ultrafast dynamics (< 5 ps) due to experimental constraints. Therefore, we cannot definitively say whether the initial dynamics are the same between each activation method.

6.2 Outlook

6.2.1 Environmental Effects

The work on 4-TBC has aided in the progression in our understanding of the effects that solvation can have on the intrinsic properties of a molecule. This bolsters the previous work done in this area of interest.[1-3] These works have highlighted that when using a "bottom-up" approach towards understanding, say, the excited state dynamics of large molecules, not only does functionalization need to be considered, but so do the surroundings and certainly add gravitas to the well-known adage structure determines dynamics which determines function. With this in mind, future work on molecules should consider performing both gas-phase and solution-phase measurements, in order to provide a more in depth, and complete picture of the molecules photodynamics.

Indeed, work is currently underway to study the photodynamics of one of the building blocks of eumelanin. The molecule in questions is 5,6-dihydroxyindole carboxylic acid, one of the dominant monomers present in the eumelanin pigment, which has been studied previously,[4,5] but several questions still remain *e.g*. is a phenolic radical species being formed or not? This however is only one of the many monomers that make up eumelanin, which present a plethora of biologically relevant ultraviolet-chromophores for exploration of their photophysics.

6.2.2 Photoprotection

While the work within the thesis provided a dynamical insight into two potential sunscreening agents, adding to several other studies,[6-8] there is still a plethora of other sunscreen filter molecules, where there is an evident paucity of dynamical data. Therefore, future work will focus on providing this information for a variety of sunscreen filter molecules and, combined with the data presented in this thesis, can hopefully provide valuable knowledge to help design more efficient and effective sunscreens that are more robust to degradation and less phototoxic.

Directly building upon the work presented in this thesis is determining the photodynamics of ethyl ester variants of ferulic and caffeic acids. Secondly in order to determine if the *cis*-isomer is being formed in aqueous solutions for both ferulic and caffeic acid, femtosecond transient vibrational (infrared) absorption spectroscopy will be performed. As in these measurements, the *cis*-isomer signature will no longer be convoluted with the phenolic radical absorption which hinders our ability to say with complete certainty whether the *cis*-isomer is being formed or not.

The eventual aim of this work is to slowly add additional molecules present in commercial suncreams in order to determine what effect, if any, the interactions between the various components have. This will hopefully highlight any detrimental or beneficial interactions between molecules to the overall photoprotective nature of the suncream.

6.2.3 Two-photon Activation

The work presented here showed that in the case of *cis*-$[Ru(bpy)_2(NA)_2]^{2+}$ no major difference was apparent in the photodynamics of activation by either one-photon or two-photon absorption. Therefore, the aim now is to perform similar studies on related metal complexes and other light activated compounds, in order to determine if the photodynamics are comparable between the two excitation schemes. Furthermore, work is being done towards improving the temporal resolution of the experiment in

order to observe the initial ultrafast dynamics after two-photon absorption, in order to see if any differences are present within this region (< 5 ps). This information will hopefully provide an insight into the design of future two-photon activatable complexes with an aim to improving the quantum yield of the desired photoproduct.

6.3 Bibliography

1. S. E. Greenough, M. D. Horbury, J. O. F. Thompson, G. M. Roberts, T. N. V. Karsili, B. Marchetti, D. Townsend and V. G. Stavros, *Phys. Chem. Chem. Phys.*, 2014, **16**, 16187-16195.
2. S. J. Harris, D. Murdock, Y. Zhang, T. A. Oliver, M. P. Grubb, A. J. Orr-Ewing, G. M. Greetham, I. P. Clark, M. Towrie, S. E. Bradforth and M. N. R. Ashfold, *Phys. Chem. Chem. Phys.*, 2013, **15**, 6567-6582.
3. Y. Zhang, T. A. A. Oliver, M. N. R. Ashfold and S. E. Bradforth, *Farad. Discuss.*, 2012, **157**, 141-163.
4. M. Gauden, A. Pezzella, L. Panzella, A. Napolitano, M. d'Ischia and V. Sundström, *J. Phys. Chem. B*, 2009, **113**, 12575-12580.
5. A. Corani, A. Pezzella, T. r. Pascher, T. Gustavsson, D. Markovitsi, A. Huijser, M. d'Ischia and V. Sundström, *J. Phys. Chem. Lett.*, 2013, **4**, 1383-1388.
6. L. A. Baker, M. D. Horbury, S. E. Greenough, P. M. Coulter, T. N. V. Karsili, G. M. Roberts, A. J. Orr-Ewing, M. N. R. Ashfold and V. G. Stavros, *J. Phys. Chem. Lett.*, 2015, **6**, 1363-1368.
7. L. A. Baker, M. D. Horbury, S. E. Greenough, M. N. Ashfold and V. G. Stavros, *Photochem. Photobiol. Sci.*, 2015, **14**, 1814-1820.
8. L. A. Baker, M. D. Horbury, S. E. Greenough, F. Allais, P. S. Walsh, S. Habershon and V. G. Stavros, *J. Phys. Chem. Lett.*, 2016, **7**, 56-61.